



저작자표시-비영리-변경금지 2.0 대한민국

이용자는 아래의 조건을 따르는 경우에 한하여 자유롭게

- 이 저작물을 복제, 배포, 전송, 전시, 공연 및 방송할 수 있습니다.

다음과 같은 조건을 따라야 합니다:



저작자표시. 귀하는 원저작자를 표시하여야 합니다.



비영리. 귀하는 이 저작물을 영리 목적으로 이용할 수 없습니다.



변경금지. 귀하는 이 저작물을 개작, 변형 또는 가공할 수 없습니다.

- 귀하는, 이 저작물의 재이용이나 배포의 경우, 이 저작물에 적용된 이용허락조건을 명확하게 나타내어야 합니다.
- 저작권자로부터 별도의 허가를 받으면 이러한 조건들은 적용되지 않습니다.

저작권법에 따른 이용자의 권리는 위의 내용에 의하여 영향을 받지 않습니다.

이것은 [이용허락규약\(Legal Code\)](#)을 이해하기 쉽게 요약한 것입니다.

[Disclaimer](#)

이학박사학위논문

**Manipulation of Matrix-Isolated Molecules and
Molecular Clusters with Electrostatic Fields**

전기장을 이용한 분자 및 분자 클러스터
조작에 관한 연구

2020년 1월

서울대학교 대학원

화학부 물리화학전공

박 영 욱

Ph.D. Dissertation

**Manipulation of Matrix-Isolated Molecules and
Molecular Clusters with Electrostatic Fields**

Supervisor: Professor Heon Kang

Major: Physical Chemistry

January 2020

by Youngwook Park

Department of Chemistry

The Graduate School

Seoul National University

Manipulation of Matrix-Isolated Molecules and Molecular Clusters with Electrostatic Fields




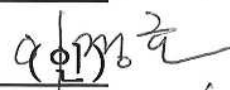
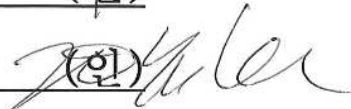
전기장을 이용한 분자 및 분자 클러스터
조작에 관한 연구

지도교수 강 현

이 논문을 이학박사 학위논문으로 제출함
2019년 12월

서울대학교 대학원
화학부 물리화학전공
박 영 옥

박영옥의 이학박사 학위논문을 인준함
2019년 12월

위원장	이 성 훈	(인) 
부위원장	강 현	(인) 
위원	김 지 환	(인) 
위원	이 정 호	(인) 
위원	이 진 용	(인) 

Abstract

Manipulation of Matrix-Isolated Molecules and Molecular Clusters with Electrostatic Fields

Youngwook Park

Department of Chemistry, Physical Chemistry

The Graduate School

Seoul National University

This dissertation aims to demonstrate how a strong external electrostatic field on the order of 10^8 V/m manipulates molecular properties, such as orientation, structure, dynamics, etc., of small molecules and molecular clusters isolated in cold inert matrices. A combination of the ice film nanocapacitor method and the matrix isolation technique enabled the application of unprecedentedly intense external electric dc fields across the isolated molecules and molecular clusters. Changes in molecular properties driven by external fields were investigated by means of vibrational spectroscopy.

Chapter 1 provides a background of molecular-control studies with external forces. A brief history of molecular manipulation using electrostatic, magnetic, and optical fields is introduced, with more detailed examples on molecular control with electrostatic fields in both gas-phase and condensed-phase molecular systems. A concise introduction to the methodology of research in the present dissertation is also given.

Detailed experimental methods are described in **Chapter 2**. The fundamentals and practical aspects of the ice film nanocapacitor method for applying intense external fields, the matrix isolation technique for preparing isolated molecular species, and the reflection–absorption infrared spectroscopy for detecting molecular behaviors are summarized. A description on the instrumentation used in the experiments is provided.

Chapter 3 presents the spectroscopic study on the field-driven change in inversion tunneling dynamics of ammonia molecule. An ammonia molecule isolated in the Ar matrix, which undergoes a rapid umbrella inversion tunneling across the barrier of the symmetric double-minimum potential energy surface when undisturbed, reorients into the direction of an strong external field by Stark mixing of inversion states with close energy levels and opposite parities. An external field results in the asymmetrization of the double-minimum potential and thereby the quenching of inversion dynamics. The static infrared spectra recorded at systematically scanned-field strengths, which encrypt such field-induced behavior of ammonia, were decoded with the help of potential energy surface, localization of wavefunctions, and transition selection rule under the external dc field.

Chapter 4 reports the experimental measurement of the vibrational Stark sensitivity of small hydrogen-bonded water and ammonia clusters ((D₂O)₃, (D₂O)₄, (NH₃)₃, NH₃–HCl, NH₃–H₂O, and (ND₃)₃). The vibrational Stark effect manifests the frequency shift as a result of the field-induced manipulation of potential energy surfaces of molecular vibrations. The Stark sensitivity of vibrations of the clusters was found to significantly differ from the corresponding uncomplexed monomer. The clustering effect on the Stark sensitivity is discussed in the perspective of anharmonicity, geometric effect, and intermolecular vibrational coupling. As an extreme example of the clustering through hydrogen-bonding, Stark spectra of a

crystalline ice were qualitatively interrogated and compared with those of the isolated water monomer.

Chapters 5 and 6 demonstrate that a strong electrostatic field enables the dislocation of an acidic proton. In **Chapter 5**, vibrational Stark spectroscopy was conducted for hydrogen chloride–water (HCl–H₂O, HCl–D₂O) complexes to examine the field-induced behavior of the proton in hydrated acids. The spectra of the complexes showed an extraordinarily large Stark shift of the proton stretching frequency compared to that of uncomplexed HCl molecule. In the case of HCl–D₂O, the vibrational coupling between the proton stretching and the symmetric stretching of D₂O was modified by external fields. Spectral analysis aided by a quantum calculation reveals the reversible and asymmetric translocation of the acidic proton along the proton-transfer coordinate in the HCl–water complexes by applied fields. **Chapter 6** reports the Stark spectra of HCl complexes with ammonia and methylated amines (methylamine, dimethylamine, and trimethylamine), a prototypical example of proton-transferring molecular system. Not only the proton stretching vibration which is a parallel/anti-parallel motion of proton along the proton-transfer coordinate but also the perpendicular proton bending mode showed exceptionally drastic spectral changes under the influence of external fields. The spectral changes by fields were characteristic of each complex with different degree of proton transfer. The studies on the hydrated acids and the proton-transfer complexes provide the spectroscopic evidence of the large protonic polarizability, a concept which occupies a prominent position in the behavior and spectroscopy of proton in chemistry.

Chapter 7 summarizes the dissertation. The significance and prospect of the research presented in this dissertation are briefly addressed in the perspective of intermolecular processes in chemistry and molecular manipulation in quantum technology.

Keywords: molecular manipulation, electrostatic field, tunneling dynamics,
molecular cluster, hydrated acid, proton-transfer complex, vibrational
spectroscopy

Student number: 2014-21234

Contents

Abstract	i
Contents	v
List of Figures and Tables	viii
Chapter 1. Introduction	1
1.1. Manipulation of Molecules with External Fields	2
1.2. Manipulation of Molecules with Homogeneous Electrostatic Fields	4
1.3. Approach and Contents of This Dissertation.....	6
References	8
Chapter 2. Method	16
2.1. A Combined Technique of Ice Film Nanocapacitor and Matrix Isolation ...	16
2.2. Reflection–Absorption Infrared Spectroscopy of Matrix-Isolated Molecules under the Influence of External Fields.....	21
2.3. Instruments	24
References	27
Chapter 3. Electric Field-Control of Inversion Dynamics of Ammonia in an Argon Matrix	31
Abstract.....	31

3.1. Introduction	32
3.2. Experimental Details	34
3.3. Results and Discussion	35
3.4. Conclusion	47
References	49
Chapter 4. Experimental Measurement of Vibrational Stark Sensitivity of	
Small Molecular Clusters: Clustering Effect on Stark Response of	
Vibrations	52
Abstract.....	52
4.1. Introduction	53
4.2. Experimental Details	55
4.3. Results and Discussion	56
4.4. Conclusion	70
References	71
Chapter 5. Spectroscopic Evidence of Large Protonic Polarizability of	
Hydrogen Chloride–Water Complexes.....	77
Abstract.....	77
Main Text	78
References	88
Supporting Information	92
Chapter 6. Vibrational Stark Spectroscopy on Proton Vibrations in Proton-	
Transfer Complexes of Hydrogen Chloride with Ammonia and	
Methylated Amine	103

Abstract.....	103
6.1. Introduction	104
6.2. Experimental Details	107
6.3. Results	108
6.4. Discussion.....	115
6.5. Conclusion.....	121
References	122
Chapter 7. Summary.....	126
List of Publications.....	128
Abstract in Korean (국문 초록)	131
Acknowledgement (감사의 글).....	135

List of Figures and Tables

Figure 3-1. (a) RAIR spectra of the ν_2 umbrella vibration of matrix-isolated NH_3 , measured as a function of the strength of applied electric field. The $\nu=0 \rightarrow 1$ vibrational band origin (968 cm^{-1}) is indicated by the gray arrow. In the spectra, transitions occurring within $K=0$ rotational levels are shown in red, while transitions in $|K|=1$ states are shown in blue. The evolution of peaks induced by the external field is depicted by dotted red and blue lines. (b) Schematic drawings of the double-minimum potential, energy states and allowed transitions at different stages of Stark shifts and mixings. Likewise, the red and blue color-coding indicates features that belong to $K=0$ and $|K|=1$, respectively. (Bottom) A symmetric double-minimum potential at zero field. The transition shown in $R(0_0^-)$, which is prominent at zero field. (Middle) The slightly “tilted” asymmetric double-minimum potential in the intermediate field region. Energy levels and expected transitions are shown for $K=0$ (red) and $|K|=1$ (blue). The red and blue potential curves are identical, but shifted horizontally for clarity. Two strong transitions observed in the intermediate field region are marked with two solid arrows. The dotted blue arrow is an originally-allowed transition at zero field but that becomes a forbidden transition as the field strength increases. (Top) Strongly asymmetric double-minimum potential in the high field region. Transitions are localized in the deeper well of the potential and the two transitions coincide in energy.

Figure 3-2. Schematic picture of energy levels of NH_3 umbrella inversion–rotation–vibration states and allowed transitions at (a) zero field, (b) intermediate field, and (c) strong field. Those relevant to the spectroscopic observation in this work are

displayed. Energy levels marked with black and gray horizontal lines are those of $K=0$ and $|K|=1$, respectively, which are shown horizontally dislocated for visual clarity. Dotted horizontal lines in diagram (a) indicate the energy levels that are absent due to nuclear permutation symmetry. In diagram (c), strong field orientation makes ammonia molecules become a harmonic librator bound in the potential well of the electrostatic dipole–field interaction. The quantum number N in diagram (c) indicates the vibrational quanta of the harmonic librator, which is defined as $N = 2\tilde{J} - |K + M|$ where \tilde{J} designates the value of the J quantum number of the free-rotor state that adiabatically correlates with the state under external electrostatic fields [15]. The K and M , the projections of the rotational angular momentum J on the c-axis in the molecular frame and Z-axis in the laboratory frame, respectively, remain good quantum numbers under the electrostatic field that is collinear with the radiative field of the IR beam. The correlation diagram between the freely-rotating symmetric top states (without inversion tunneling) and the harmonic librator states has been reported [15, 16]. According to the correlation diagram, the 0_0 and 1_1 rotational levels of a symmetric top at zero field evolve into the lowest-lying harmonic librator states ($N=0$) at strong field. A similar correlation diagram is expected for ammonia because it behaves like a polar symmetric top at strong field due to the quenching of inversion tunneling and the localization of ν_2 transitions in the lower well of the asymmetric double-minimum potential. Because these correlations between the rotational and librational states exist for both $\nu=0$ and 1, the two ν_2 transitions in $K=0$ and $|K|=1$ observed at intermediate field merge into one peak at strong field. The symbols ‘a’, ‘b’, and ‘c’ correspond to the observed transitions marked with identical symbols in Figure 3-1(a).

Figure 3-3. (a) A symmetric double-minimum potential at zero field. Energy levels

and corresponding wavefunctions of the inversion doublet states in the ground and first excited vibrational levels are shown within the potential. The color of wavefunctions illustrates the selection rule: transitions are allowed between the same color wavefunctions (“bottom-to-top” and “top-to-bottom”). (b) An asymmetric double-minimum potential in the presence of the external field. The energy splittings of doublets are Δ_g and Δ_e for the ground and excited vibrational levels, respectively. For simplicity, wavefunctions that are fully localized by complete (1:1) Stark mixing are shown, although Δ_g and Δ_e represent intermediate Stark mixing. Notice that the left well wavefunctions do not overlap with the right well wavefunctions. (c) Schematic plot of the energy splittings as a function of external field strength. The dashed line indicates the dipole–field interaction energy ($|u| = |\boldsymbol{\mu} \cdot \mathbf{F}|$).

Figure 3-4. (a) Plot of relative peak positions of umbrella vibrational mode of ammonia isotopologues as a function of external field strength. The term ‘relative peak position’ in the plot is used to visually present the frequency separations of two coalescing peaks and the linear shift in the strong field regime for each isotopologue. The absolute values in the ordinate and the vertical spacing between the data points of different isotopologues have no physical meaning. The dashed lines show the trend. The linear field-dependence of the frequency in the strong field regime is the result of the vibrational Stark effect of field-oriented molecules. (b) Plot of the frequency separation between the pair of coalescing peaks as a function of external field strength for NH_3 and NH_2D . (c) Stark spectra of the umbrella vibrational mode of matrix-isolated ammonia isotopologues. The (bottom, middle, top) spectra were recorded under external fields at strengths of (1.3, 2.1, 3.6), (1.0, 1.9, 3.4), (1.0, 1.9,

3.4), and $(1.3, 2.1, 3.5) \times 10^7$ V/m for NH_3 , NH_2D , NHD_2 , and ND_3 , respectively. The peak separations are marked by the double-headed arrows.

Figure 4-1. RAIR spectra of the Ar film containing D_2O molecules inside, (a) at zero field and (b) under field of 1.9×10^8 V/m. (c) Difference spectrum of (b) and (a). The spectral bands for the bonded OD stretch vibrations of $(\text{D}_2\text{O})_3$ and $(\text{D}_2\text{O})_4$ are highlighted with gray shades. The spectra were acquired with a spectral resolution of 4 cm^{-1} .

Figure 4-2. Vibrational Stark spectra (difference absorbance; black solid lines) of the bonded OD stretch mode of $(\text{D}_2\text{O})_3$ isolated in the Ar matrix acquired at various field strengths with fit (red solid lines). The zero-field absorbance for each difference spectrum is displayed with gray dotted lines. The contributions on the fit of the zeroth, first, and second derivatives of zero-field absorbance are depicted with cyan, green, and blue dashed lines, respectively. The experimental spectra were acquired with a spectral resolution of 4 cm^{-1} .

Figure 4-3. Vibrational Stark spectra of the umbrella vibration of the matrix-isolated $(\text{NH}_3)_3$ with (a) difference absorbance fit and (b) Stark absorbance fit. The color-coding of lines in (a) is identical with that in Figure 4-2. In the case of (b), black solid lines, red solid lines, and gray dotted lines correspond to the Stark absorbance, simulated Stark absorbance, and zero-field absorbance, respectively. The field strength at which each Stark spectrum was acquired and the magnitude of vibrational Stark sensitivity ($|\Delta\mu|$) obtained by fitting the spectrum are marked in each plot in units of V/m (black) and $\text{cm}^{-1}/(10^8 \text{ V/m})$ (red), respectively. The experimental spectra were acquired with a spectral resolution of 1 cm^{-1} .

Table 1. Resonant frequency and magnitude of Stark sensitivity of the OD stretching and the ammonia umbrella vibrations for various clusters.

Figure 4-4. Simplified schematic of clustering effect on Stark sensitivity of vibrations. (a) Increase of anharmonic character of the OD stretching by hydrogen-bonding. (b) Suppression of field-driven HNH angle change in NH₃ when hydrogen-bonded. (c) Symmetrized potential energy surface of out-of-phase coupling of the NH₃ umbrella vibration.

Figure 4-5. (a) Stark spectra of D₂O crystalline ice in the stretching region (2300–2700 cm⁻¹) and the bending region (1000–1400 cm⁻¹). The film structure was Cs⁺/H₂O(amorphous; 14 nm)/Ar(70 nm)/D₂O(crystalline; 46 nm)/Pt. The D₂O crystalline ice was prepared by adsorption of D₂O molecules at 140 K followed by 150 K annealing for a short period (~100 seconds). Solid line is an absorbance spectrum at zero field. Dashed line is a difference absorbance between the spectra under 1.4×10^8 V/m and at zero field. Spectral resolution: 4 cm⁻¹. (b) Stark spectra of the symmetric stretching (2657.7 cm⁻¹) and the bending (1174.6 cm⁻¹) vibrational bands of field-oriented D₂O monomer isolated in the Ar matrix. Solid line spectrum was acquired at 3.3×10^7 V/m. Dashed line is a difference spectrum between the spectra under 1.2×10^8 V/m and 3.3×10^7 V/m. The magnitude of Stark sensitivity is shown in the unit of cm⁻¹/(10⁸ V/m). Gray dotted vertical lines visually guide the degree of field-induced peak position shift. Spectral resolution: 1 cm⁻¹.

Figure 5-1. (a) RAIR spectra of the $\nu_{\text{stretch}}(\text{H}-\text{Cl})$ of the matrix-isolated HCl–H₂O 1:1 complex, acquired as a function of external electric field strength. (b) RAIR spectra

of the HCl–D₂O 1:1 complex acquired in a similar manner. The features related to the proton vibration are marked with ‘**a**’ and ‘**b**’ at the zero field spectrum. The dashed profiles at the ‘**a**’ peak position indicate the intensity of $\nu_{\text{sym.stretch}}(\text{D}_2\text{O})$ band of D₂O monomer in the matrices at each stage of field strength (see Figure 5-S3). The peak at 2615 cm⁻¹ is assigned to $\nu_{\text{stretch}}(\text{D}_2\text{O})$ of (D₂O)₂ in the Ar matrix, which is beyond the scope of this work. (c) Plot of the position of the peaks shown in (a) and (b) as a function of the field strength. The slopes of linear fit for the peak position shift are marked in the unit of cm⁻¹/(10⁸ V/m).

Figure 5-2. (a, b) Comparison of field-induced spectral changes of the proton vibrations between (a) HCl–H₂O and (b) HCl–D₂O complexes. The black, red, and blue lines indicate the spectra at zero field, spectra acquired under external fields, and the difference spectra, respectively. (Top) Under moderate fields (3.8×10^7 V/m for HCl–H₂O, 3.9×10^7 V/m for HCl–D₂O). (Bottom) Under strong fields (1.2×10^8 V/m for HCl–H₂O, 1.3×10^8 V/m for HCl–D₂O). The red dotted lines show the contribution of the $\nu_{\text{sym.stretch}}(\text{D}_2\text{O})$ of D₂O monomer for the spectra of HCl–D₂O. (c, d) Simulated spectra for (c) HCl–H₂O and (d) HCl–D₂O 1:1 complexes. The black lines correspond to the zero-field spectrum, which is simulated for the strongest-coupling geometry between the H–Cl stretching and D₂O symmetric stretching for the HCl–D₂O complex. The spectra are calculated upon the artificial change of $r(\text{H–Cl})$: one half of the ensemble with decreased $r(\text{H–Cl})$ (green dashed lines) from the zero-field geometry and the other half with increased $r(\text{H–Cl})$ (gray dashed lines). The red lines are the sum of the green and gray lines at each plot. The blue lines are the difference between the red and black lines. (Top panel) $\Delta[r(\text{H–Cl})] = \pm 0.05$ pm; (bottom panel) $\Delta[r(\text{H–Cl})] = -0.1, +0.3$ pm. (e) Spectral evolution calculated for HCl–H₂O and HCl–D₂O complexes upon artificial changes in $r(\text{H–Cl})$, both

positively and negatively from the strongest-coupling geometry marked with $\Delta[r(\text{H}-\text{Cl})] = 0$.

Figure 5-S1. RAIR spectra of the Ar film containing HCl and H₂O molecules inside, (a) at zero field and (b) under field whose strength is 3.2×10^7 V/m. (c) Difference spectrum of (b) and (a). The spectral region for the $\nu_{\text{stretch}}(\text{H}-\text{Cl})$ of HCl–H₂O 1:1 complex (2663 cm^{-1}) is marked by the shaded gray and shown magnified in the inset.

Figure 5-S2. Stark spectra of the film containing HCl and D₂O acquired at various pressure ratios of Ar, HCl, and D₂O, (a) series of constant D₂O pressure and (b) constant HCl. The black and gray solid lines indicate the spectra at zero field and under fields (about 1.2×10^8 V/m), respectively, and the difference spectra between them are displayed with dotted lines.

Figure 5-S3. This figure illustrates how the symmetric stretching band of D₂O monomer, marked with dashed lines in Figure 5-1(b) and red-dotted lines in Figure 5-2(b), which overlaps with the band of the HCl–D₂O complex in the Stark spectra, was estimated. Black solid line in (a) is the spectrum of the matrix-isolated HCl–D₂O complex under the external field whose strength is about 1×10^8 V/m. Line in (b) shows the difference spectrum of the black line with its zero field spectrum (not shown) in the bending vibration region of D₂O monomer isolated in the film. The intense rise in the difference spectrum (b) corresponds to the bending vibration origin peak of D₂O monomer oriented to the external field direction. The gray solid line in (c) displays the difference spectrum, between the spectra under 1×10^8 V/m field and at zero field, of the matrix which is comprised only of D₂O. The difference spectrum in (c) was scaled by a certain factor to make the intensity of the bending

vibration peak of D₂O monomer identical with that of the difference spectrum in (b). Under this circumstance, the symmetric stretching band of D₂O monomer in the line at 2658 cm⁻¹ in (c) is extracted (gray dotted line in (a)) and used as an estimation of that involved in the Stark spectrum of the HCl–D₂O complex. Black dashed line in (a) is the result of subtracting the gray dotted line from the black solid line in (a).

Figure 5-S4. (a) Simulated spectra of the HCl–D₂O complex in the H–Cl stretching and D₂O symmetric stretching region. H–Cl distance ($r(\text{H–Cl})$) was artificially changed both positively and negatively from the strongest-coupling structure as a reference point, which is marked as $\Delta[r(\text{H–Cl})] = 0$ in the Figure. The distance $r(\text{H–Cl})$ at the strongest-coupling structure was 129.15 pm. See the main text for details on the calculation. (b) The calculated frequency and IR intensity of the proton vibrations of HCl–H₂O and HCl–D₂O.

Figure 5-S5. (Top) Calculated energies of the HCl–water 1:1 complex upon the displacement of proton. The energy and dipole moment was calculated for the optimized structure with frozen $r(\text{H–Cl})$, as mentioned in the main text in detail. The dipole–field energy shown in the plot is the absolute magnitude of $u = -\boldsymbol{\mu} \cdot \mathbf{F}$ under the influence of the external field with 2×10^8 V/m strength which is parallel (or anti-parallel) to the dipole moment. The dipole–field energy in increasing $r(\text{H–Cl})$ direction exceeds the chemical destabilization energy up to $\Delta[r(\text{H–Cl})] = +0.2$ pm at 2×10^8 V/m, whereas in decreasing $r(\text{H–Cl})$ direction, the field-driven energy gain hardly overcomes the destabilization. (Bottom) Simulated potential energy surfaces calculated from the sum of zero-field potential surface with the dipole–field interaction energy.

Figure 6-1. Vibrational correlation diagram of $A\cdots H\cdots B$ complexes ($A = \text{Cl}$; $B = \text{H}_2\text{O}, \text{NH}_3, \text{MeNH}_2, \text{Me}_2\text{NH}, \text{Me}_3\text{N}$) isolated in the Ar matrix. The proton stretching frequency of each complex is plotted as a function of proton affinity of the acceptor (B).

Figure 6-2. RAIR spectra of the Ar matrix containing HCl and NH_3 acquired as a function of field strength. The bands that correspond to HCl– NH_3 1:1 complex are highlighted with shades. Dotted line indicates the difference absorbance between the Stark spectrum at 2.4×10^7 V/m and the zero-field spectrum. The broad band at 1220 cm^{-1} is of the bending vibration of D_2O layer capping the Ar matrix, used for the ice film nanocapacitor.

Figure 6-3. Stark spectra of HCl– MeNH_2 complex. The slash pattern around 800 cm^{-1} shows the spectral region with large instrumental error.

Figure 6-4. Stark spectra of HCl– Me_2NH complex.

Figure 6-5. Stark spectra of HCl– Me_3N complex. The dashed gray spectrum was acquired from the Ar matrix containing only Me_3N , without HCl. The dotted vertical lines indicate the peak positions of the matrix-isolated HCl– Me_3N 1:1 complex.

Figure 6-6. Schematic of proton displacement induced by parallel/anti-parallel and perpendicular external fields.

Figure 6-7. Peak frequency plot as a function of external field strength for different

matrix-isolated complexes of HCl with NH_3 , MeNH_2 , Me_2NH , and Me_3N . The Stark sensitivity values, $c_{\text{local}}|\Delta\mu|/c_{\text{dist}}$, estimated from the frequency change under external fields, are shown in the right-side of the plot.

Chapter 1

Introduction

Manipulation of molecules with controllable external forces is a dream of chemists. The molecular manipulation includes the control of rotation, vibration, and translation of molecules as well as quantum states, dynamics, and reactivity. Molecules are inherently quantum-mechanical systems, control of which potentially can lead to quantum technology, such as quantum memory and quantum computing. One of the traditional interest in physical chemistry, termed chemical stereodynamics, is to direct molecular orientation or alignment, control molecular collisions, and thereby control chemical reactions using external fields [1]. The possibility of controlling chemical reactions with dc electric fields [2–9] and ac fields [10, 11] has been examined.

External forces which can be utilized to manipulate molecular states include electrostatic fields, magnetic fields, and electromagnetic optical fields. Among these, electrostatic manipulation of molecules and molecular clusters is the focus of this dissertation. Electrostatic field is a fundamental concept in chemistry since non-covalent intermolecular interactions are mostly electrostatic [12, 13]. Electrostatic manipulation of molecules is, therefore, at the heart of the interrogation on intermolecular interactions and molecular engineering. This research effort has been limited by the lack of appropriate techniques that can achieve a high-field strength. The ice film nanocapacitor method [14] developed recently in our research group was combined with the matrix-isolation approach [15–18] to provide sufficiently strong external electrostatic fields to isolated molecules and molecular clusters.

Introduced in the rest of this dissertation are the subjects that exemplify the molecular control using electrostatic forces.

Three subheadings comprise the Introduction. **1.1** introduces briefly the history of molecular manipulation with external fields. Among those, examples of electrostatic manipulation are described in **1.2**. Lastly, **1.3** includes a brief description on the experimental approach and the contents of this dissertation.

1.1. Manipulation of Molecules with External Fields

The motion of molecules was controlled in various methods ever since the first experimental electric-field deflection of polar molecules performed by Wrede [19], a graduate student of Stern who is famous for Stern-Gerlach experiment on spatial quantization. Inhomogeneous electric fields [20–24] or intense laser fields [25–27] were utilized for the field control of molecular beams, including the transverse motion control (focusing the beam) and longitudinal motion control (deceleration and acceleration of the molecules). Conceptually, the field control of molecular beams uses the high-field-seeking or low-field-seeking property of states in the molecules: it is basically state-selective. Longitudinal control was found to be much more challenging than transverse control.

The deceleration of molecules leads to the field trapping of molecules. The trapping of molecules, in line with the trapping of molecular ionic species [28–30], widens the scope of spectroscopic studies by enormously extending the time of interrogation. Magnetic traps [31], electrostatic traps [23, 32, 33], and laser field traps [34–36] have been proposed and realized.

Essence of chemical stereodynamics is the control of molecular orientation

and alignment, which was enabled by field control of molecular rotation. Weak electrostatic fields of a hexapole were used to mix near-degenerate states and thereby change the orientation for symmetric top molecules [37–39]. In the case of other types of rigid rotor, namely linear and asymmetric top, high-field strength and rotational cooling to low temperatures below 10 K were required for brute-force orientation. This electrostatic manipulation of molecular orientation through pendularization with homogeneous fields is described in detail in **1.2**. Magnetic and off-resonant laser ac fields resulted the alignment of molecules. Note that orientation is related with $\langle \cos\theta \rangle$ while alignment, with $\langle \cos^2\theta \rangle$. An electric field mixes molecular states with the opposite parity while a magnetic and or a laser field mixes states with the same parity. Electrostatic fields were combined with off-resonant ac fields to achieve better orientation [40–42], where ac fields can generate near-degenerate doublets with opposite parity which can be actively mixed by electrostatic fields. Short laser pulses interacting with molecules result in non-adiabatic alignment and orientation of the molecules [43, 44].

Listed above is a brief summary, with a limited amount of examples, on the history of molecular control with external fields in the gas phase. A detailed review with an extensive amount of references can be found elsewhere [45]. The systematic field control of molecular properties has been restricted mostly to gas phase studies, since molecules in the condensed phase have much more complicated states and strong interactions with neighboring molecules, a problem difficult to overcome with currently available technique and achievable field strength.

1.2. Manipulation of Molecules with Homogeneous Electrostatic Fields

An electrostatic field influences a gas-phase molecule by mixing its internal quantum states with opposite parity. The matrix elements in Hamiltonian which illustrate the effect of a dc electric field on the molecule is given by eq. (1-1).

$$V_F = -\boldsymbol{\mu} \cdot \mathbf{F} \quad [\boldsymbol{\mu}: \text{dipole moment, } \mathbf{F}: \text{electric field}] \quad \text{eq. (1-1)}$$

A dimensionless parameter $\mu F/\Delta_{\pm}$ characterizes the interaction between a molecule and a dc electric field [45]. where Δ_{\pm} corresponds to the energy splitting between opposite parity levels at zero field. For example, in the case of a linear molecule, the states with opposite parity are J and $J+1$, which makes the value of Δ_{\pm} correlated with the rotational constant. In the case of ammonia, Δ_{\pm} corresponds to the tunneling splitting.

Field strength achievable in the gas-phase experiments was limited to $<10^7$ V/m. Molecules with small rotational constant and large dipole moment were oriented by dc electric fields, with the aid of rotational cooling. The external dc fields hybridized rotational energy levels to produce pendular states. Molecules behave as a harmonic vibrator in the extreme field strength. The pendularization induced by external dc fields resulted in the drastic spectral changes in IR spectra, studies on which were termed pendular states spectroscopy. Friedrich and Herschbach are pioneers of the field [46–49]. The pendular behavior under electrostatic fields has been examined for different classes of rigid rotor, namely linear [46, 49, 50], symmetric top [42, 51], and asymmetric top [52–54]. Loesch and coworkers oriented molecules and investigated stereodynamics of molecular collisions [55–57]. Miller and coworkers attributed field-induced spectral changes to field manipulation of structure and dynamics of molecules and molecular clusters [58, 59]. The pendular

state spectroscopy was expanded toward the large biomolecules trapped in He nanodroplet, to determine the direction of vibrational transition dipole moments in those large molecules by means of field orientation [60, 61].

Boxer and coworkers investigated field-induced frequency shifts of molecular vibrations in the condensed phase [62, 63]. The maximum field strength applicable in the condensed phase is about 10^8 V/m, one order of magnitude larger than that in the gas phase. Electrostatic fields manipulate the potential energy surfaces and thereby the resonant frequency [64]. With a linearly polarized detecting IR beam, Boxer and coworkers were able to observe broadening of a vibrational band of an oscillator under the influence of strong electric fields. In the case of the condensed molecules, dc electric fields hardly influence the molecular orientation due to severely large intermolecular interactions. The vibrational Stark sensitivity of an oscillator could be determined from spectral changes under fields. Boxer and coworkers locate the oscillator with the known Stark sensitivity inside solvents and protein structures as an electric field probe to determine the field strength inside such natural environments [65–67].

Shin et al. developed a device called ice film nanocapacitor [14]. Inside the nanocapacitor, electrostatic fields $<4 \times 10^8$ V/m were applied across the frozen chemically-tailored molecular films. Field-induced phenomena in the condensed-phase molecular systems, including dipolar polarization of acetone film [68], Stark manipulation of hydroxyl stretch vibration of ice [69], internal rotation of 1,2-dichloroethane induced by fields [70], and enhancement of acid–base reactivity [71], were interrogated.

1.3. Approach and Contents of This Dissertation

In this dissertation, intense electrostatic fields generated by the ice film nanocapacitor method were applied across the cold inert gas matrices (~ 10 K) containing molecules and molecular clusters of interest. The feasibility has been verified by the previous publications on field manipulation of matrix-isolated small molecules including formaldehyde, hydrogen chloride, and water [15–17]. This experimental approach combines two advantageous aspects, each of the gas- and condensed-phase studies. One is that the molecules and molecular clusters isolated in the inert matrices are, as those in the gas phase, easier to manipulate with external forces compared to molecules in the bulk. The other is the advantage of condensed-phase experiments; that is, high-field strength is achievable. Moreover, molecules and clusters are translationally trapped inside the rigid matrices, which enables long-time spectroscopic interrogation.

Quoting a sentence directly from a review on the field manipulation of molecules [45]: “The interactions of the electrons and nuclei with the static and far-off-resonant optical fields used in experiments give rise to matrix elements with magnitudes ≤ 100 GHz (~ 3.3 cm^{-1}).” With an unprecedentedly intense electrostatic field which resulted one order of magnitude larger interaction (> 30 cm^{-1}) than the previous, it was possible to explore beyond the boundary of traditional field control studies. This dissertation includes examples of significantly large field-induced spectral changes of molecules and molecular clusters, an indication of electrostatic manipulation of orientation, structure, and dynamics.

The contents of the rest of this dissertation are as following. **Chapter 2** describes the experimental methods in detail. **Chapter 3** presents the field control of inversion tunneling dynamics of matrix-isolated ammonia, encoded in the

frequency-domain spectra. **Chapter 4** illustrates the experimental determination of the vibrational Stark sensitivity of hydrogen-bonded clusters and the examination on clustering effect on the vibrational Stark sensitivity. The field-induced proton dislocation in the hydrogen chloride–water complexes and hydrogen chloride–ammonia (or amines) complexes is discussed in **Chapter 5** and **6**, respectively, evidenced by extraordinarily large spectral changes under the influence of electrostatic fields. **Chapter 7** summarizes the dissertation.

References

1. Herschbach, D. Chemical Stereodynamics: Retrospect and Prospect. *Eur. Phys. J. D* **2006**, *38*, 3–13.
2. Shaik, S.; de Visser, S. P.; Kumar, D. External Electric Field Will Control the Selectivity of Enzymatic-Like Bond Activations. *J. Am. Chem. Soc.* **2004**, *126*, 11746–11749.
3. Meir, R.; Chen, H.; Lai, W.; Shaik, S. Oriented Electric Fields Accelerate Diels–Alder Reactions and Control the Endo/Exo Selectivity. *ChemPhysChem* **2010**, *11*, 301–310.
4. Gorin, C. F.; Beh, E. S.; Kanan, M. W. An Electric Field–Induced Change in the Selectivity of a Metal Oxide–Catalyzed Epoxide Rearrangement. *J. Am. Chem. Soc.* **2011**, *134*, 186–189.
5. Gorin, C. F.; Beh, E. S.; Bui, Q. M.; Dick, G. R.; Kanan, M. W. Interfacial Electric Field Effects on a Carbene Reaction Catalyzed by Rh Porphyrins. *J. Am. Chem. Soc.* **2013**, *135*, 11257–11265.
6. Shaik, S.; Mandal, D.; Ramanan, R. Oriented Electric Fields as Future Smart Reagents in Chemistry. *Nat. Chem.* **2016**, *8*, 1091–1098.
7. Aragonès, A. C.; Haworth, N. L.; Darwish, N.; Ciampi, S.; Bloomfield, N. J.; Wallace, G. G.; Diez-Perez, I.; Coote, M. L. Electrostatic Catalysis of a Diels–Alder Reaction. *Nature* **2016**, *531*, 88–91.
8. Akamatsu, M.; Sakai, N.; Matile, S. Electric-Field-Assisted Anion– π Catalysis. *J. Am. Chem. Soc.* **2017**, *139*, 6558–6561.
9. Shaik, S.; Ramanan, R.; Danovich, D.; Mandal, D. Structure and Reactivity/Selectivity Control by Oriented-External Electric Fields. *Chem.*

- Soc. Rev.* **2018**, *47*, 5125–5145.
10. Sussman, B. J.; Townsend, D.; Ivanov, M. Y.; Stolow, A. Dynamic Stark Control of Photochemical Processes. *Science* **2006**, *314*, 278–281.
 11. Corrales, M.; González-Vázquez, J.; Balerdi, G.; Solá, I.; De Nalda, R.; Bañares, L. Control of Ultrafast Molecular Photodissociation by Laser-Field-Induced Potentials. *Nat. Chem.* **2014**, *6*, 785–790.
 12. Havenith, M. H. *Infrared Spectroscopy of Molecular Clusters: An Introduction to Intermolecular Forces*; Springer-Verlag: Berlin, 2002.
 13. Stone, A. *The Theory of Intermolecular Forces*; Oxford University Press: Oxford, 2013.
 14. Shin, S.; Kim, Y.; Moon, E.-s.; Lee, D. H.; Kang, H.; Kang, H. Generation of Strong Electric Fields in an Ice Film Capacitor. *J. Chem. Phys.* **2013**, *139*, 074201.
 15. Park, Y.; Kang, H.; Kang, H. Brute Force Orientation of Matrix-Isolated Molecules: Reversible Reorientation of Formaldehyde in an Argon Matrix toward Perfect Alignment. *Angew. Chem. Int. Ed.* **2017**, *56*, 1046–1049.
 16. Kang, H.; Park, Y.; Kim, Z. H.; Kang, H. Electric Field Effect on Condensed-Phase Molecular Systems. VI. Field-Driven Orientation of Hydrogen Chloride in an Argon Matrix. *J. Phys. Chem. A* **2018**, *122*, 2871–2876.
 17. Park, Y.; Lim, J. H.; Lee, J. Y.; Kang, H. Electric Field Effect on Condensed-Phase Molecular Systems. VII. Vibrational Stark Sensitivity of Spatially Oriented Water Molecules in an Argon Matrix. *J. Phys. Chem. C* **2019**, *123*, 9868–9874.
 18. Park, Y.; Kang, H.; Field, R. W.; Kang, H. The Frequency-Domain IR Spectrum of Ammonia Encodes Changes in Molecular Dynamics Caused

- by a DC Electric Field. *Proc. Natl. Acad. Sci. U.S.A.* **2019**, *116*, 23444–23447.
19. Wrede, E. Über die Ablenkung von Molekularstrahlen Elektrischer Dipolmoleküle im Inhomogenen Elektrischen Feld. *Z. Phys.* **1927**, *44*, 261–268.
 20. Gordon, J. P.; Zeiger, H. J.; Townes, C. H. The Maser—New Type of Microwave Amplifier, Frequency Standard, and Spectrometer. *Phys. Rev.* **1955**, *99*, 1264–1274.
 21. Filsinger, F.; Küpper, J.; Meijer, G.; Hansen, J. L.; Maurer, J.; Nielsen, J. H.; Holmegaard, L.; Stapelfeldt, H. Pure Samples of Individual Conformers: The Separation of Stereoisomers of Complex Molecules Using Electric Fields. *Angew. Chem. Int. Ed.* **2009**, *48*, 6900–6902.
 22. Bethlem, H. L.; Berden, G.; Meijer, G. Decelerating Neutral Dipolar Molecules. *Phys. Rev. Lett.* **1999**, *83*, 1558–1561.
 23. Bethlem, H. L.; Berden, G.; Crompvoets, F. M.; Jongma, R. T.; Van Roij, A. J.; Meijer, G. Electrostatic Trapping of Ammonia Molecules. *Nature* **2000**, *406*, 491–494.
 24. Meek, S. A.; Conrad, H.; Meijer, G. Trapping Molecules on a Chip. *Science* **2009**, *324*, 1699–1702.
 25. Stapelfeldt, H.; Sakai, H.; Constant, E.; Corkum, P. B. Deflection of Neutral Molecules Using the Nonresonant Dipole Force. *Phys. Rev. Lett.* **1997**, *79*, 2787–2790.
 26. Purcell, S.; Barker, P. Controlling the Optical Dipole Force for Molecules with Field-Induced Alignment. *Phys. Rev. A* **2010**, *82*, 033433.
 27. Zhao, B. S.; Chung, H. S.; Cho, K.; Lee, S. H.; Hwang, S.; Yu, J.; Ahn, Y.; Sohn, J.; Kim, D.; Kang, W. K. Molecular Lens of the Nonresonant Dipole

- Force. *Phys. Rev. Lett.* **2000**, *85*, 2705–2708.
28. Blythe, P.; Roth, B.; Fröhlich, U.; Wenz, H.; Schiller, S. Production of Ultracold Trapped Molecular Hydrogen Ions. *Phys. Rev. Lett.* **2005**, *95*, 183002.
 29. Ostendorf, A.; Zhang, C. B.; Wilson, M.; Offenberg, D.; Roth, B.; Schiller, S. Sympathetic Cooling of Complex Molecular Ions to Millikelvin Temperatures. *Phys. Rev. Lett.* **2006**, *97*, 243005.
 30. Wolk, A. B.; Leavitt, C. M.; Garand, E.; Johnson, M. A. Cryogenic Ion Chemistry and Spectroscopy. *Acc. Chem. Res.* **2013**, *47*, 202–210.
 31. Weinstein, J. D.; Guillet, T.; Friedrich, B.; Doyle, J. M. Magnetic Trapping of Calcium Monohydride Molecules at Millikelvin Temperatures. *Nature* **1998**, *395*, 148–150.
 32. Kirste, M.; Sartakov, B. G.; Schnell, M.; Meijer, G. Nonadiabatic Transitions in Electrostatically Trapped Ammonia Molecules. *Phys. Rev. A* **2009**, *79*, 051401.
 33. Heiner, C. E.; Carty, D.; Meijer, G.; Bethlem, H. L. A Molecular Synchrotron. *Nat. Phys.* **2007**, *3*, 115–118.
 34. Friedrich, B.; Herschbach, D. Alignment and Trapping of Molecules in Intense Laser Fields. *Phys. Rev. Lett.* **1995**, *74*, 4623–4626.
 35. Takekoshi, T.; Patterson, B.; Knize, R. Observation of Optically Trapped Cold Cesium Molecules. *Phys. Rev. Lett.* **1998**, *81*, 5105–5108.
 36. Danzl, J. G.; Mark, M. J.; Haller, E.; Gustavsson, M.; Hart, R.; Aldegunde, J.; Hutson, J. M.; Nägerl, H.-C. An Ultracold High-Density Sample of Rovibronic Ground-State Molecules in an Optical Lattice. *Nat. Phys.* **2010**, *6*, 265–270.
 37. Parker, D. H.; Bernstein, R. B. Oriented Molecule Beams via the

- Electrostatic Hexapole: Preparation, Characterization, and Reactive Scattering. *Annu. Rev. Phys. Chem.* **1989**, *40*, 561–595.
38. Cho, V. A.; Bernstein, R. B. Tight Focusing of Beams of Polar Polyatomic Molecules via the Electrostatic Hexapole Lens. *J. Phys. Chem.* **1991**, *95*, 8129–8136.
 39. Brooks, P. R. Orientation Effects in Electron Transfer Collisions. *Int. Rev. Phys. Chem.* **1995**, *14*, 327–354.
 40. Friedrich, B.; Herschbach, D. Manipulating Molecules via Combined Static and Laser Fields. *J. Phys. Chem. A* **1999**, *103*, 10280–10288.
 41. Friedrich, B.; Herschbach, D. Enhanced Orientation of Polar Molecules by Combined Electrostatic and Nonresonant Induced Dipole Forces. *J. Chem. Phys.* **1999**, *111*, 6157–6160.
 42. Härtelt, M.; Friedrich, B. Directional States of Symmetric-Top Molecules Produced by Combined Static and Radiative Electric Fields. *J. Chem. Phys.* **2008**, *128*, 224313.
 43. Rosca-Pruna, F.; Vrakking, M. Experimental Observation of Revival Structures in Picosecond Laser-Induced Alignment of I₂. *Phys. Rev. Lett.* **2001**, *87*, 153902.
 44. Lee, K. F.; Legare, F.; Villeneuve, D.; Corkum, P. Measured Field-Free Alignment of Deuterium by Few-Cycle Pulses. *J. Phys. B* **2006**, *39*, 4081–4086.
 45. Lemeshko, M.; Krems, R. V.; Doyle, J. M.; Kais, S. Manipulation of Molecules with Electromagnetic Fields. *Mol. Phys.* **2013**, *111*, 1648–1682.
 46. Friedrich, B.; Herschbach, D. R. Spatial Orientation of Molecules in Strong Electric Fields and Evidence for Pendular States. *Nature* **1991**, *353*, 412–414.

47. Friedrich, B.; Herschbach, D. R. On the Possibility of Orienting Rotationally Cooled Polar Molecules in an Electric Field. *Z. Phys. D* **1991**, *18*, 153–161.
48. Friedrich, B.; Pullman, D. P.; Herschbach, D. R. Alignment and Orientation of Rotationally Cool Molecules. *J. Phys. Chem.* **1991**, *95*, 8118–8129.
49. Rost, J. M.; Griffin, J. C.; Friedrich, B.; Herschbach, D. R. Pendular States and Spectra of Oriented Linear Molecules. *Phys. Rev. Lett.* **1992**, *68*, 1299–1302.
50. Block, P. A.; Bohac, E. J.; Miller, R. E. Spectroscopy of Pendular States: The Use of Molecular Complexes in Achieving Orientation. *Phys. Rev. Lett.* **1992**, *68*, 1303–1306.
51. Wei, Q.; Kais, S.; Friedrich, B.; Herschbach, D. Entanglement of Polar Symmetric Top Molecules as Candidate Qubits. *J. Chem. Phys.* **2011**, *135*, 154102.
52. Moore, D. T.; Oudejans, L.; Miller, R. Pendular State Spectroscopy of an Asymmetric Top: Parallel and Perpendicular Bands of Acetylene-HF. *J. Chem. Phys.* **1999**, *110*, 197–208.
53. Li, H.; Franks, K. J.; Hanson, R. J.; Kong, W. Brute Force Orientation and Alignment of Pyridazine Probed by Resonantly Enhanced Multiphoton Ionization. *J. Phys. Chem. A* **1998**, *102*, 8084–8090.
54. Kong, W.; Bulthuis, J. Orientation of Asymmetric Top Molecules in a Uniform Electric Field: Calculations for Species without Symmetry Axes. *J. Phys. Chem. A* **2000**, *104*, 1055–1063.
55. Loesch, H. J.; Remscheid, A. Brute Force in Molecular Reaction Dynamics: A Novel Technique for Measuring Steric Effects. *J. Chem. Phys.* **1990**, *93*, 4779–4790.

56. Loesch, H. J. Orientation and Alignment in Reactive Beam Collisions: Recent Progress. *Annu. Rev. Phys. Chem.* **1995**, *46*, 555–594.
57. Loesch, H. J.; Möller, J. Reactive Scattering from Brute Force Oriented Molecules: $K^+ IR \rightarrow KI + R$ ($R = i\text{-C}_3\text{H}_7$ and $t\text{-C}_4\text{H}_9$). *J. Phys. Chem. A* **1998**, *102*, 9410–9419.
58. Bemish, R. J.; Chan, M. C.; Miller, R. E. Molecular Control Using dc Electric Fields: Quenching of the Tunneling in HF Dimer. *Chem. Phys. Lett.* **1996**, *251*, 182–188.
59. Nauta, K.; Moore, D. T.; Miller, R. E. Molecular Orientation in Superfluid Liquid Helium Droplets: High Resolution Infrared Spectroscopy as a Probe of Solvent–Solute Interactions. *Faraday Discuss.* **1999**, *113*, 261–278.
60. Dong, F.; Miller, R. Vibrational Transition Moment Angles in Isolated Biomolecules: A Structural Tool. *Science* **2002**, *298*, 1227–1230.
61. Choi, M. Y.; Miller, R. E. Four Tautomers of Isolated Guanine from Infrared Laser Spectroscopy in Helium Nanodroplets. *J. Am. Chem. Soc.* **2006**, *128*, 7320–7328.
62. Andrews, S. S.; Boxer, S. G. Vibrational Stark Effects of Nitriles I. Methods and Experimental Results. *J. Phys. Chem. A* **2000**, *104*, 11853–11863.
63. Andrews, S. S.; Boxer, S. G. Vibrational Stark Effects of Nitriles II. Physical Origins of Stark Effects from Experiment and Perturbation Models. *J. Phys. Chem. A* **2002**, *106*, 469–477.
64. Park, E. S.; Boxer, S. G. Origins of the Sensitivity of Molecular Vibrations to Electric Fields: Carbonyl and Nitrosyl Stretches in Model Compounds and Proteins. *J. Phys. Chem. B* **2002**, *106*, 5800–5806.
65. Suydam, I. T.; Snow, C. D.; Pande, V. S.; Boxer, S. G. Electric Fields at the Active Site of an Enzyme: Direct Comparison of Experiment with Theory.

- Science* **2006**, *313*, 200–204.
66. Fried, S. D.; Bagchi, S.; Boxer, S. G. Extreme Electric Fields Power Catalysis in the Active Site of Ketosteroid Isomerase. *Science* **2014**, *346*, 1510–1514.
 67. Fried, S. D.; Boxer, S. G. Measuring Electric Fields and Noncovalent Interactions Using the Vibrational Stark Effect. *Acc. Chem. Res.* **2015**, *48*, 998–1006.
 68. Shin, S.; Kim, Y.; Kang, H.; Kang, H. Effect of Electric Field on Condensed-Phase Molecular Systems. I. Dipolar Polarization of Amorphous Solid Acetone. *J. Phys. Chem. C* **2015**, *119*, 15588–15595.
 69. Shin, S.; Kang, H.; Cho, D.; Lee, J. Y.; Kang, H. Effect of Electric Field on Condensed-Phase Molecular Systems. II. Stark Effect on the Hydroxyl Stretch Vibration of Ice. *J. Phys. Chem. C* **2015**, *119*, 15596–15603.
 70. Shin, S.; Park, Y.; Kang, H.; Kang, H. Electric Field Effect on Condensed-Phase Molecular Systems. IV. Conformational Change of 1, 2-Dichloroethane in a Frozen Molecular Solid. *J. Phys. Chem. C* **2017**, *121*, 25342–25346.
 71. Shin, S.; Park, Y.; Kang, H.; Kang, H. Electric Field Effect on Condensed-Phase Molecular Systems: V. Acid–Base Proton Transfer at the Interface of Molecular Films. *J. Phys. Chem. C* **2018**, *122*, 4901–4907.

Chapter 2

Method

2.1. A Combined Technique of Ice Film Nanocapacitor and Matrix Isolation

To experimentally study the behavior of molecules or molecular clusters under the influence of external fields, they should be isolated from other molecules. One of the simple ways to provide the molecules or clusters such circumstance is to conduct experiments in the gas phase. There have been several studies which explored the effect of electric fields on the gas-phase molecules or those trapped in helium (He) nanodroplets [1–7]. To apply homogenous external electrostatic fields, the gas-phase studies utilized the conventional parallel metal plate capacitor, the fields applied by which were only moderately strong (10^6 V/m order) such that the observations were limited to small field-driven changes.

When it comes to the condensed phase, the applicable field strength becomes substantially larger. Boxer and coworkers reported the vibrational Stark effect spectroscopy on the frozen molecular films under the field strength of 10^8 V/m [8–12]. In the group of Kang, a method called the ice film nanocapacitor was recently developed to apply external electrostatic fields up to about 4×10^8 V/m across the ice and other kinds of molecular films [13–17]. In these condensed-phase Stark experiments, the strength of external fields is rather strong but the molecules in the condense phase interact with neighboring molecules with much larger extent, which restricts the proper examination of molecular behaviors under the influence of

external fields.

Applying the external fields using the ice film nanocapacitor across the molecules or molecular clusters isolated in the inert matrices satisfies both requirements: the isolation of molecules or molecular clusters from neighboring molecules and the capability of employing intense external electrostatic fields in the condensed phase. The combination of the ice film nanocapacitor method with matrix-isolation technique has been verified to enable the exploration on field-induced manipulation of molecular properties including orientation, molecular states, and internal dynamics [18–21].

Starting from the pioneering work of G. C. Pimentel [22], the matrix-isolation method has been widely used in the spectroscopic studies on the unstable, transient species, with the help of the rapid development of low temperature technique [23]. The molecules or molecular clusters are isolated by co-adsorbing the gas of target molecules with the matrix gas on the cold substrate (spectroscopic lens or mirror) in pressure ratios on the order of 1:1000. Most commonly used matrix has been traditionally nitrogen (N_2) and argon (Ar) which are generally regarded as inert species. Neon (Ne) and *para*-hydrogen (*p*- H_2) joined the list with better cryogenic technique available recently. Except for the *p*- H_2 matrix which is known to have a quantum behavior, the cold solid matrices are rigid with respect to diffusion, enabling the preparation of well-defined molecules or molecular clusters inside the matrices.

The matrix-isolated species are readily detected with spectroscopic tools since most of the matrices are transparent in the spectral region of interest (usually infrared). From the point of view of an isolated molecule, the influence of surrounding matrix is not significant, and thereby the properties of the molecule resemble those of the gas-phase molecule. The vibrational frequencies of a matrix-

isolated molecule are similar to the gas phase frequencies. In addition, the absorption features in spectra are sharp compared to those in the conventional liquid or solid spectroscopy. In the case of large molecules or clusters isolated in the rigid matrices, contrary to gas-phase vibrational spectroscopy, the rotational features do not appear in the spectra. Instead, the resultant sharpened absorption at vibrational fundamentals allow better interpretation on the molecular properties and behavior under the influence of external perturbations.

Though the influence of the inert matrices on the isolated species is generally regarded to be small, limitations of the matrix-isolation technique mainly originate from the non-negligible matrix effect. Compared to gas-phase or He nanodroplet spectroscopy, the matrix-shift, defined as the discrepancy in vibrational frequencies between matrix-isolated species and gas-phase species, is apparent. Ab initio calculations are generally employed in the molecular spectroscopy, but the matrix effect is not easy to be included in the calculations. In the case of Ar matrix which is mostly used in the experiments introduced in this dissertation, it has been thought to have a face-centered cubic lattice structure with a molecule trapped in a substitutional site. The diameter of a singly-substitutional spherical cavity of Ar lattice was estimated to be 3.755 Å at 4 K or 3.760 Å at 20 K. For a molecule whose size is comparable or slightly smaller, it is thought to locate inside the singly-substitutional site with 12 nearest neighboring Ar atoms. There could be, however, different trapping sites for smaller or larger molecules or molecular clusters. For small molecules, they can be trapped in the octahedral (O_h) and tetrahedral (T_d) interstitial site, whose diameters are 1.56 Å and 0.85 Å, respectively, in the case of Ar matrix. For larger molecules or molecular clusters, they require the substitution of two or more Ar atoms to be trapped inside the lattice. There even can be multiple trapping sites for one kind of molecule. In general, the information on the trapping

sites is properly postulated based on the size and spectroscopic properties of the isolated molecules.

The ice film nanocapacitor method utilizes the fact that the large Cs^+ ions thermodynamically prefer to locate on the surface of ice instead of being inside the bulk [13]. On top of the matrix which isolates the target molecules or clusters, amorphous solid water film is prepared to accommodate Cs^+ ions on the surface. Low energy (< 30 eV) Cs^+ ions are soft-landed on the surface of ice to prevent the surface sputtering and introduced with a de-focused trajectory to guarantee the uniform surface distribution. Once the Cs^+ ions are introduced, the equivalent amount of negative charges is derived on the surface of a metal substrate on which the matrix and ice films are adsorbed sequentially. This system forms a plate capacitor with the nanoscale separation of opposite charges. The electric fields formed across the nanocapacitor have a strength on 10^8 V/m scale. To increase the strength of field, the amount of Cs^+ ions on the ice surface is increased. To decrease the field strength, low energy (< 5 eV) electrons are introduced to compensate the positive charge of Cs^+ ions at the surface.

The strength of external fields applied by means of the ice film nanocapacitor is estimated based on the film voltage measurement with a Kelvin probe and the film thickness measurement with temperature-programmed desorption (TPD) spectrometry. The strength of the macroscopic field (F_0) that is applied across the Ar matrix is determined from the film voltage (V_{film}) developed as a consequence of Cs^+ by considering the division of the voltage between the Ar matrix and the ice layer.

$$F_0 = \frac{V_{\text{film}}}{d_{\text{Ar}} + d_{\text{ice}} \frac{\epsilon_{\text{Ar}}}{\epsilon_{\text{ice}}}} \quad \text{eq. (2-1)}$$

Here, d_{Ar} and d_{ice} are the thicknesses of the Ar and ice layers, respectively. The

relative permittivity of each dielectric layer is $\varepsilon_{Ar} = 1.6$ and $\varepsilon_{ice} = 2.0$ [24, 25].

The actual field (\mathbf{F}) that a matrix-isolated molecule or cluster experiences, also called the local field, is stronger than the macroscopic field (\mathbf{F}_0) according to classical electrostatics and the reaction field theory proposed by L. Onsager [26, 27]. The correction factor (c_{local}) which relates the local field and macroscopic field can be estimated by assuming that the isolated molecule is located inside a spherical cavity of the dielectric continuum of the matrix (Onsager model). Two factors are involved: the cavity field and the reaction field.

The cavity field is the field inside a spherical cavity in a dielectric. When a uniform macroscopic field is applied to a dielectric with relative permittivity ε , the cavity field (\mathbf{F}_c) is expressed as eq. (2-2) by solving Laplace's equation.

$$\mathbf{F}_c = \frac{3\varepsilon}{2\varepsilon+1} \mathbf{F}_0 \quad \text{eq. (2-2)}$$

The reaction field, in general, is defined as the field exerted on a dipole inside the cavity by surrounding matter that is polarized by an inhomogeneous field of the dipole. According to Onsager, the reaction field is proportional to the dipole moment and is inversely proportional to the size of the cavity. The reaction field (\mathbf{R}) is expressed as $\mathbf{R} = f\boldsymbol{\mu}$, where $\boldsymbol{\mu}$ is the dipole moment and f is the reaction field factor. The reaction field factor is expressed as eq. (2-3).

$$f = \frac{1}{a^3} \frac{2(\varepsilon-1)}{2\varepsilon+1} \quad \text{eq. (2-3)}$$

Here, a is the radius of the cavity. A macroscopic field generates the reaction field which is parallel to the macroscopic field by creating the induced dipole ($\alpha\mathbf{F}$) of the trapped molecule, where α is the polarizability. Therefore, the reaction field generated by a macroscopic field is $\mathbf{R} = f\alpha\mathbf{F}$.

With both contributions from the cavity field and the reaction field, the local field (\mathbf{F}) is given by the eq. (2-4, 2-5):

$$\mathbf{F} = \mathbf{F}_c + f\alpha\mathbf{F} \quad \text{eq. (2-4)}$$

or

$$\mathbf{F} = \frac{1}{1-f\alpha} \mathbf{F}_c = \frac{1}{1-f\alpha} \frac{3\varepsilon}{2\varepsilon+1} \mathbf{F}_0 \quad \text{eq. (2-5)}$$

The real circumstance would be different for the matrix-isolated molecules or clusters, as being surrounded by discrete Ar atoms with an uncertain shape and size of the cavity. Therefore, the local field correction factor has been practiced in many previous reports of the vibrational Stark effect of molecules to be left as c_{local} , instead of a specific value. Generally, c_{local} is thought to be in the range of 1–2 depending on the system [12, 18].

2.2. Reflection–Absorption Infrared Spectroscopy of Matrix-Isolated Molecules under the Influence of External Fields

Vibrational spectroscopy is a powerful tool to investigate the changes in molecular states owing to the sensitiveness of molecular vibration to the environment. For instance, a slight change in the bond properties induced by any perturbations is immediately reflected in the frequency of stretching vibration of the specific bond. Besides, the molecular vibration is a vector quantity, enabling the detection of molecular orientation by using a polarized beam.

To study the molecules and clusters isolated in the nanoscopic film of inert matrices formed on the surface of a metal substrate, reflection–absorption infrared spectroscopy (RAIRS) was used. In contrast to conventional transmittance IR spectroscopy where the absorbance is determined from the difference in the intensity of transmitted beam with and without the sample, the absorbance is measured from

the difference in reflectance with and without the target film on the metal surface in RAIRS. To maximize the sensitivity of the detection, the p-polarized infrared beam with a grazing angle close to 87° is almost invariably utilized [28]. In the case of s-polarized beam, a complete out-of-phase reflection at the metal surface results in the destructive interference of the light. For p-polarized light, the grazing-angle reflection at the metal surface gives rise to an enhancement of the surface normal component [28, 29]. Because the absorption of polarized light by an oscillator is proportional to $\cos^2\theta$ where θ is the angle of transition dipole moment with respect to the polarization of detecting light, the vibrations with their dipoles directing perpendicular to the surface are selectively detected in the RAIR spectroscopic measurements with the p-polarized incident beam.

In the experimental scheme used in the present dissertation study, the external electrostatic field applied across the film is normal to the surface [13], and therefore collinear with the polarization of the IR beam. This serves as an indisputable advantage for the observation of field-induced manipulations of matrix-isolated molecules and clusters. For small molecules that could reorient into the direction of external fields inside the matrix, the change of absorbance is a direct indication of molecular orientation under the influence of fields. Assuming that the orientation distribution of a polar molecule follows Boltzmann distribution with dipolar potential energy, $u = \mu F \cos\theta$, where μ is the permanent dipole moment of the molecule, F is the field strength, and θ is the angle between the dipole moment and the field, absorbance of the vibration with the transition dipole collinear to the permanent dipole moment is expected to be:

$$A = \frac{\int_0^\pi |\cos\theta|^2 e^{\mu F \cos\theta / k_B T} \sin\theta \, d\theta}{\int_0^\pi e^{\mu F \cos\theta / k_B T} \sin\theta \, d\theta} = 1 - \frac{2}{\beta} \left(\coth\beta - \frac{1}{\beta} \right) \quad \text{eq. (2-6)}$$

where $\beta = \mu F / k_B T$, with T the temperature of the film and k_B the Boltzmann

constant. The relation was confirmed for the C=O stretching vibration of the matrix-isolated formaldehyde (CH₂O) molecule which underwent a reorientation under the influence of external fields [18].

For even smaller molecules which rotate nearly freely inside the matrix, such as hydrogen chloride (HCl) and water (H₂O) [19, 20], they in general show rotational structures in the vibrational spectra. When the external fields are applied to these molecules, the rotational motion transforms into the pendular-like motion. The rotational energy levels at zero field evolve into the pendular states under fields, and ultimately toward the harmonic libration limit at extreme [30–33], which is responsible for the spectral changes [1, 34]. The collinearity between the static and radiative fields results in the transition selection rule which expects the considerably intensified transition at the vibrational band origin. This enabled the observation of vibrational transitions and measurement of vibrational Stark sensitivities of molecules including HCl and H₂O, which would not be feasible without the spatial orientation driven by the strong external fields collinear with the radiative field, due to the weak oscillator strengths. An example of field-driven manipulation of internal dynamics of molecule was also observed for ammonia (NH₃) with the help of the substantial amount of spatial orientation achieved in the methodology [21].

For larger molecules or molecular clusters which are unable to change the orientation in the rigid matrices under external fields, vibrational bands are subjected to broadening without significant change of intensity. Strong external fields modify the potential energy surface, resulting in the change of frequency in vibrational spectra. In general, this is called the vibrational Stark effect [8, 9]. The band broadening is expected for the molecules or clusters which have an isotropic distribution of orientation, as a result of the vibrational Stark effect by external fields that are collinear with the radiative field. As mentioned earlier, since they are trapped

in the rigid cage of solid matrices, the molecules and clusters show relatively sharp bands in IR spectra which are purely vibrational without hindrance of rotational structures. This feature provides a benefit in spectral interpretation.

2.3. Instruments

All experiments described in this dissertation were conducted inside an ultrahigh vacuum (UHV) chamber. The stainless-steel chamber was vacuum-pumped with turbomolecular pumps (TMP; Leybold) backed by rotary vane pumps (Edwards) to maintain the base pressure on the order of 10^{-10} torr. The pressure inside the chamber was monitored by a hot-filament ionization gauge (Granville-Phillips). In the center of the chamber, a platinum (Pt) substrate with a well-defined (111) surface was located. The Pt substrate was held by a home-designed sample holder made of vacuum-compatible copper which is connected to a sample manipulator (McAllister), enabling the rotation and translation of the substrate for a certain extent. The Pt substrate had a thermal contact with a closed-cycle helium cryocooler (coldhead: Coldedge CH-204SN, compressor: Sumitomo HC-4E1) which enabled to cool the temperature of the substrate down to ~ 10 K. The Pt substrate was electrically floated so that the voltage could be biased with respect to the electrical ground. The molecular films were prepared on the Pt surface by sequential deposition of the corresponding gaseous species introduced through variable leak valves into the UHV chamber. Some gases which might seriously contaminate the vacuum were guided to the surface with tube dosers. For *in situ* analysis of the films, the chamber was equipped with a Fourier-transform infrared (FTIR) spectrometer (Bruker Vertex 70), a quadrupole mass spectrometer (Extrel), a Kelvin probe (McAllister KP6500) for

film voltage measurements, and a low-energy Cs^+ ion gun (Kimball Physics Inc.).

The matrix-isolation was achieved by co-adsorbing the gases of target molecules and the matrix gas (Ar) with a much higher pressure, where each gas was introduced into the chamber through an individual leak valve. The pressure ratio of the guest and the host was on the order of 1:1000. During the co-adsorption, the pressure of Ar gas was monitored with the ionization gauge. The pressure of the guest, which was about three orders of magnitude smaller than that of Ar and therefore was difficult to be quantitated with the ionization gauge during the co-adsorption, was monitored by the mass spectrometer on a residual gas analyzer mode.

The temperature was measured by using a type N thermocouple (Nicrosil–Nisil) spot-welded on the substrate. The molecular films on the Pt substrate was heated with high-energy (2 keV) electron bombardment. A home-built electron gun located in the rear side of the Pt substrate enabled to increase the temperature up to about 1200 K. The temperature of the sample was maintained or linearly ramped with a PID controller (Eurotherm) by means of modifying the amount of electron emission from the electron gun. Taking advantage of this elaborate temperature control and the quadrupole mass spectrometer, a temperature-programmed desorption (TPD) spectrometry was available even at low temperature of ~ 10 K. The surface of the Pt substrate was cleaned before every experiment by 2 kV Ar^+ ion sputtering followed by several 1200 K annealing cycles.

Reflection–absorption infrared spectroscopic (RAIRS) measurements were conducted using a Fourier-transform infrared (FTIR) spectrometer with a liquid nitrogen-cooled mercury–cadmium–telluride (MCT) detector (Infrared Associates Inc. ID316-L). The incident IR beam was focused by mirrors and p-polarized by a wire grid polarizer (Specac GS57510). The IR beam passed into the UHV chamber through a zinc selenide (ZnSe) viewport, reflected at the surface of the Pt substrate

with the grazing angle ($\sim 85^\circ$), passed out of the chamber through another ZnSe viewport, and arrived at the MCT detector. The beam path outside the UHV chamber was purged with dry nitrogen gas. The RAIR spectra were acquired at spectral resolution of $0.5\text{--}4\text{ cm}^{-1}$ in spectral range of $650\text{--}4000$ (or 5000) cm^{-1} . The aperture size of the beam ($3\text{--}6\text{ mm}$) and phase resolution ($4\text{--}16$) were adjusted accordingly with the spectral resolution. The spectra were averaged $256\text{--}1024$ times.

References

1. Block, P. A.; Bohac, E. J.; Miller, R. E. Spectroscopy of Pendular States: The Use of Molecular Complexes in Achieving Orientation. *Phys. Rev. Lett.* **1992**, *68*, 1303–1306.
2. Nauta, K.; Moore, D. T.; Miller, R. E. Molecular Orientation in Superfluid Liquid Helium Droplets: High Resolution Infrared Spectroscopy as a Probe of Solvent–Solute Interactions. *Faraday Discuss.* **1999**, *113*, 261–278.
3. Nauta, K.; Miller, R. E. Nonequilibrium Self-Assembly of Long Chains of Polar Molecules in Superfluid Helium. *Science* **1999**, *283*, 1895–1897.
4. Toennies, J. P.; Vilesov, A. F. Superfluid Helium Droplets: A Uniquely Cold Nanomatrix for Molecules and Molecular Complexes. *Angew. Chem. Int. Ed.* **2004**, *43*, 2622–2648.
5. Choi, M.; Dong, F.; Miller, R. Multiple Tautomers of Cytosine Identified and Characterized by Infrared Laser Spectroscopy in Helium Nanodroplets: Probing Structure Using Vibrational Transition Moment Angles. *Philos. Trans. Royal Soc. A* **2004**, *363*, 393–413.
6. Choi, M. Y.; Douberly, G. E.; Falconer, T. M.; Lewis, W. K.; Lindsay, C. M.; Merritt, J. M.; Stiles, P. L.; Miller, R. E. Infrared Spectroscopy of Helium Nanodroplets: Novel Methods for Physics and Chemistry. *Int. Rev. Phys. Chem.* **2006**, *25*, 15–75.
7. Choi, M. Y.; Miller, R. E. Infrared Laser Spectroscopy of Imidazole Complexes in Helium Nanodroplets: Monomer, Dimer, and Binary Water Complexes. *J. Phys. Chem. A* **2006**, *110*, 9344–9351.
8. Andrews, S. S.; Boxer, S. G. Vibrational Stark Effects of Nitriles I. Methods

- and Experimental Results. *J. Phys. Chem. A* **2000**, *104*, 11853–11863.
9. Andrews, S. S.; Boxer, S. G. Vibrational Stark Effects of Nitriles II. Physical Origins of Stark Effects from Experiment and Perturbation Models. *J. Phys. Chem. A* **2002**, *106*, 469–477.
 10. Saggu, M.; Levinson, N. M.; Boxer, S. G. Direct Measurements of Electric Fields in Weak OH $\cdots\pi$ Hydrogen Bonds. *J. Am. Chem. Soc.* **2011**, *133*, 17414–17419.
 11. Saggu, M.; Levinson, N. M.; Boxer, S. G. Experimental Quantification of Electrostatics in X–H $\cdots\pi$ Hydrogen Bonds. *J. Am. Chem. Soc.* **2012**, *134*, 18986–18997.
 12. Fried, S. D.; Boxer, S. G. Measuring Electric Fields and Noncovalent Interactions Using the Vibrational Stark Effect. *Acc. Chem. Res.* **2015**, *48*, 998–1006.
 13. Shin, S.; Kim, Y.; Moon, E.-s.; Lee, D. H.; Kang, H.; Kang, H. Generation of Strong Electric Fields in an Ice Film Capacitor. *J. Chem. Phys.* **2013**, *139*, 074201.
 14. Shin, S.; Kim, Y.; Kang, H.; Kang, H. Effect of Electric Field on Condensed-Phase Molecular Systems. I. Dipolar Polarization of Amorphous Solid Acetone. *J. Phys. Chem. C* **2015**, *119*, 15588–15595.
 15. Shin, S.; Kang, H.; Cho, D.; Lee, J. Y.; Kang, H. Effect of Electric Field on Condensed-Phase Molecular Systems. II. Stark Effect on the Hydroxyl Stretch Vibration of Ice. *J. Phys. Chem. C* **2015**, *119*, 15596–15603.
 16. Shin, S.; Park, Y.; Kang, H.; Kang, H. Electric Field Effect on Condensed-Phase Molecular Systems. IV. Conformational Change of 1,2-Dichloroethane in a Frozen Molecular Solid. *J. Phys. Chem. C* **2017**, *121*, 25342–25346.

17. Shin, S.; Park, Y.; Kang, H.; Kang, H. Electric Field Effect on Condensed-Phase Molecular Systems: V. Acid–Base Proton Transfer at the Interface of Molecular Films. *J. Phys. Chem. C* **2018**, *122*, 4901–4907.
18. Park, Y.; Kang, H.; Kang, H. Brute Force Orientation of Matrix-Isolated Molecules: Reversible Reorientation of Formaldehyde in an Argon Matrix toward Perfect Alignment. *Angew. Chem. Int. Ed.* **2017**, *56*, 1046–1049.
19. Kang, H.; Park, Y.; Kim, Z. H.; Kang, H. Electric Field Effect on Condensed-Phase Molecular Systems. VI. Field-Driven Orientation of Hydrogen Chloride in an Argon Matrix. *J. Phys. Chem. A* **2018**, *122*, 2871–2876.
20. Park, Y.; Lim, J. H.; Lee, J. Y.; Kang, H. Electric Field Effect on Condensed-Phase Molecular Systems. VII. Vibrational Stark Sensitivity of Spatially Oriented Water Molecules in an Argon Matrix. *J. Phys. Chem. C* **2019**, *123*, 9868–9874.
21. Park, Y.; Kang, H.; Field, R. W.; Kang, H. The Frequency-Domain IR Spectrum of Ammonia Encodes Changes in Molecular Dynamics Caused by a DC Electric Field. *Proc. Natl. Acad. Sci. U.S.A.* **2019**, *116*, 23444–23447.
22. Whittle, E.; Dows, D. A.; Pimentel, G. C. Matrix Isolation Method for the Experimental Study of Unstable Species. *J. Chem. Phys.* **1954**, *22*, 1943.
23. Hallam, H. E. *Vibrational Spectroscopy of Trapped Species*; Wiley: Hoboken, 1973.
24. Marcoux, J. Dielectric Constants and Indices of Refraction of Xe, Kr, and Ar. *Can. J. Phys.* **1970**, *48*, 244–245.
25. Tsekouras, A. A.; Iedema, M. J.; Cowin, J. P. Amorphous Water-Ice Relaxations Measured with Soft-Landed Ions. *Phys. Rev. Lett.* **1998**, *80*,

- 5798–5801.
26. Onsager, L. Electric Moments of Molecules in Liquids. *J. Am. Chem. Soc.* **1936**, *58*, 1486–1493.
 27. Böttcher, C. J. F. *Theory of Electric Polarization*; Elsevier: Amsterdam, NY, 1973.
 28. Griffiths, P. R.; De Haseth, J. A. *Fourier Transform Infrared Spectrometry*, 2nd ed.; Wiley: Hoboken, 2007, pp. 277–301.
 29. Golden, W. G.; Saperstein, D. D.; Severson, M. W.; Overend, J. Infrared Reflection-Absorption Spectroscopy of Surface Species: A Comparison of Fourier Transform and Dispersion Methods. *J. Phys. Chem.* **1984**, *88*, 574–580.
 30. Rost, J. M.; Griffin, J. C.; Friedrich, B.; Herschbach, D. R. Pendular States and Spectra of Oriented Linear Molecules. *Phys. Rev. Lett.* **1992**, *68*, 1299–1302.
 31. Maergoiz, A.; Troe, J. Weak- and Strong-Field Stark Energy Levels of Symmetric Top Dipolar Molecules. *J. Chem. Phys.* **1993**, *99*, 3218–3223.
 32. Kanya, R.; Ohshima, Y. Pendular-Limit Representation of Energy Levels and Spectra of Symmetric- and Asymmetric-Top Molecules. *Phys. Rev. A* **2004**, *70*, 013403.
 33. Härtelt, M.; Friedrich, B. Directional States of Symmetric-Top Molecules Produced by Combined Static and Radiative Electric Fields. *J. Chem. Phys.* **2008**, *128*, 224313.
 34. Moore, D. T.; Oudejans, L.; Miller, R. Pendular State Spectroscopy of an Asymmetric Top: Parallel and Perpendicular Bands of Acetylene-HF. *J. Chem. Phys.* **1999**, *110*, 197–208.

Chapter 3

Electric Field-Control of Inversion Dynamics of Ammonia in an Argon Matrix

Abstract

Ammonia is special. It is non-planar, yet it has a zero permanent electric dipole moment. It is a favorite pedagogical example of tunneling in a symmetric double-minimum potential. Tunneling is a dynamical concept, yet the quantitative characteristics of tunneling are expressed in a static, eigenstate-resolved spectrum. The inverting-umbrella tunneling motion in ammonia is both large-amplitude and profoundly affected by an external electric field. We report how a uniquely strong (up to 10^8 V/m) DC electric field causes a richly detailed sequence of reversible changes in the frequency-domain infrared spectrum (the $\nu=0 \rightarrow 1$ ν_2 umbrella-mode transition) of ammonia, freely rotating in a 10 K Ar matrix. Although the spectrum is *static*, encoded in it is the complete inter- and intra-molecular picture of tunneling *dynamics*.

3.1. Introduction

Ammonia is a textbook example of a symmetric top rotor molecule with a highly fluxional inversion motion. The ro-vibrational energy levels of free NH_3 are split due to inversion tunneling through the barrier along the ν_2 umbrella mode vibrational coordinate. With an energy barrier of about 2000 cm^{-1} in the symmetric double-minimum potential, the inversion splitting is 0.79 cm^{-1} for the vibrational ground state and 36 cm^{-1} for the $\nu=1$ of the ν_2 mode [1]. Energy level diagrams for ammonia can be found in the literature [2, 3].

The ammonia molecule is known to behave similarly in the gas phase and in inert gas matrices. The matrix-isolated ammonia monomer is nearly a free rotor and also undergoes inversion tunneling [4–6]. The sum of the inversion splitting in the vibrational ground and excited states is different for ammonia molecules in the gas-phase ($0.79\text{ cm}^{-1} + 36\text{ cm}^{-1}$) and in the Ar matrix (about 24 cm^{-1}) [4]. Ro-vibrational peaks observed in the IR spectra of matrix-isolated ammonia corresponds to transitions between the inversion-rotation-vibration energy levels. These transitions are governed by the same selection rules as in the gas phase. The selection rules for the vibrational and rotational transitions are well known: $\Delta\nu=\pm 1$ for the vibrational transition, and $\Delta J=\pm 1$ (for $K=0$) or $\Delta J=0, \pm 1$ (for $K\neq 0$) and $\Delta K=0$ for all rotational transitions of a rigid rotor symmetric top. For the inversion transition in a symmetric top rotor, only transitions between + and - inversion symmetries are allowed.

Since the proton (H) is a fermion, the inversion-rotation-vibration wavefunctions of NH_3 must be anti-symmetric with respect to the exchange of any two protons. This permutation symmetry requirement results in nuclear spin statistics that gives different weights to inversion-rotation-vibration energy states. According

to the nuclear spin statistics for NH₃, several energy levels are absent. The absent energy levels are + levels for even J and – levels for odd J when $K=3n$ ($n=0, 1, 2, \dots$). For example, denoting inversion–rotation energy levels with a symbol $J_K^{(\text{inversion parity})}$, the states $0_0^+, 1_0^-, 2_0^+, 3_0^-, \dots$ are absent. As a result, the 0_0^- level in the vibrational ground state is the lowest in energy. Taking the relatively large B rotational constant of NH₃ (about 10 cm^{-1} in the gas phase and about 9.4 cm^{-1} in the Ar matrix) into consideration, the dominant transition is expected to be the R(0_0^-) ($[v=0, J=0, K=0, \text{inversion parity } -] \rightarrow [v=1, J=1, K=0, \text{inversion parity } +]$) transition at the low temperature ($\sim 10 \text{ K}$). The next most populated rotational levels are 1_1^+ and 1_1^- (since NH₃ is oblate), meaning that the Q(1_1) or R(1_1) transitions are expected to be the second-strongest transitions.

ND₃ undergoes less efficient tunneling between two wells in the symmetric double-minimum potential. The tunneling rate, i.e. the rate at which the ammonia molecule inverts from one form to the other, is related to the inversion splitting frequency. The time τ for inversion is expressed as $\tau = (2 \Delta\nu)^{-1}$ [7]. The values of τ in the gas phase are $2.1 \times 10^{-11} \text{ s}$ for NH₃, $2.2 \times 10^{-11} \text{ s}$ for ¹⁵NH₃, and $3.1 \times 10^{-10} \text{ s}$ for ND₃. Values of the inversion splitting term (summation of tunneling-splitting in the ground and the first excited vibrational states) are 3.7 cm^{-1} for gas phase ND₃ and about 2 cm^{-1} for ND₃ in the Ar matrix [1, 4].

In this study, strong external electrostatic fields on the order of 10^8 V/m were applied, using the ice film nanocapacitor method, to ammonia molecules isolated in the Ar matrix. The field-driven changes in transitions between inversion–rotation–vibration energy levels of matrix-isolated ammonia were recorded with IR spectroscopy. The spectral changes indicated that the inversion dynamics was quenched for the ammonia molecules which were spatially oriented along the

direction of external fields.

3.2. Experimental Details

The experiments were performed in an ultrahigh vacuum (UHV) chamber, the detailed description of which can be found elsewhere [8, 9]. The molecular film was prepared on a Pt(111) substrate surface maintained at a cryogenic temperature (about 10 K) by sequential deposition of corresponding gases.

D₂O (Aldrich, 99 atom% D) was purified by freeze–pump–thaw cycles. Ar and NH₃ gases were used directly from commercially available gas cylinders. ND₃ were prepared by thermal evaporation of ND₃ molecules from ND₄OD solution (Alfa Aesar, 99 atom% D, 23.0–27.0 wt% sol), utilizing the large vapor pressure of ammonia relative to that of water. NH₂D and NHD₂ were prepared similarly, from a roughly 1:1 mixture of NH₄OH solution (Samchun Chemical Co., Ltd., Korea, 28.0–30.0 wt% sol) and liquid D₂O to give an isotopologue distribution of NH₃:NH₂D:NHD₂:ND₃ = 1:3:3:1.

A thin film sample of matrix-isolated ammonia was prepared by co-deposition of ammonia and Ar gases with a predetermined partial-pressure ratio on the order of 10⁻³. The sample had a stacked structure of an Ar film (144–960 ML thickness; ML = monolayer; 1 ML = 1.1 × 10¹⁵ molecules/cm²) that contained ammonia molecules, sandwiched between two Ar spacer layers (48–120 ML each). The spacer layers prevent the ammonia molecules from being affected by interfacial effects. The upper Ar film was capped by an amorphous D₂O film (25 ML). The thickness of the entire sample was 150–710 nm.

A static electric field was generated across the film using the previously

demonstrated [8, 10] ice film nanocapacitor method. The strength of the externally applied electric field within the Ar matrix was estimated from the film voltage measured with a Kelvin probe. All measured values of field strength given in this paper are the macroscopic field (F_0), estimated simply by dividing voltage across the film by the thickness of the film. The actual field strength (F) that a matrix-isolated molecule experiences is expressed by $F = c_{\text{local}}F_0$, with the local field correction factor, c_{local} , estimated to be in the range of 1–2 [8].

Reflection–absorption infrared spectroscopic (RAIRS) measurements were conducted with a Fourier transform infrared (FTIR) spectrometer with a liquid nitrogen-cooled mercury–cadmium telluride detector in grazing angle reflection geometry (85°). An incident IR beam was p-polarized by a wire grid polarizer. The RAIR spectra were averaged 256 times at a spectral resolution of 1 cm^{-1} .

3.3. Results and Discussion

Figure 3-1(a) shows the RAIR spectrum of matrix-isolated NH_3 in the ν_2 region and its evolution with increasing field strength. In the zero-field spectrum, the peak at about 975 cm^{-1} corresponds to the $\text{R}(0_0^-)$ ro–vibrational transition of the ν_2 mode [4]. Features due to ammonia aggregates (dimer, trimer, etc.) appeared at higher frequencies ($> 990 \text{ cm}^{-1}$, not shown in Figure 3-1(a)) [4, 11] and could be distinguished from the monomer peak by examining their intensity variation with respect to the change in the Ar: NH_3 ratio. The external field induced drastic changes in the frequency, intensity, and shape of the ν_2 band of NH_3 . The $\text{R}(0_0^-)$ peak became slightly red-shifted and a new peak appeared at field strength above $1.3 \times 10^7 \text{ V/m}$, resulting in two peaks at 963 and 972 cm^{-1} . The two peaks tuned closer to each other

as the field increased and eventually merged into a single feature above 4.7×10^7 V/m. The merged peak shifted continuously to the blue with increasing field. In addition, the intensity of the ν_2 band increased as the field strength increased. These changes were reversible with respect to an increase or decrease of field strength.

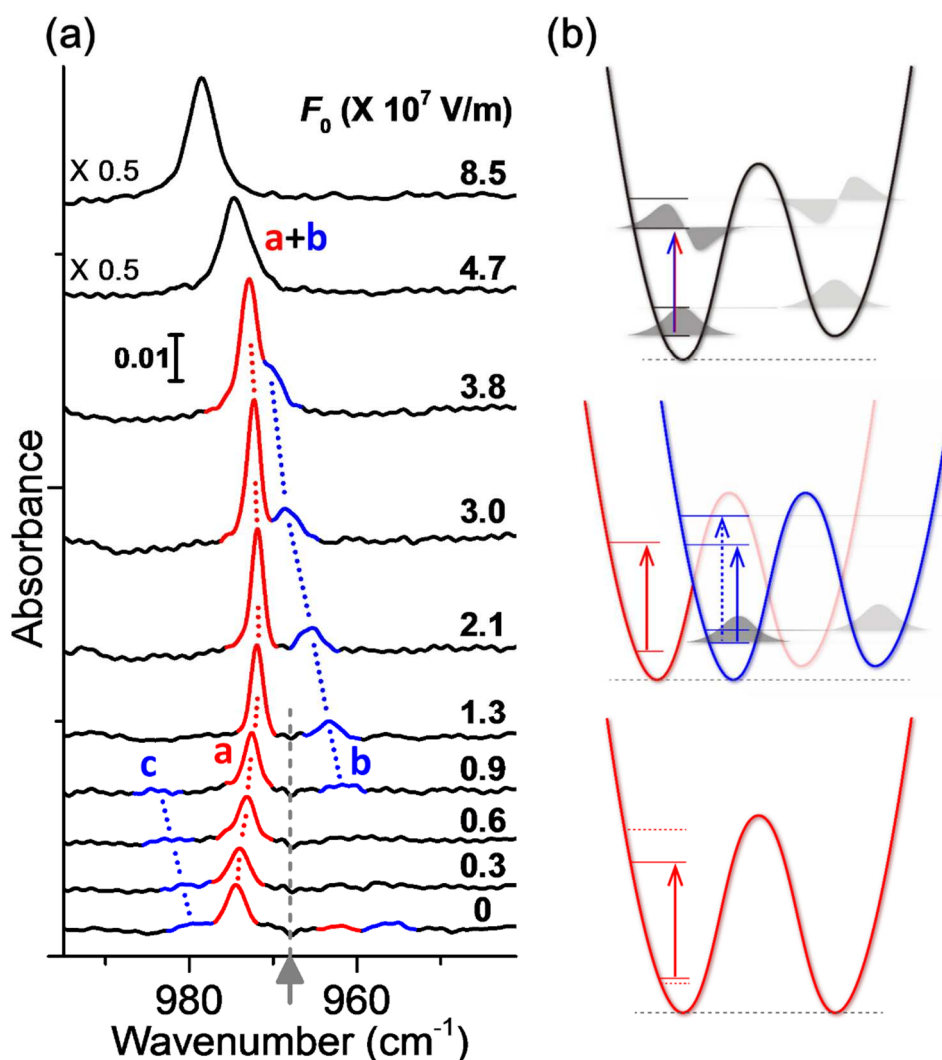


Figure 3-1. (a) RAIR spectra of the ν_2 umbrella vibration of matrix-isolated NH_3 ,

measured as a function of the strength of applied electric field. The $\nu=0\rightarrow 1$ vibrational band origin (968 cm^{-1}) is indicated by the gray arrow. In the spectra, transitions occurring within $K=0$ rotational levels are shown in red, while transitions in $|K|=1$ states are shown in blue. The evolution of peaks induced by the external field is depicted by dotted red and blue lines. (b) Schematic drawings of the double-minimum potential, energy states and allowed transitions at different stages of Stark shifts and mixings. Likewise, the red and blue color-coding indicates features that belong to $K=0$ and $|K|=1$, respectively. (Bottom) A symmetric double-minimum potential at zero field. The transition shown in $R(0_0^-)$, which is prominent at zero field. (Middle) The slightly “tilted” asymmetric double-minimum potential in the intermediate field region. Energy levels and expected transitions are shown for $K=0$ (red) and $|K|=1$ (blue). The red and blue potential curves are identical, but shifted horizontally for clarity. Two strong transitions observed in the intermediate field region are marked with two solid arrows. The dotted blue arrow is an originally-allowed transition at zero field but that becomes a forbidden transition as the field strength increases. (Top) Strongly asymmetric double-minimum potential in the high field region. Transitions are localized in the deeper well of the potential and the two transitions coincide in energy.

The intensity increase of the ν_2 peak at stronger field indicates that the ammonia molecules became dipole-oriented along the direction of the field. This occurred because the external field was collinear (Z -axis) with the polarization of infrared beam [8], and the molecular electric dipole moment became parallel to the ν_2 transition dipole moment. The evolution of the ro-vibrational spectrum caused by field-induced molecular orientation has been well studied for linear polar molecules in the gas phase [12, 13] and in Ar matrices [14]. These studies showed that, when

the static and radiative fields were collinear, the rotational features in the spectrum gradually disappeared and the vibrational band origin peak ($[v=0, J=0] \rightarrow [v=1, J=0]$) became dominant upon the field-induced molecular orientation [12–14]. Symmetric top rigid rotors show a similar behavior, with slight variation in quantum number dependence [15, 16]. Ammonia has a zero electric dipole moment along the c-axis due to tunneling inversion, but the external field mixes the symmetric and antisymmetric inversion states of ammonia thereby generating a permanent electric dipole moment, which is electrostatically stabilized by becoming oriented parallel to the field.

The increase of ν_2 intensity approached a saturation point at field strength beyond the range displayed in Figure 3-1(a) [17]. This indicated that the degree of field-orientation of molecules asymptotically approached perfect orientation. At the same time, the peak showed a blue-shift that is linearly dependent on the field strength, which manifests the vibrational Stark shift of the ν_2 frequency of spatially oriented molecules [8].

To explain the field-driven spectral changes in the intermediate field region ($< 5 \times 10^7$ V/m), namely the evolution of the $R(0_0^-)$ peak, the appearance of a new peak near 963 cm^{-1} , and the merging of these two peaks, it was examined how an external electrostatic field is expected to modify the inversion–rotation–vibration energy levels of NH_3 . Note that only the rotational states with small ($J < 2$ and $|K| < 2$) quantum numbers are significantly populated at low matrix temperature (10 K). Also, under the influence of electric fields, K remains a good quantum number, indicating that neither electric-dipole-allowed transitions nor field-induced interactions (Stark mixing) occur between states with different K values. Therefore, the field-induced changes can be discussed separately for $K=0$ and $|K|=1$ states.

For $|K|=1$ states, $Q(1_1^+)$ and $Q(1_1^-)$ ($[v=0, J=1, |K|=1, \pm] \rightarrow [v=1, J=1, |K|=1,$

\mp] transitions at zero field are expected to be located at 956 and 980 cm^{-1} , respectively [4]. Transitions within $|K|=1$ states are colored blue in the spectra and energy diagrams in Figure 3-1. In the zero-field spectrum shown in Figure 3-1(a), two blue peaks correspond to $Q(1_1^+)$ and $Q(1_1^-)$ transitions, though they are very weak due to the smaller population in the $J=1$ level than $J=0$. At zero field, the allowed $\nu=0 \rightarrow 1$ transitions between the pairs of inversion doublets in the symmetric potential are “bottom-to-top” and “top-to-bottom”, as required by the dipole selection rule for transitions between opposite parity inversion-rotation-vibration states. The $Q(1_1^+)$, $Q(1_1^-)$ pair of transitions are “top-to-bottom” and “bottom-to-top”, respectively (Figure 3-2(a)).

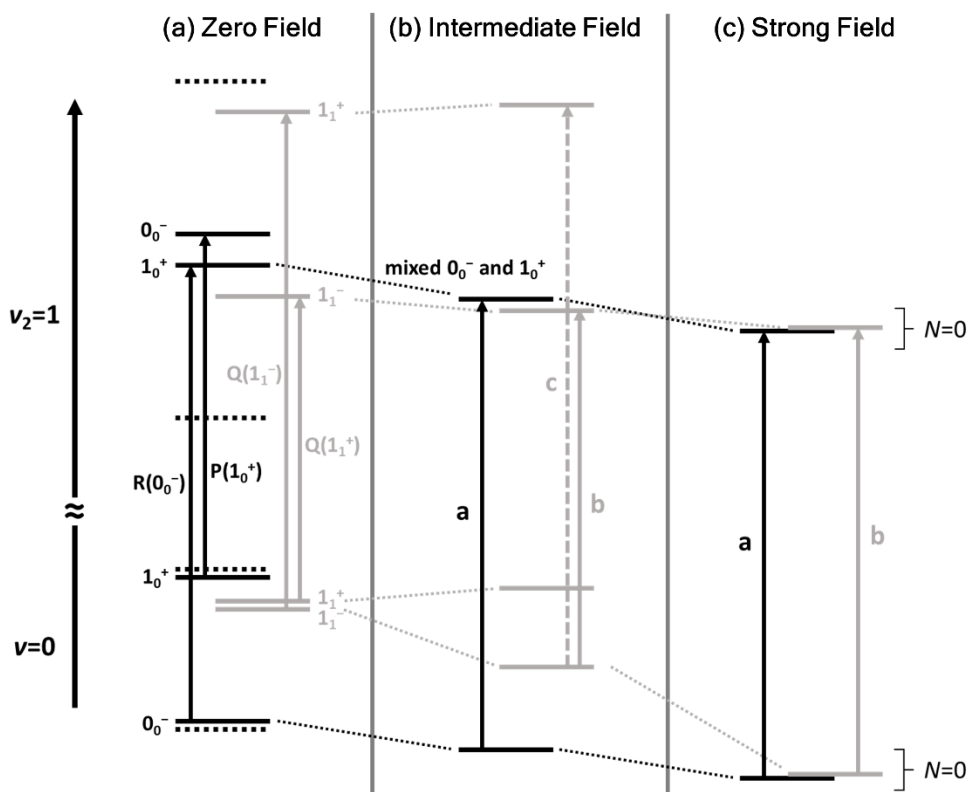


Figure 3-2. Schematic picture of energy levels of NH₃ umbrella inversion–rotation–vibration states and allowed transitions at (a) zero field, (b) intermediate field, and (c) strong field. Those relevant to the spectroscopic observation in this work are displayed. Energy levels marked with black and gray horizontal lines are those of $K=0$ and $|K|=1$, respectively, which are shown horizontally dislocated for visual clarity. Dotted horizontal lines in diagram (a) indicate the energy levels that are absent due to nuclear permutation symmetry. In diagram (c), strong field orientation makes ammonia molecules become a harmonic vibrator bound in the potential well of the electrostatic dipole–field interaction. The quantum number N in diagram (c) indicates the vibrational quanta of the harmonic vibrator, which is defined as $N = 2\tilde{J} - |K + M|$ where \tilde{J} designates the value of the J quantum number of the free-rotor state that adiabatically correlates with the state under external electrostatic fields [15]. The K and M , the projections of the rotational angular momentum J on the c-axis in the molecular frame and Z-axis in the laboratory frame, respectively, remain good quantum numbers under the electrostatic field that is collinear with the radiative field of the IR beam. The correlation diagram between the freely-rotating symmetric top states (without inversion tunneling) and the harmonic vibrator states has been reported [15, 16]. According to the correlation diagram, the 0_0 and 1_1 rotational levels of a symmetric top at zero field evolve into the lowest-lying harmonic vibrator states ($N=0$) at strong field. A similar correlation diagram is expected for ammonia because it behaves like a polar symmetric top at strong field due to the quenching of inversion tunneling and the localization of ν_2 transitions in the lower well of the asymmetric double-minimum potential. Because these correlations between the rotational and librational states exist for both $\nu=0$ and 1, the two ν_2 transitions in $K=0$ and $|K|=1$ observed at intermediate field merge into one peak at strong field. The symbols ‘a’, ‘b’, and ‘c’ correspond to the observed

transitions marked with identical symbols in Figure 3-1(a).

An external field along the direction of the molecular c-axis distorts the double-minimum potential by stabilizing one of wells by the dipole–field interaction energy ($u = -\boldsymbol{\mu} \cdot \mathbf{F}$) and destabilizing the other by the same energy. In the field-asymmetrized potential, wavefunctions become localized in either of two wells via Stark mixing of zero-field eigenstates, and become neither symmetric nor anti-symmetric with respect to the barrier maximum. This wavefunction localization is mathematically illustrated for a 1D double-minimum potential [18]. Significantly, the selection rules change from symmetry-allowed (“bottom-to-top” and “top-to-bottom”) “delocalized” transitions at zero field to “localized” transitions in the field-asymmetrized potential. In the strong field limit, transitions that originate from the localized wavefunctions in each well dominate, which results in the “bottom-to-bottom” and “top-to-top” transition propensity rules. Figure 3-3 illustrates these features.

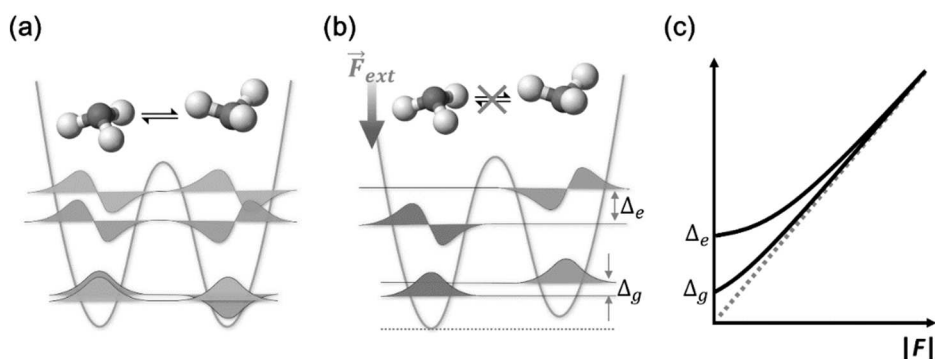


Figure 3-3. (a) A symmetric double-minimum potential at zero field. Energy levels and corresponding wavefunctions of the inversion doublet states in the ground and first excited vibrational levels are shown within the potential. The color of

wavefunctions illustrates the selection rule: transitions are allowed between the same color wavefunctions (“bottom-to-top” and “top-to-bottom”). (b) An asymmetric double-minimum potential in the presence of the external field. The energy splittings of doublets are Δ_g and Δ_e for the ground and excited vibrational levels, respectively. For simplicity, wavefunctions that are fully localized by complete (1:1) Stark mixing are shown, although Δ_g and Δ_e represent intermediate Stark mixing. Notice that the left well wavefunctions do not overlap with the right well wavefunctions. (c) Schematic plot of the energy splittings as a function of external field strength. The dashed line indicates the dipole–field interaction energy ($|u| = |\boldsymbol{\mu} \cdot \mathbf{F}|$).

The effect of an external electric field on a near-degenerate pair of inversion doublet components can be modeled by near-degenerate perturbation theory. The field-perturbed energy of a two-level system is expressed by eq. (3-1) [19, 20].

$$W = \frac{W_1^0 + W_2^0}{2} \pm \left[\left(\frac{W_1^0 - W_2^0}{2} \right)^2 + F^2 \mu_{12}^2 \right]^{1/2} \quad \text{eq. (3-1)}$$

W_1^0 and W_2^0 are the energies of two interacting adjacent levels at zero field, and $F^2 \mu_{12}^2$ is the square of the off-diagonal element of the two-by-two Hamiltonian matrix. F denotes the field strength. The Stark interaction mixes the corresponding eigenstates.

$$\psi_1 = \alpha(F)\psi_1^0 + \beta(F)\psi_2^0 \quad \text{eq. (3-2-1)}$$

$$\psi_2 = -\beta(F)\psi_1^0 + \alpha(F)\psi_2^0 \quad \text{eq. (3-2-2)}$$

The 0 superscript indicates zero-field. The mixing coefficients are expressed as follow, and they become 1:1 in the high field strength limit. The 1:1 linear combination of the two zero-field wavefunctions (complete Stark mixing) results in

the “localized” wavefunctions.

$$\alpha = \left[\frac{\sqrt{\delta^2 + 4F^2\mu_{12}^2} + \delta}{2\sqrt{\delta^2 + 4F^2\mu_{12}^2}} \right]^{1/2} \quad \text{eq. (3-3-1)}$$

$$\beta = \left[\frac{\sqrt{\delta^2 + 4F^2\mu_{12}^2} - \delta}{2\sqrt{\delta^2 + 4F^2\mu_{12}^2}} \right]^{1/2} \quad \text{eq. (3-3-2)}$$

$$\delta = W_1^0 - W_2^0 \quad \text{eq. (3-3-3)}$$

As shown in eq. (3-1), the two interacting levels repel each other in the presence of the Stark field (Figure 3-2(b)).

The peak that emerged at 963 cm^{-1} is the “bottom-to-bottom” transition in $|K|=1$, shown as a blue solid arrow in the middle potential energy surface (PES) diagram in Figure 3-1(b). The 963 cm^{-1} peak blue-shifted as the field strength increased until it merged with the red peak. This is principally attributed to the energy shift of the $|K|=1$ states in $\nu=0$. The energy shift at weak field is larger for the $\nu=0$ state than for the $\nu=1$ state, because the zero-field inversion splitting is much smaller in $\nu=0$ ($< 1 \text{ cm}^{-1}$) than in $\nu=1$ (about 24 cm^{-1}). The “bottom” level of $|K|=1$ in $\nu=0$, originally 1_1^- at zero field, shifts downward, while that in $\nu=1$ shifts very little. This results in the observed blue-shift of the “bottom-to-bottom” transition. The rate of the blue-shift was observed to be 2.6 cm^{-1} per 10^7 V/m (illustrated by Figure 3-4(a)), which agrees with the dipole–field interaction energy ($u = -\boldsymbol{\mu} \cdot \mathbf{F}$) of about 2.4 cm^{-1} at 10^7 V/m . The “bottom-to-top” transition, shown as a blue dashed arrow in the middle PES diagram in Figure 3-1(b), is also expected to be blue-shifted as the 1_1^- level in $\nu=0$ shifts downward at stronger field, but this transition disappears due to the change in transition selection rule mentioned above. The $Q(1_1^-)$ peak around 980 cm^{-1} , though only barely observable in the spectra in Figure 3-1(a), followed this expectation.

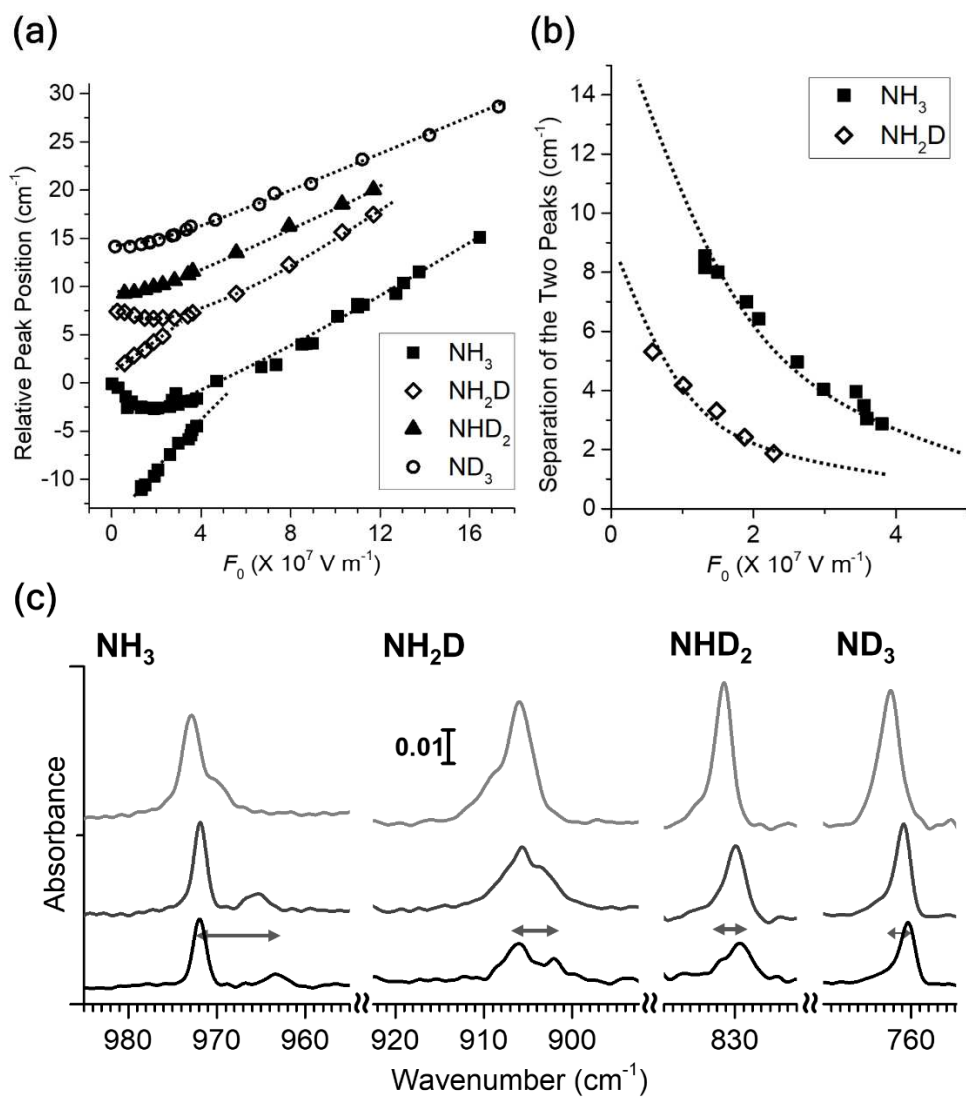


Figure 3-4. (a) Plot of relative peak positions of umbrella vibrational mode of ammonia isotopologues as a function of external field strength. The term ‘relative peak position’ in the plot is used to visually present the frequency separations of two coalescing peaks and the linear shift in the strong field regime for each isotopologue. The absolute values in the ordinate and the vertical spacing between the data points

of different isotopologues have no physical meaning. The dashed lines show the trend. The linear field-dependence of the frequency in the strong field regime is the result of the vibrational Stark effect of field-oriented molecules. (b) Plot of the frequency separation between the pair of coalescing peaks as a function of external field strength for NH_3 and NH_2D . (c) Stark spectra of the umbrella vibrational mode of matrix-isolated ammonia isotopologues. The (bottom, middle, top) spectra were recorded under external fields at strengths of (1.3, 2.1, 3.6), (1.0, 1.9, 3.4), (1.0, 1.9, 3.4), and $(1.3, 2.1, 3.5) \times 10^7$ V/m for NH_3 , NH_2D , NHD_2 , and ND_3 , respectively. The peak separations are marked by the double-headed arrows.

For $K=0$ states, when the field is absent, the $\text{R}(0_0^-)$ transition at 975 cm^{-1} is prominent, with a barely noticeable $\text{P}(1_0^+)$ transition ($[\nu=0, J=1, K=0, +] \rightarrow [\nu=1, J=0, K=0, -]$) at 961.5 cm^{-1} . The $\text{R}(0_0^-)$ transition exhibited the following field-dependent behavior: (1) red-shift (peak position 975 cm^{-1} at zero field $\rightarrow 972\text{ cm}^{-1}$ at 1.3×10^7 V/m); (2) gradual monotonic increase of intensity; (3) narrowing width (the 2.5 cm^{-1} full width at half maximum at zero field decreased to 1 cm^{-1} at 1.3×10^7 V/m). The gradual increase of intensity and the narrowing of band width imply that this formerly ro-vibrational transition changed into a vibrational band origin transition for a field-oriented molecule [12, 14]. This may be possible through Stark mixing of the 0_0^- and 1_0^+ states in $\nu=1$, which are located close to each other (0_0^- being about 4 cm^{-1} higher in energy than 1_0^+) in contrast to their large separation in $\nu=0$. Note that the 0_0^- and 1_0^+ states have proper symmetries for Stark-mixing. The lower-lying 1_0^+ state in $\nu=1$ shifts downward as the field increases, even faster than 0_0^- state in $\nu=0$, resulting in the red-shift observed in the Stark spectra. The mixing of wavefunctions gives some 0_0^- character to the 1_0^+ state, making this transition behave more like a vibrational band origin at a stronger field.

The $K=0$ and $|K|=1$ transitions evolved in frequency in the field range of 1.3×10^7 V/m – 3.8×10^7 V/m to eventually merge into one peak. In the strong field extreme, the molecular c-axis is nearly parallel to the field direction and the potential is highly asymmetric. This makes both transitions localized in the lower well of the asymmetric double-minimum potential. Also, the highly oriented ammonia molecule liberates in the harmonic potential well of electrostatic dipole–field interaction. The 0_0 and 1_1 rotational states of ammonia at zero field are correlated with the lowest-lying states of harmonic librator, which are degenerate in energy (Figure 3-2(c)) [15, 16]. Therefore, only one ν_2 peak must appear for strongly oriented molecules.

Similar experiments of deuterated ammonia molecules (NH_2D , NHD_2 , and ND_3) were conducted to make qualitative observations of isotope effect on the field-driven spectral changes. It is expected [4] that deuterium substitution would reduce the inversion tunneling rate and the magnitude of the inversion splitting. Figure 3-4(c) shows the Stark spectra of ammonia isotopologues in the field region of 1×10^7 V/m – 4×10^7 V/m. The coalescent behavior of two peaks was well resolved in the spectra of NH_3 and NH_2D , whereas the evolution of the peaks could only be deduced from changes of the band shape and width for NHD_2 and ND_3 because the peak separation was narrower than the inherent bandwidth. NH_2D showed a smaller energy separation and lower-field coalescence of the peaks compared to NH_3 (Figure 3-4(a) and 3-4(b)). In the case of ND_3 , “top-to-bottom” and “bottom-to-top” transitions in $|K|=1$, which are $Q(1_1^+)$ and $Q(1_1^-)$, appeared predominantly at zero field at 760 and 762 cm^{-1} , respectively [4]. As the field increases, these transitions become forbidden and the intensity of the “bottom-to-bottom” transition increases. The situation is equivalent to the case of $|K|=1$ states in NH_3 ; however, the energy splitting of the inversion doublets at zero field is much smaller for ND_3 so that the signature of spectral evolution induced by electrostatic fields was not clearly

resolved. The energy levels and transition selection rules that govern the Stark response would be different for NH_2D and NHD_2 since they are asymmetric top rotors, unlike NH_3 and ND_3 . Detailed analysis will not be discussed in this work. Nevertheless, the isotopologue dependence of the energy separation between transitions, which is marked by horizontal double-headed arrows in Figure 3-4(c), follows well the decreasing trend of inversion splitting with increased deuteration (24, 12, 6, and 2 cm^{-1} for NH_3 , NH_2D , NHD_2 , and ND_3) [4]. These isotope effects confirm the field-induced asymmetrization of the PES and the corresponding modification of inversion states.

3.4. Conclusion

In summary, a very strong DC electric field can reversibly orient ammonia molecules in an Ar matrix along the laboratory frame electric field direction. Infrared Stark spectroscopy of spatially oriented ammonia molecules reveals how the external field modifies the PES for the ν_2 umbrella vibration and produces a sequence of changes in the ν_2 mode transition frequencies and intensities. A noteworthy feature is that Stark-effect vibrational spectroscopy reveals detailed information about the large-amplitude inter- and intra-molecular dynamics encoded in static spectra recorded at systematically scanned field strengths. The emergence of vibrational band origin transitions in both $K=0$ and $|K|=1$ states and the evolution of these transitions as the field increases from $1.3 \times 10^7\text{ V/m}$ to $3.8 \times 10^7\text{ V/m}$ reveal progressive localization of the wavefunctions as the double-minimum potential becomes increasingly asymmetrized. This corresponds to a change of the inversion dynamics from efficient resonant tunneling to inefficient quenched tunneling. The merging of two transitions

and a linear blue-shift of the coalesced peak at field strength above 4.7×10^7 V/m indicate strong field-orientation of no-longer fluxional ammonia molecules that librate within the deeper minimum of the asymmetric dipole–field interaction potential. This work demonstrates that, with the help of a strong DC field, frequency domain spectroscopy can give information about the changes of molecular eigenstate energies and wavefunctions that develop due to the field-induced change of the PES. This class of DC spectroscopy gives important insights into dynamics. The accuracy and multi-feature nature of these frequency domain spectra offer advantages over time-resolved ultrafast measurements, which monitor the evolution of multiple wavepackets induced by ultrashort laser pulses interacting with non-oriented molecules.

References

1. Weeks, W. T.; Hecht, K. T.; Dennison, D. M. Inversion-Vibration and Inversion-Rotation Interactions in the Ammonia Molecule. *J. Mol. Spectrosc.* **1962**, *8*, 30–57.
2. Behrens, M.; Buck, U.; Fröchtenicht, R.; Hartmann, M.; Huisken, F.; Rohmund, F. Rotationally Resolved IR Spectroscopy of Ammonia Trapped in Cold Helium Clusters. *J. Chem. Phys.* **1998**, *109*, 5914–5920.
3. Slipchenko, M. N.; Vilesov, A. F. Spectra of NH₃ in He Droplets in the 3 μm Range. *Chem. Phys. Lett.* **2005**, *412*, 176–183.
4. Abouaf-Marguin, L.; Jacox, M. E.; Milligan, D. E. The Rotation and Inversion of Normal and Deuterated Ammonia in Inert Matrices. *J. Mol. Spectrosc.* **1977**, *67*, 34–61.
5. Jacox, M. E.; Thompson, W. E. The Infrared Spectrum of NH₃-d_n Trapped in Solid Neon. *J. Mol. Spectrosc.* **2004**, *228*, 414–431.
6. Ruzi, M.; Anderson, D. T. Matrix Isolation Spectroscopy and Nuclear Spin Conversion of NH₃ and ND₃ in Solid Parahydrogen. *J. Phys. Chem. A* **2013**, *117*, 9712–9724.
7. Hollas, J. M. *High Resolution Spectroscopy*; Butterworths: London, 1982.
8. Park, Y.; Kang, H.; Kang, H. Brute Force Orientation of Matrix-Isolated Molecules: Reversible Reorientation of Formaldehyde in an Argon Matrix toward Perfect Alignment. *Angew. Chem. Int. Ed.* **2017**, *56*, 1046–1049.
9. Kang, H.; Shin, S.; Park, Y.; Kang, H. Electric Field Effect on Condensed-Phase Molecular Systems. III. The Origin of the Field-Induced Change in the Vibrational Frequency of Adsorbed CO on Pt (111). *J. Phys. Chem. C*

- 2016, *120*, 17579–17587.
10. Shin, S.; Kim, Y.; Moon, E.-s.; Lee, D. H.; Kang, H.; Kang, H. Generation of Strong Electric Fields in an Ice Film Capacitor. *J. Chem. Phys.* **2013**, *139*, 074201.
 11. Süzer, S.; Andrews, L. FTIR Spectra of Ammonia Clusters in Noble Gas Matrices. *J. Chem. Phys.* **1987**, *87*, 5131–5140.
 12. Rost, J. M.; Griffin, J. C.; Friedrich, B.; Herschbach, D. R. Pendular States and Spectra of Oriented Linear Molecules. *Phys. Rev. Lett.* **1992**, *68*, 1299–1302.
 13. Choi, M. Y.; Douberly, G. E.; Falconer, T. M.; Lewis, W. K.; Lindsay, C. M.; Merritt, J. M.; Stiles, P. L.; Miller, R. E. Infrared Spectroscopy of Helium Nanodroplets: Novel Methods for Physics and Chemistry. *Int. Rev. Phys. Chem.* **2006**, *25*, 15–75.
 14. Kang, H.; Park, Y.; Kim, Z. H.; Kang, H. Electric Field Effect on Condensed-Phase Molecular Systems. VI. Field-Driven Orientation of Hydrogen Chloride in an Argon Matrix. *J. Phys. Chem. A* **2018**, *122*, 2871–2876.
 15. Härtelt, M.; Friedrich, B. Directional States of Symmetric-Top Molecules Produced by Combined Static and Radiative Electric Fields. *J. Chem. Phys.* **2008**, *128*, 224313.
 16. Maergoiz, A.; Troe, J. Weak- and Strong-Field Stark Energy Levels of Symmetric Top Dipolar Molecules. *J. Chem. Phys.* **1993**, *99*, 3218–3223.
 17. Park, Y.; Kang, H.; Field, R. W.; Kang, H. The Frequency-Domain IR Spectrum of Ammonia Encodes Changes in Molecular Dynamics Caused by a DC Electric Field. *Proc. Natl. Acad. Sci. U.S.A.* **2019**, *116*, 23444–23447.

18. Burrows, B.; Cohen, M.; Feldmann, T. Localization Effects in a Double-Well Model. *Can. J. Phys.* **1998**, *76*, 129–142.
19. Wollrab, J. E. *Rotational Spectra and Molecular Structure*; Academic Press: New York, 1967.
20. Townes, C. H.; Schawlow, A. L. *Microwave Spectroscopy*; McGraw-Hill: New York, 1955.

Chapter 4

Experimental Measurement of Vibrational Stark Sensitivity of Small Molecular Clusters: Clustering Effect on Stark Response of Vibrations

Abstract

The vibrational Stark sensitivity of the hydroxyl stretching and the umbrella vibrations in small hydrogen-bonded water and ammonia clusters, respectively, was measured. The clusters were isolated in the solid Ar matrix. The IR spectral changes under the influence of strong electrostatic fields (10^7 – 10^8 V/m order) were model-fit to extract the magnitude of Stark sensitivity of the vibrations. The magnitude of Stark sensitivity for the clusters was compared to that for corresponding uncomplexed monomers. The clustering effect on the Stark sensitivity is discussed in the perspective of anharmonicity, geometric effect, and intermolecular vibrational coupling. The field-induced spectral changes of a crystalline ice was qualitatively interrogated as an extreme example of clustering through hydrogen-bonding.

4.1. Introduction

A vibration of a molecule is highly sensitive to its environment, which offers a fundamental for vibrational spectroscopy to be used as an informative tool for structural and dynamic studies on molecular systems [1]. Intermolecular interactions substantially influence the nature of vibrations, including the vibrational frequency, line-shape, IR intensity, etc. Based on the fact that most of intermolecular interactions are electrostatic [2, 3], researchers explored the change in vibrational properties, especially the shift of vibrational frequency, by external electrostatic fields, termed vibrational Stark effect or vibrational electrochromism [4–10]. The Stark sensitivity of a vibration, or the vibrational Stark tuning rate, was determined by experimentally observing the frequency change under the application of external electric fields [8, 11–16]. Often, the change in vibrational frequency of a molecule upon the clustering or solvation is expressed with the similar electrostatic description: molecular vibration influenced by local electric fields exerted by neighboring molecules. In this description, so-called the vibrational solvatochromism, the Stark sensitivity of a certain vibration determined from the vibrational Stark effect experiments is used to translate the frequency change into the magnitude of electrostatic fields in intermolecular interactions [17–31]. To ensure the validity of such approach, it should be provided that the electrostatic fields created by environmental molecules are uniform and the dipole–field interactions should be dominant compared to other contributions. It fails to electrostatically illustrate strong interactions such as strong hydrogen bonds, as well as the changes of vibrational properties induced by geometric changes upon solvation or intermolecular coupling/de-coupling.

When an oscillator experiences a change of its molecular environment, not

only the vibrational frequency but the vibrational Stark sensitivity can also be influenced. As an example, we have observed a matrix-dependence of the Stark sensitivity for vibrations of formaldehyde and deuterated water (D_2O) molecules isolated/solvated in solid Ar, Kr, and Xe (unpublished data). Note that those matrices are some of the weakest-interacting solvents. If the magnitude change in the vibrational Stark sensitivity of a molecule induced by forming clusters or solvation shells is systematically investigated, additional information on intermolecular interactions that cannot be obtained from the frequency change would be available, such as the changes in anharmonicity of potential surfaces, molecular geometry, and intermolecular vibrational coupling. This may also be applied to the strongly hydrogen-bonded systems where the vibrational solvatochromism fails.

For that, we measured the Stark sensitivity of the OD stretching of D_2O and the umbrella vibration of ammonia (NH_3 , ND_3) in homogeneous and heterogeneous small hydrogen-bonded molecular clusters. The molecular clusters were isolated in the solid Ar matrix. External electrostatic fields were applied across the matrix by using the ice film nanocapacitor method [11, 14]. The magnitudes of Stark sensitivity for the clusters were determined by model-fitting the experimentally spectra recorded under external fields in two different fit methods [8, 12], one of which failed for large field-induced spectral changes. The determined magnitude of vibrational Stark sensitivity for the clusters was compared to that for corresponding uncomplexed molecules to evaluate the clustering effect. Upon the clustering through hydrogen bonds, the magnitudes of Stark sensitivity for the OD stretching vibration showed an extensive enhancement, while those for the umbrella vibration of ammonia decreased. The rationalization of such clustering effect on the vibrational Stark response is proposed, which qualitatively explained the Stark response of the stretching and bending vibrations of D_2O crystalline ice, an extreme

D₂O cluster.

4.2. Experimental Details

The experiments were performed in an ultrahigh vacuum (UHV) chamber, the detailed description of which can be found elsewhere [13, 14]. The molecular films were prepared on a cold Pt(111) substrate (about 10 K) by sequential deposition of the corresponding gaseous species that were introduced into the UHV chamber through variable leak valves. H₂O (Milli-Q) and D₂O (Aldrich, 99 atom % D) were purified by freeze–pump–thaw cycles. Ar, NH₃ and HCl (Sigma-Aldrich, >99%) gases were used directly from commercially available gas cylinders. ND₃ were prepared by thermal evaporation of ND₃ molecules from ND₄OD solution (Alfa Aesar, 99 atom % D, 23.0–27.0 wt % sol), utilizing the large vapor pressure of ammonia relative to that of water [32]. Tube dosers were used to guide NH₃, ND₃, and HCl gases close to the Pt(111) substrate. Other gases were back-filled.

The matrix-isolation of molecular clusters was achieved by co-adsorbing the corresponding molecules with Ar gas in a predetermined pressure ratio. For instance, the matrix-isolated D₂O clusters (including (D₂O)₃ and (D₂O)₄) were prepared by co-deposition of D₂O and Ar gases with pressure ratio of 1:200–1:100. The sample had a stacked structure of an Ar film (144–960 ML thickness; ML = monolayer; 1 ML = 1.1×10^{15} molecules/cm²) that contained molecular clusters to be investigated, which was sandwiched between two spacer layers (48–120 ML each) of pure Ar films. The Ar film was capped with an amorphous water film (25 ML). The appropriate isopologue of water was used to constitute the capping layer to prevent the spectral overlap with the molecular clusters of interest. The thickness of

the complete sample was 150–710 nm.

Electrostatic fields were applied across the film by using the ice film nanocapacitor method, which has been described previously in detail [11]. The field strength was increased by the deposition of Cs⁺ ions on the capping ice film and decreased by spraying low energy (roughly 3 eV) electrons on the Cs⁺-deposited film [33, 34]. The strength of the applied field was estimated from the film voltage measured with a Kelvin probe. Measured values of field strength given in this chapter are the macroscopic field strength (F_0), obtained simply by dividing the film voltage with the thickness of the film. The actual field strength (F) that a matrix-isolated molecular cluster experiences can be expressed as $F = c_{\text{local}}F_0$, with the local field correction factor c_{local} estimated to be in the range of 1–2 [14, 24].

Reflection–absorption infrared spectroscopic (RAIRS) measurements were conducted using a Fourier transform infrared spectrometer with a liquid nitrogen-cooled mercury–cadmium–telluride detector in the grazing angle reflection geometry (85°). An incident IR beam was p-polarized by a wire grid polarizer. The RAIR spectra were averaged 256 times when acquired with 1 cm⁻¹ spectral resolution, and 1024 times with 4 cm⁻¹ resolution. The sloped baselines of all spectra, caused by the increasing negative reflectance–absorbance with increasing wavenumber [35, 36], were corrected.

4.3. Results and Discussion

Figure 4-1 shows the field-induced spectral changes of D₂O clusters isolated in the Ar matrix in the OD stretch region. In the case of the bonded OD stretch, the bands were clearly distinguished for (D₂O)_n clusters of n=2–5. The bonded OD stretch

bands of $(\text{D}_2\text{O})_3$ (2578 cm^{-1}) and $(\text{D}_2\text{O})_4$ (2488 cm^{-1}) are marked with gray highlight in Figure 4-1 [37, 38]. Other vibrational bands, i.e. free OD stretch (roughly $2700\text{--}2800\text{ cm}^{-1}$ in Figure 4-1) [37] and DOD bend ($1170\text{--}1220\text{ cm}^{-1}$; not shown), were not clearly resolved for each cluster due to small frequency separation compared to the spectral resolution. Figure 4-1(a) and 4-1(b) show the spectra at zero field and under field whose strength is $1.9 \times 10^8\text{ V/m}$, respectively. The bonded OD stretch bands of $(\text{D}_2\text{O})_3$ and $(\text{D}_2\text{O})_4$ showed drastic changes under the external field. As can be seen from the difference spectrum in Figure 4-1(c), the spectral change is principally broadening of the band. Considering the cyclic structure of $(\text{D}_2\text{O})_3$ and $(\text{D}_2\text{O})_4$ [38–41], which implies the small net dipole moment [42], and rigidity of the solid Ar matrix at 10 K, the clusters would retain their initial isotropic orientation distribution, not being reoriented by external fields. The band broadening by the external field is a consequence of the vibrational Stark effect on the isotropically-oriented dipoles [7, 8, 24].

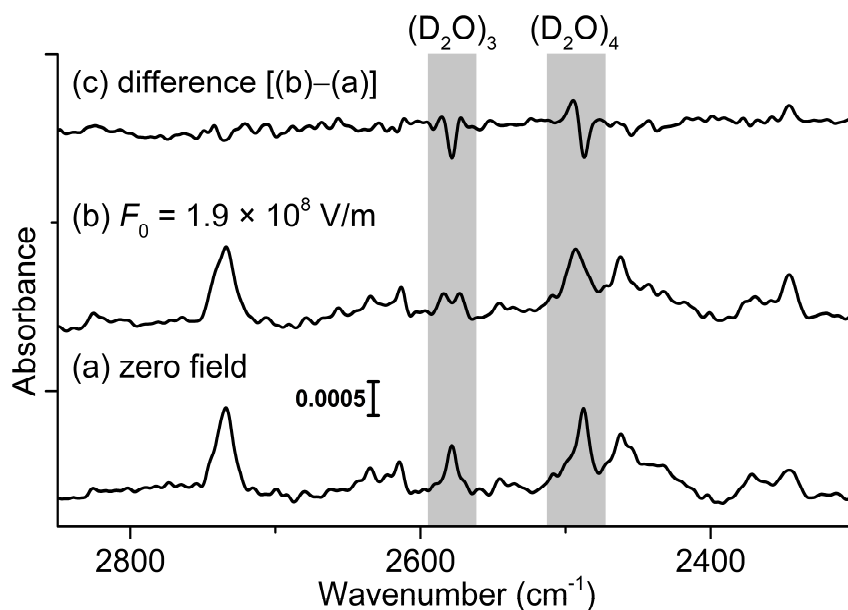


Figure 4-1. RAIR spectra of the Ar film containing D₂O molecules inside, (a) at zero field and (b) under field of 1.9×10^8 V/m. (c) Difference spectrum of (b) and (a). The spectral bands for the bonded OD stretch vibrations of (D₂O)₃ and (D₂O)₄ are highlighted with gray shades. The spectra were acquired with a spectral resolution of 4 cm^{-1} .

The magnitude of Stark sensitivity, $|\Delta\mu|$, of a vibration can be determined by fitting the experimentally observed difference absorbance, as practiced by S. Boxer and coworkers [8]. In this method, the difference absorbance, $\Delta A(\tilde{\nu})$, is fit to a linear combination of frequency-weighted derivatives of zero-field absorbance, $A(\tilde{\nu})$ (see eq. (4-1)).

$$\Delta A(\tilde{\nu}) = \alpha A(\tilde{\nu}) + \beta \tilde{\nu} \frac{\partial A(\tilde{\nu})}{\partial \tilde{\nu}} + \gamma \tilde{\nu}^2 \frac{\partial^2 A(\tilde{\nu})}{\partial \tilde{\nu}^2} \quad (\tilde{\nu}: \text{frequency}) \quad \text{eq. (4-1)}$$

The Stark sensitivity $|\Delta\mu|$ is derived from the coefficient of the second derivative term, γ in eq. (4-1). Figure 4-2 shows the experimentally acquired difference absorbance for the bonded OD stretch mode of (D₂O)₃ at three different field strengths with fit. The sensitivity values determined by the fit are written in red. Note that the field strength used for determining $|\Delta\mu|$ is the experimentally measured macroscopic field strength (F_0) (see Experimental Details section). Since F_0 has a relation with the actual field strength (F) that an isolated cluster experiences in the matrix by $F = c_{\text{local}} F_0$ [14, 24], the strict expression for the sensitivity values determined in Figure 4-2 is the sensitivity multiplied by the local field correction factor, $c_{\text{local}} |\Delta\mu|$. The c_{local} term is omitted in the expression for convenience in the rest of this article. Though the c_{local} term is expected to vary with respect to the clusters, since the local field is dependent on the polarizability of the isolated cluster as well as the shape and size of the cavity where the cluster is located [14, 43], the

difference in c_{local} value between different clusters is expected to be insignificant.

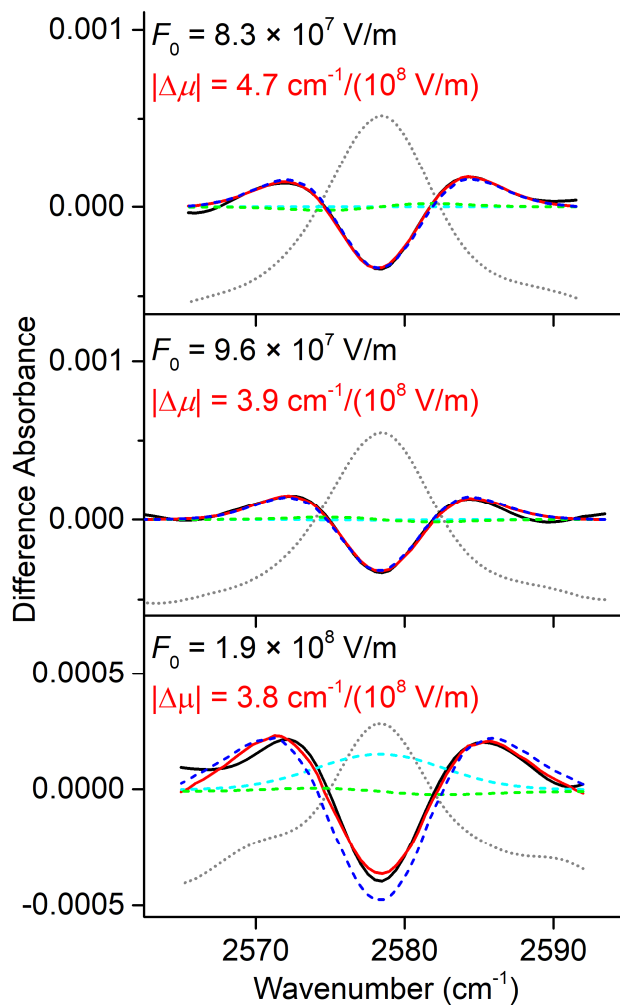


Figure 4-2. Vibrational Stark spectra (difference absorbance; black solid lines) of the bonded OD stretch mode of $(\text{D}_2\text{O})_3$ isolated in the Ar matrix acquired at various field strengths with fit (red solid lines). The zero-field absorbance for each difference spectrum is displayed with gray dotted lines. The contributions on the fit of the zeroth, first, and second derivatives of zero-field absorbance are depicted with cyan, green,

and blue dashed lines, respectively. The experimental spectra were acquired with a spectral resolution of 4 cm^{-1} .

The similar Stark analysis was conducted for the umbrella vibration of $(\text{NH}_3)_3$, the results of which are displayed in Figure 4-3(a). The umbrella vibrational band of the cluster exhibited broadening under external fields. The difference absorbance at $1.3 \times 10^7\text{ V/m}$ (shown in top of Figure 4-3(a)) was well fit with a linear combination of the derivatives of zero-field absorbance. At stronger fields, however, namely at 2.6 and $3.6 \times 10^7\text{ V/m}$ (middle and bottom of Figure 4-3(a)), where the band broadening was substantial so that the separation between red- and blue-shifting components exceeded the breadth of the second derivative of zero-field absorbance, the model failed to reproduce the difference absorbance.

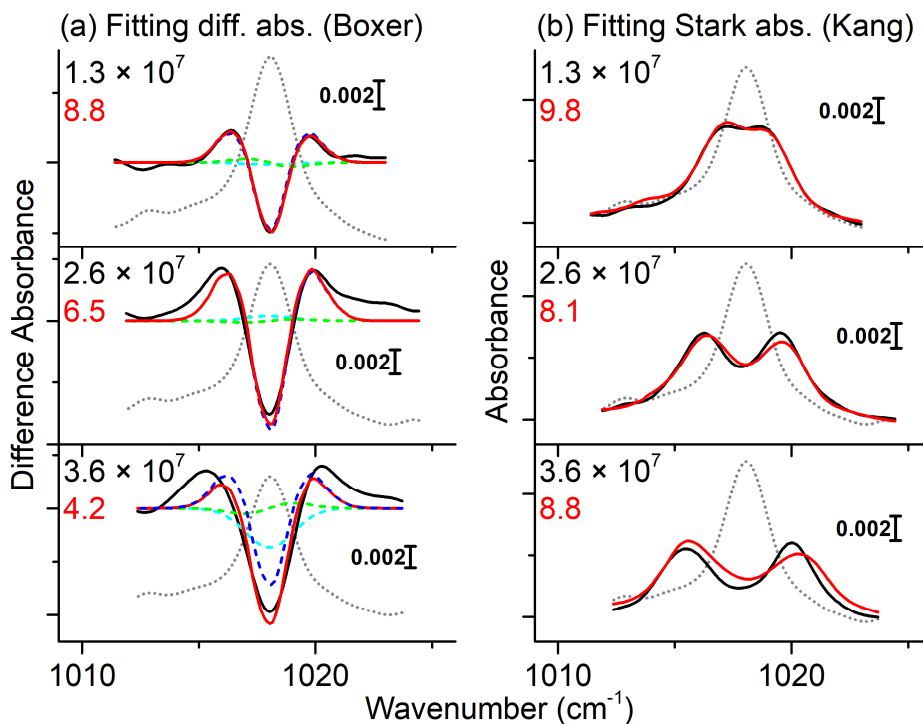


Figure 4-3. Vibrational Stark spectra of the umbrella vibration of the matrix-isolated $(\text{NH}_3)_3$ with (a) difference absorbance fit and (b) Stark absorbance fit. The color-coding of lines in (a) is identical with that in Figure 4-2. In the case of (b), black solid lines, red solid lines, and gray dotted lines correspond to the Stark absorbance, simulated Stark absorbance, and zero-field absorbance, respectively. The field strength at which each Stark spectrum was acquired and the magnitude of vibrational Stark sensitivity ($|\Delta\mu|$) obtained by fitting the spectrum are marked in each plot in units of V/m (black) and $\text{cm}^{-1}/(10^8 \text{ V/m})$ (red), respectively. The experimental spectra were acquired with a spectral resolution of 1 cm^{-1} .

Alternatively, a numerical method to simulate the absorbance under fields (Stark absorbance), rather than difference absorbance, was employed to extract $|\Delta\mu|$ from the experimental observation. In this method, zero-field absorbance was divided into contributions from individual oscillators with an isotropic orientation. The frequency of each absorbance by the individual oscillator was shifted according to the Stark effect relationship approximated to the second-order term, given by

$$\Delta\tilde{\nu} \cong -(\Delta\boldsymbol{\mu} \cdot \mathbf{F} + \frac{1}{2}\mathbf{F} \cdot \Delta\boldsymbol{\alpha} \cdot \mathbf{F}) \quad \text{eq. (4-2)}$$

where $\Delta\tilde{\nu}$ is the frequency shift in cm^{-1} , $\Delta\boldsymbol{\mu}$ is the Stark sensitivity in $\text{cm}^{-1}/(10^8 \text{ V/m})$, \mathbf{F} is the electric field in 10^8 V/m , and $\Delta\boldsymbol{\alpha}$ is the second-order coefficient, previously termed as the difference polarizability [8]. Afterwards, the contributions of shifted absorbance by individual oscillators were summed to result the simulated Stark absorbance, which was fit to the experimentally observed Stark absorbance by varying the magnitude of $\Delta\boldsymbol{\mu}$ and $\Delta\boldsymbol{\alpha}$. The detailed description on the numerical simulation can be found elsewhere [12].

The results of Stark absorbance fit for the $(\text{NH}_3)_3$ umbrella vibration are

shown in Figure 4-3(b). The simulated Stark absorbance spectra well matched with the experimental spectra. The simulation resulted in convergent $|\Delta\mu|$ values for different field strengths. The Stark spectra were experimentally acquired and the Stark sensitivities were determined by simulations as well for the NH_3 umbrella vibration of matrix-isolated $\text{NH}_3\text{-HCl}$ and $\text{NH}_3\text{-H}_2\text{O}$ 1:1 complexes and the ND_3 umbrella vibration of $(\text{ND}_3)_3$. In all cases, the Stark absorbance fit provided more reliable Stark sensitivity than the difference absorbance fit.

The Stark sensitivities, $|\Delta\mu|$, derived by fitting the Stark absorbance for the various matrix-isolated molecular clusters are listed in Table 1. The Stark sensitivities for the symmetric stretch of D_2O monomer and the umbrella vibration of NH_3/ND_3 in the Ar matrices, which were previously determined with the field-oriented D_2O and NH_3/ND_3 molecules [16, 32], as well as other reported values of relevant systems [12, 19, 44–46], are listed together in Table 1 to evaluate the clustering effect on the field-response of the vibrations.

Table 1. Resonant frequency and magnitude of Stark sensitivity of the OD stretching and the ammonia umbrella vibrations for various clusters.

Species	Vibration	Frequency in cm^{-1}	$ \Delta\mu $ in $\text{cm}^{-1}/(10^8 \text{ V/m})$
$(\text{D}_2\text{O})_3$ in Ar	Bonded OD stretch	2578	4.4 ^a
$(\text{D}_2\text{O})_4$ in Ar	Bonded OD stretch	2488	2.6 ^a
D_2O in Ar	Symmetric stretch	2658 (band origin)	0.33 ^b
HDO in liquid H_2O	Bonded OD stretch	-	1.65 ^c
$(\text{D}_2\text{O})_n$; n=2–6	Bonded OD stretch	-	1.76 ^d

HDO in solid H ₂ O (I _h)	Bonded OD stretch	~2420	6.4 – 12 ^e
(HDO)(H ₂ O) ₇	Bonded OD stretch	-	4.8 ^e
(HDO)(H ₂ O) ₃	Bonded OD stretch	-	~2.5 ^f
(HDO)(H ₂ O) ₃	Free OD stretch	-	~0.3 ^f
HDO	OD stretch	-	0.13 – 0.25 ^f
2,6-di- <i>t</i> -butylphenol in toluene	OD stretch in weak OD•••π bond	~2674	1.4 ^g
(NH ₃) ₃ in Ar	Umbrella	1018	8.9 ^a
NH ₃ –HCl in Ar	Umbrella of NH ₃	1070	16.3 ^a
NH ₃ –H ₂ O in Ar	Umbrella of NH ₃	1035	13.3 ^a
NH ₃ in Ar	Umbrella	968 (band origin)	14.2 ^h
(ND ₃) ₃ in Ar	Umbrella	792	5.7 ^a
ND ₃ in Ar	Umbrella	761 (band origin)	9.3 ^h

^aThis work

^bReference 16

^cReference 44

^dReference 45

^eReference 12

^fReference 46

^gReference 19

^hReference 32

The $|\Delta\mu|$ values of the bonded OD stretch for (D₂O)₃ and (D₂O)₄ in the Ar matrix, 4.4 and 2.6 cm⁻¹/(10⁸ V/m), respectively, are about one order of magnitude

larger than that of the symmetric stretch of matrix-isolated D₂O monomer, 0.33 cm⁻¹/(10⁸ V/m) [16]. Such substantial difference in Stark sensitivity between the bonded OD stretch of clusters and the symmetric stretch of monomer, however, must not originate from the distinction between the local and coupled vibrations, but arise predominantly from the hydrogen-bonding. A similarly significant difference between cluster and monomer was reported by a quantum calculation: the Stark sensitivity of the bonded OD vibration of (HDO)(H₂O)₃ (2.5 cm⁻¹/(10⁸ V/m)) was order of magnitude larger than the OD vibration of HDO (0.13–0.25 cm⁻¹/(10⁸ V/m)) (see Table 1) [46]. Besides, in the same theoretical work, $|\Delta\mu|$ of the free (non-bonded) OD stretch of (HDO)(H₂O)₃ was reported to be about 0.3 cm⁻¹/(10⁸ V/m), similar to that of HDO monomer [46]. Stark sensitivities of the bonded OD stretch of other water clusters were calculated/observed to be much larger than those of non-bonded OD stretch, as listed in Table 1. This suggests that the hydrogen-bonding is responsible for the enlarged Stark sensitivity of stretching vibration. The potential energy surface for the OD stretch becomes significantly more asymmetric and anharmonic when it is hydrogen-bonded, thereby the potential curve becomes more vulnerable to vary under the influence of electric fields (Figure 4-4(a)) [10, 12]. This is expected to make the vibrational frequency more susceptible to external electric fields.

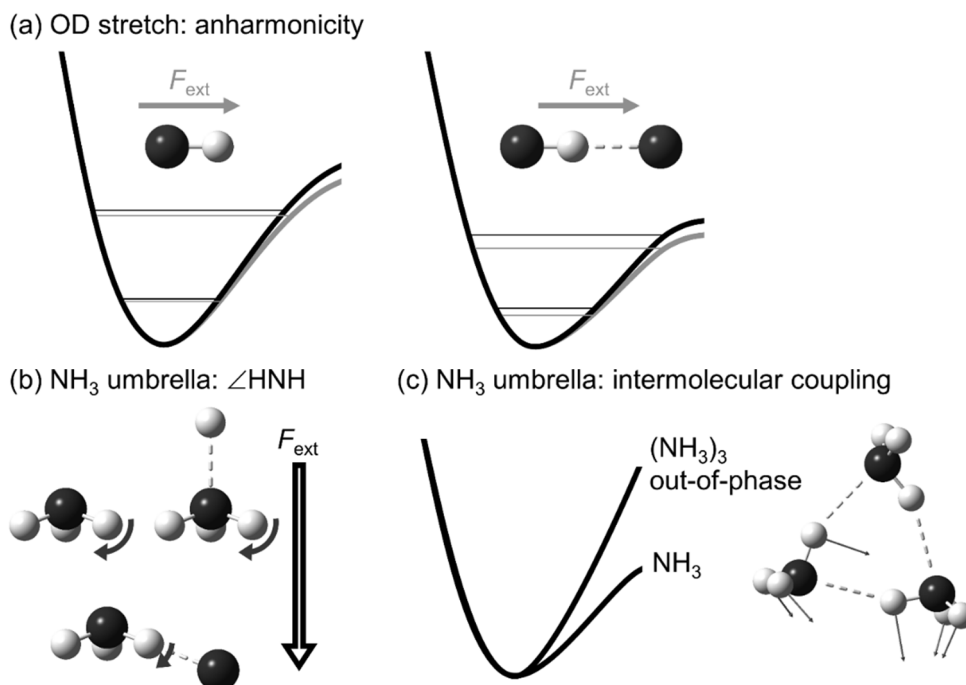


Figure 4-4. Simplified schematic of clustering effect on Stark sensitivity of vibrations. (a) Increase of anharmonic character of the OD stretching by hydrogen-bonding. (b) Suppression of field-driven HNH angle change in NH_3 when hydrogen-bonded. (c) Symmetrized potential energy surface of out-of-phase coupling of the NH_3 umbrella vibration.

On the contrary, in the case of the umbrella vibration of ammonia molecules, the Stark sensitivity for the hydrogen-bonded clusters, namely $(\text{NH}_3)_3$ and $(\text{ND}_3)_3$, was observed to be smaller than that of the uncomplexed molecules. The $|\Delta\mu|$ values for the umbrella vibration of $(\text{NH}_3)_3$ and $(\text{ND}_3)_3$, 8.9 and 5.7 $\text{cm}^{-1}/(10^8 \text{ V/m})$, respectively, were about two-thirds of those of the corresponding uncomplexed monomers, 14.2 $\text{cm}^{-1}/(10^8 \text{ V/m})$ for NH_3 and 9.3 $\text{cm}^{-1}/(10^8 \text{ V/m})$ for ND_3 [32]. For

NH₃-HCl (16.3 cm⁻¹/(10⁸ V/m)) and NH₃-H₂O (13.3 cm⁻¹/(10⁸ V/m)) 1:1 complexes, the umbrella vibration of NH₃ showed similar $|\Delta\mu|$ with the uncomplexed NH₃. These altogether imply that the umbrella vibration of an ammonia molecule becomes less susceptible to electric fields when it forms homogeneous hydrogen-bonded clusters.

Two factors are thought to be involved in such clustering effect on Stark sensitivity of the umbrella vibration. One is the geometric effect on the Stark sensitivity [16, 46]. A geometric change under external fields, HNH angle (\angle HNH) of NH₃ in this case, can explain the field-induced frequency shift of the NH₃ umbrella motion. A NH₃ structure with smaller \angle HNH would have a larger dipole and can be better stabilized by an external field parallel to the dipole. The parallel field, therefore, is expected to decrease the \angle HNH of NH₃ by means of the dipole-field interaction. The decreased \angle HNH results in a blue-shift of the NH₃ umbrella vibration. An anti-parallel field would derive the opposite changes. The NH₃ umbrella vibration frequency is sensitively shifted even with a negligibly small field-driven \angle HNH change, which is estimated to be <0.1% with respect to the equilibrium \angle HNH (107°) under <10⁸ V/m external fields, as inferred from the large Stark sensitivity of 14.2 cm⁻¹/(10⁸ V/m). When it forms a hydrogen bond, the geometric change in the \angle HNH under the influence of external fields would be suppressed (Figure 4-4(b)), which results in the decrease in Stark sensitivity. The hydrogen-bond-accepting NH₃ which is expected not to experience such restriction in field-induced \angle HNH change would not have the decreased Stark sensitivity compared to the monomer's, as observed for NH₃-HCl and NH₃-H₂O.

The other is intermolecular vibrational coupling. The umbrella vibration of ammonia which is involved in a homogeneous cluster is expected to be coupled to

umbrella vibrations of other ammonia constituting the cluster. For instance, in the case of ammonia trimer, the intermolecular coupling between umbrella vibrations through hydrogen bonds would result in two near-degenerate out-of-phase and one in-phase umbrella vibrations. The in-phase vibration is totally symmetric with respect to the three-fold axis of the cluster, which means that the vibration has an almost zero transition dipole moment. Therefore, the umbrella vibrational band of ammonia trimer we observed in spectra should originate from the out-of-phase motion. The potential surface along the out-of-phase vibration coordinate, where $\angle\text{HNH}$ decrease in one NH_3 and $\angle\text{HNH}$ increase in the other NH_3 constituting $(\text{NH}_3)_3$ clusters occur synchronously, is expected to have more centrosymmetric shape compared to that along the umbrella vibration coordinate of the uncomplexed ammonia which is highly asymmetric and anharmonic as inferred from the large Stark sensitivity (Figure 4-4(c)). The symmetrized potential curve for the out-of-phase umbrella vibration of ammonia trimer may account for the decrease in Stark sensitivity of the vibrational band.

As an extreme of clustering through hydrogen-bonding, we report the field-driven spectral changes of D_2O crystalline ice (Figure 4-5(a)). An external field induced a dramatic change in the stretching region and an imperceptible change for the bending vibration of D_2O ice. This contrasts sharply with the Stark sensitivity of matrix-isolated D_2O monomer where the bending vibration was observed to be about six times more sensitive to external fields than the stretching vibration, as depicted in Figure 4-5(b) [16]. As shown for small water clusters, the network of hydrogen bond seems to be responsible for the extensive enhancement of the Stark sensitivity of the OD stretching in ice. In the case of bending vibration, which can be thought analogously to the umbrella vibration of ammonia, the rigidity of $\angle\text{DOD}$ in ice and

intermolecular coupling through hydrogen bonds seem to result the decrease in the Stark sensitivity. Note that, in Figure 4-5(a) and 4-5(b), the relative IR intensity between the stretching and bending modes is markedly reversed when D₂O forms a large hydrogen-bonded system. The bending vibration has about an order of magnitude larger intensity than the stretching mode for D₂O monomer [16, 47], while for D₂O crystalline ice it is about one order of magnitude weaker than the stretching. This implies the substantial decrease in dipole derivative along the bending coordinate ($\angle DOD$), for D₂O ice compared to D₂O monomer. The decreased dipole derivative anticipates the restricted external-field-induced geometric change along the bending coordinate, which coincides with the proposed rationalization on the reduced field-driven spectral changes in the bending vibration of ice.

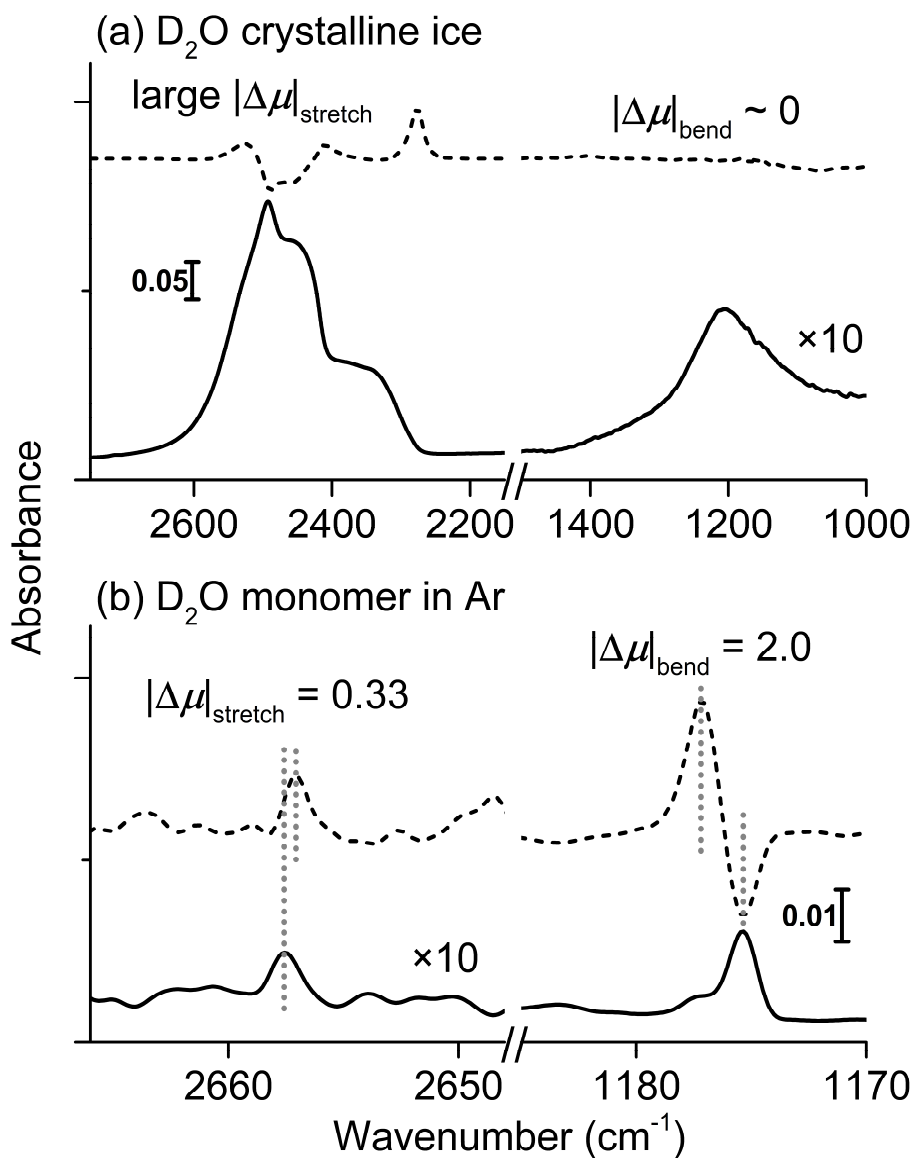


Figure 4-5. (a) Stark spectra of D₂O crystalline ice in the stretching region (2300–2700 cm⁻¹) and the bending region (1000–1400 cm⁻¹). The film structure was Cs⁺/H₂O(amorphous; 14 nm)/Ar(70 nm)/D₂O(crystalline; 46 nm)/Pt. The D₂O crystalline ice was prepared by adsorption of D₂O molecules at 140 K followed by 150 K annealing for a short period (~100 seconds). Solid line is an absorbance

spectrum at zero field. Dashed line is a difference absorbance between the spectra under 1.4×10^8 V/m and at zero field. Spectral resolution: 4 cm^{-1} . (b) Stark spectra of the symmetric stretching (2657.7 cm^{-1}) and the bending (1174.6 cm^{-1}) vibrational bands of field-oriented D_2O monomer isolated in the Ar matrix. Solid line spectrum was acquired at 3.3×10^7 V/m. Dashed line is a difference spectrum between the spectra under 1.2×10^8 V/m and 3.3×10^7 V/m. The magnitude of Stark sensitivity is shown in the unit of $\text{cm}^{-1}/(10^8 \text{ V/m})$. Gray dotted vertical lines visually guide the degree of field-induced peak position shift. Spectral resolution: 1 cm^{-1} .

4.4. Conclusion

The Stark sensitivity of the OD stretching and the umbrella vibrations of matrix-isolated D_2O and NH_3/ND_3 clusters, respectively, was spectroscopically measured. The $|\Delta\mu|$ of the bonded OD stretching of $(\text{D}_2\text{O})_3$ and $(\text{D}_2\text{O})_4$ was about one order of magnitude larger than that of D_2O monomer, which can be rationalized by increased anharmonic character of the vibration as a result of hydrogen bond. For the umbrella vibration of ammonia, $|\Delta\mu|$ decreased for hydrogen-bonded trimer to two-thirds of that for monomer. We proposed two plausible candidates to account for the phenomena: geometric effect and intermolecular vibrational coupling. The Stark spectra of D_2O crystalline ice showed the substantial field-driven changes in the stretching region and imperceptible change in the bending mode. The comparison of the field-response of this extreme D_2O cluster with that of D_2O monomer supports the proposed explanation of the clustering effect on the Stark sensitivity. This study reveals a possibility that Stark sensitivity serves as a probe for interrogating the intermolecular interactions including the strong hydrogen bond.

References

1. Kim, H.; Cho, M. Infrared Probes for Studying the Structure and Dynamics of Biomolecules. *Chem. Rev.* **2013**, *113*, 5817–5847.
2. Havenith, M. H. *Infrared Spectroscopy of Molecular Clusters: An Introduction to Intermolecular Forces*; Springer-Verlag: Berlin, 2002.
3. Stone, A. *The Theory of Intermolecular Forces*; Oxford University Press: Oxford, 2013.
4. Hush, N. S.; Reimers, J. R. Vibrational Stark Spectroscopy. 1. Basic Theory and Application to the CO Stretch. *J. Phys. Chem.* **1995**, *99*, 15798–15805.
5. Reimers, J.; Zeng, J.; Hush, N. Vibrational Stark Spectroscopy. 2. Application to the CN Stretch in HCN and Acetonitrile. *J. Phys. Chem.* **1996**, *100*, 1498–1504.
6. Reimers, J. R.; Hush, N. S. Vibrational Stark Spectroscopy 3. Accurate Benchmark ab initio and Density Functional Calculations for CO and CN. *J. Phys. Chem. A* **1999**, *103*, 10580–10587.
7. Bublitz, G. U.; Boxer, S. G. Stark Spectroscopy: Applications in Chemistry, Biology, and Materials Science. *Annu. Rev. Phys. Chem.* **1997**, *48*, 213–242.
8. Andrews, S. S.; Boxer, S. G. Vibrational Stark Effects of Nitriles I. Methods and Experimental Results. *J. Phys. Chem. A* **2000**, *104*, 11853–11863.
9. Andrews, S. S.; Boxer, S. G. Vibrational Stark Effects of Nitriles II. Physical Origins of Stark Effects from Experiment and Perturbation Models. *J. Phys. Chem. A* **2002**, *106*, 469–477.
10. Park, E. S.; Boxer, S. G. Origins of the Sensitivity of Molecular Vibrations to Electric Fields: Carbonyl and Nitrosyl Stretches in Model Compounds

- and Proteins. *J. Phys. Chem. B* **2002**, *106*, 5800–5806.
11. Shin, S.; Kim, Y.; Moon, E.-s.; Lee, D. H.; Kang, H.; Kang, H. Generation of Strong Electric Fields in an Ice Film Capacitor. *J. Chem. Phys.* **2013**, *139*, 074201.
 12. Shin, S.; Kang, H.; Cho, D.; Lee, J. Y.; Kang, H. Effect of Electric Field on Condensed-Phase Molecular Systems. II. Stark Effect on the Hydroxyl Stretch Vibration of Ice. *J. Phys. Chem. C* **2015**, *119*, 15596–15603.
 13. Kang, H.; Shin, S.; Park, Y.; Kang, H. Electric Field Effect on Condensed-Phase Molecular Systems. III. The Origin of the Field-Induced Change in the Vibrational Frequency of Adsorbed CO on Pt (111). *J. Phys. Chem. C* **2016**, *120*, 17579–17587.
 14. Park, Y.; Kang, H.; Kang, H. Brute Force Orientation of Matrix-Isolated Molecules: Reversible Reorientation of Formaldehyde in an Argon Matrix toward Perfect Alignment. *Angew. Chem. Int. Ed.* **2017**, *56*, 1046–1049.
 15. Kang, H.; Park, Y.; Kim, Z. H.; Kang, H. Electric Field Effect on Condensed-Phase Molecular Systems. VI. Field-Driven Orientation of Hydrogen Chloride in an Argon Matrix. *J. Phys. Chem. A* **2018**, *122*, 2871–2876.
 16. Park, Y.; Lim, J. H.; Lee, J. Y.; Kang, H. Electric Field Effect on Condensed-Phase Molecular Systems. VII. Vibrational Stark Sensitivity of Spatially Oriented Water Molecules in an Argon Matrix. *J. Phys. Chem. C* **2019**, *123*, 9868–9874.
 17. Suydam, I. T.; Snow, C. D.; Pande, V. S.; Boxer, S. G. Electric Fields at the Active Site of an Enzyme: Direct Comparison of Experiment with Theory. *Science* **2006**, *313*, 200–204.
 18. Fafarman, A. T.; Sigala, P. A.; Herschlag, D.; Boxer, S. G. Decomposition

- of Vibrational Shifts of Nitriles into Electrostatic and Hydrogen-Bonding Effects. *J. Am. Chem. Soc.* **2010**, *132*, 12811–12813.
19. Saggiu, M.; Levinson, N. M.; Boxer, S. G. Direct Measurements of Electric Fields in Weak OH $\cdots\pi$ Hydrogen Bonds. *J. Am. Chem. Soc.* **2011**, *133*, 17414–17419.
 20. Saggiu, M.; Levinson, N. M.; Boxer, S. G. Experimental Quantification of Electrostatics in X–H $\cdots\pi$ Hydrogen Bonds. *J. Am. Chem. Soc.* **2012**, *134*, 18986–18997.
 21. Fried, S. D.; Bagchi, S.; Boxer, S. G. Measuring Electrostatic Fields in Both Hydrogen-Bonding and Non-Hydrogen-Bonding Environments Using Carbonyl Vibrational Probes. *J. Am. Chem. Soc.* **2013**, *135*, 11181–11192.
 22. Fried, S. D.; Wang, L.-P.; Boxer, S. G.; Ren, P.; Pande, V. S. Calculations of the Electric Fields in Liquid Solutions. *J. Phys. Chem. B* **2013**, *117*, 16236–16248.
 23. Fried, S. D.; Bagchi, S.; Boxer, S. G. Extreme Electric Fields Power Catalysis in the Active Site of Ketosteroid Isomerase. *Science* **2014**, *346*, 1510–1514.
 24. Fried, S. D.; Boxer, S. G. Measuring Electric Fields and Noncovalent Interactions Using the Vibrational Stark Effect. *Acc. Chem. Res.* **2015**, *48*, 998–1006.
 25. Oklejas, V.; Sjoström, C.; Harris, J. M. SERS Detection of the Vibrational Stark Effect from Nitrile-Terminated SAMs to Probe Electric Fields in the Diffuse Double-Layer. *J. Am. Chem. Soc.* **2002**, *124*, 2408–2409.
 26. Oklejas, V.; Sjoström, C.; Harris, J. M. Surface-Enhanced Raman Scattering Based Vibrational Stark Effect as a Spatial Probe of Interfacial Electric Fields in the Diffuse Double Layer. *J. Phys. Chem. B* **2003**, *107*,

- 7788–7794.
27. Baiz, C. R.; Kubarych, K. J. Ultrafast Vibrational Stark-Effect Spectroscopy: Exploring Charge-Transfer Reactions by Directly Monitoring the Solvation Shell Response. *J. Am. Chem. Soc.* **2010**, *132*, 12784–12785.
 28. Ringer, A. L.; MacKerell Jr, A. D. Calculation of the Vibrational Stark Effect Using a First-Principles Quantum Mechanical/Molecular Mechanical Approach. *J. Phys. Chem. Lett.* **2011**, *2*, 553–556.
 29. Hu, W.; Webb, L. J. Direct Measurement of the Membrane Dipole Field in Bicelles Using Vibrational Stark Effect Spectroscopy. *J. Phys. Chem. Lett.* **2011**, *2*, 1925–1930.
 30. Marr, J. M.; Schultz, Z. D. Imaging Electric Fields in SERS and TERS Using the Vibrational Stark Effect. *J. Phys. Chem. Lett.* **2013**, *4*, 3268–3272.
 31. Pazos, I. M.; Ghosh, A.; Tucker, M. J.; Gai, F. Ester Carbonyl Vibration as a Sensitive Probe of Protein Local Electric Field. *Angew. Chem. Int. Ed.* **2014**, *53*, 6080–6084.
 32. Park, Y.; Kang, H.; Field, R. W.; Kang, H. The Frequency-Domain IR Spectrum of Ammonia Encodes Changes in Molecular Dynamics Caused by a DC Electric Field. *Proc. Natl. Acad. Sci. U.S.A.* **2019**, *116*, 23444–23447.
 33. Horowitz, Y.; Asscher, M. Low Energy Charged Particles Interacting with Amorphous Solid Water Layers. *J. Chem. Phys.* **2012**, *136*, 134701.
 34. Shin, S.; Kim, Y.; Kang, H.; Kang, H. Effect of Electric Field on Condensed-Phase Molecular Systems. I. Dipolar Polarization of Amorphous Solid Acetone. *J. Phys. Chem. C* **2015**, *119*, 15588–15595.
 35. Ayotte, P.; Plessis, S.; Marchand, P. Trapping Proton Transfer Intermediates

- in the Disordered Hydrogen-Bonded Network of Cryogenic Hydrofluoric Acid Solutions. *Phys. Chem. Chem. Phys.* **2008**, *10*, 4785–4792.
36. Cholette, F.; Zubkov, T.; Smith, R. S.; Dohnalek, Z.; Kay, B. D.; Ayotte, P. Infrared Spectroscopy and Optical Constants of Porous Amorphous Solid Water. *J. Phys. Chem. B* **2009**, *113*, 4131–4140.
37. Engdahl, A.; Nelander, B. Water in Krypton Matrices. *J. Mol. Struct.* **1989**, *193*, 101–109.
38. Ceponkus, J.; Uvdal, P.; Nelander, B. Water Tetramer, Pentamer, and Hexamer in Inert Matrices. *J. Phys. Chem. A* **2012**, *116*, 4842–4850.
39. Ohno, K.; Okimura, M.; Akai, N.; Katsumoto, Y. The Effect of Cooperative Hydrogen Bonding on the OH Stretching-Band Shift for Water Clusters Studied by Matrix-Isolation Infrared Spectroscopy and Density Functional Theory. *Phys. Chem. Chem. Phys.* **2005**, *7*, 3005–3014.
40. Hirabayashi, S.; Yamada, K. M. Infrared Spectra of Water Clusters in Krypton and Xenon Matrices. *J. Chem. Phys.* **2005**, *122*, 244501.
41. Hirabayashi, S.; Yamada, K. M. Infrared Spectra and Structure of Water Clusters Trapped in Argon and Krypton Matrices. *J. Mol. Struct.* **2006**, *795*, 78–83.
42. Gregory, J.; Clary, D.; Liu, K.; Brown, M.; Saykally, R. The Water Dipole Moment in Water Clusters. *Science* **1997**, *275*, 814–817.
43. Böttcher, C. J. F. *Theory of Electric Polarization*; Elsevier: Amsterdam, NY, 1973.
44. Corcelli, S. A.; Lawrence, C. P.; Skinner, J. L. Combined Electronic Structure/Molecular Dynamics Approach for Ultrafast Infrared Spectroscopy of Dilute HOD in Liquid H₂O and D₂O. *J. Chem. Phys.* **2004**, *120*, 8107–8117.

45. Sen, S.; Boda, M.; Lata, S. V.; Patwari, G. N. Internal Electric Fields in Small Water Clusters $[(\text{H}_2\text{O})_n; n=2-6]$. *Phys. Chem. Chem. Phys.* **2016**, *18*, 16730–16737.
46. Lim, J. H.; Cho, D.; Kang, H.; Lee, J. Y. Electronic and Nuclear Contributions to Vibrational Stark Shifts of Hydroxyl Stretching Frequencies of Water Clusters. *J. Phys. Chem. C* **2018**, *122*, 12970–12974.
47. Sliter, R.; Gish, M.; Vilesov, A. F. Fast Nuclear Spin Conversion in Water Clusters and Ices: A Matrix Isolation Study. *J. Phys. Chem. A* **2011**, *115*, 9682–9688.

Chapter 5

Spectroscopic Evidence of Large Protonic Polarizability of Hydrogen Chloride–Water Complex

Abstract

Vibrational Stark spectroscopic experiments were conducted to examine the electrostatic polarizability of acidic proton in the HCl–H₂O and HCl–D₂O complexes isolated in solid Ar matrices under the influence of uniquely strong (10^8 V/m) electric fields. The field-dependent vibrational spectra of the complexes showed an extraordinarily large Stark-shift of proton vibration (H–Cl stretch) frequency compared to that of isolated HCl molecule. The electric field also changed the coupling between the proton vibration and the normal mode of D₂O in HCl–D₂O complex. Spectral analysis aided by quantum structure calculation reveals reversible displacement of the acidic proton in HCl–water complex by the applied field. The protonic polarizability of the complex is very large and asymmetric with respect to the elongation and contraction of H–Cl bond length.

Main Text

Dissociation of a protonic acid is one of the most fundamental processes in aqueous solution chemistry and heterogeneous reaction chemistry. Intensive theoretical and experimental studies have been conducted to understand detailed mechanisms for the dissociation of protonic acid [1, 2]. A key concept in the discussion of acid dissociation is the ‘protonic polarizability’ of an acid in hydration environment [1]. Because the acidic proton with partial charge can be moved by electric forces, the electrostatic polarizability of H–X bond for hydrogen-bonded acid molecules can be very large compared to that solely due to the distortion of electron clouds. Zundel [1] proposed that the large protonic polarizability of a hydrated acid, either in the molecular or dissociated form, is responsible for the appearance of IR continua in the absorption spectra of acidic aqueous solutions. Electric fields exerted by the local hydration structure can greatly shift the vibrational frequency of polarizable H–X bond of an acid to produce the absorption continua, according to theoretical calculations on acid–water clusters [3–6]. Wolke et al. [7] studied the vibrational spectra of hydronium structures complexed with various hydrogen-bonded acceptor molecules in gas phase. They observed that the proton vibration frequency of hydroniums greatly changes with the proton affinity of the complexed molecule, which can be attributed to internal field-induced displacement of protons in the complexes. Electric fields also actuate biological structures with large protonic polarizability, such as the proton pathways in membranes [1] and enzyme catalysis mechanisms [8].

Despite general recognition that the protonic polarizability plays a crucial role in acid dissociation, this property for acid has not yet been directly observed under the conditions of controlled external electric fields. In this communication, we

report the observation of large protonic polarizability of HCl–water 1:1 complex isolated in a solid Ar matrix. Extensive studies have been done for small clusters of HCl and water generated in the gas phase or isolated in the inert solid matrix to understand the hydration structures and reactions of acid [2, 9–17], and the monohydrated HCl is one of the simplest forms of hydrated acid clusters. We have applied a uniquely strong ($<1.5 \times 10^8$ V/m) electric field to the matrix-isolated HCl–H₂O complex using the ice film nanocapacitor method [18, 19]. The H–Cl stretching vibration of the complex exhibits a drastically large frequency shift in electric field due to large protonic polarizability. In the case of HCl–D₂O complex, where the H–Cl vibration and the symmetric stretching vibration of D₂O are strongly coupled together, the applied field changes the intra-complex coupling behavior.

Figure 5-1(a) shows the result of reflection–absorption IR spectroscopic (RAIRS) measurement of H–Cl stretching vibration, $\nu_{\text{stretch}}(\text{H–Cl})$, of the HCl–H₂O 1:1 complex at the scanned field strength from zero to 1.2×10^8 V/m. The $\nu_{\text{stretch}}(\text{H–Cl})$ band originally appearing at 2663 cm^{-1} at zero field [13, 14] became broadened and separated into two components as the field strength increased. The spectral changes were reversible with respect to the increase or decrease of field strength. The band broadening at moderate field strength can be attributed to the Stark shift of the vibrational frequencies of an ensemble of isotropically orientated molecules [20]. The HCl–H₂O complex in the rigid Ar matrix must have retained the initial isotropic orientation without being reoriented by the applied field.

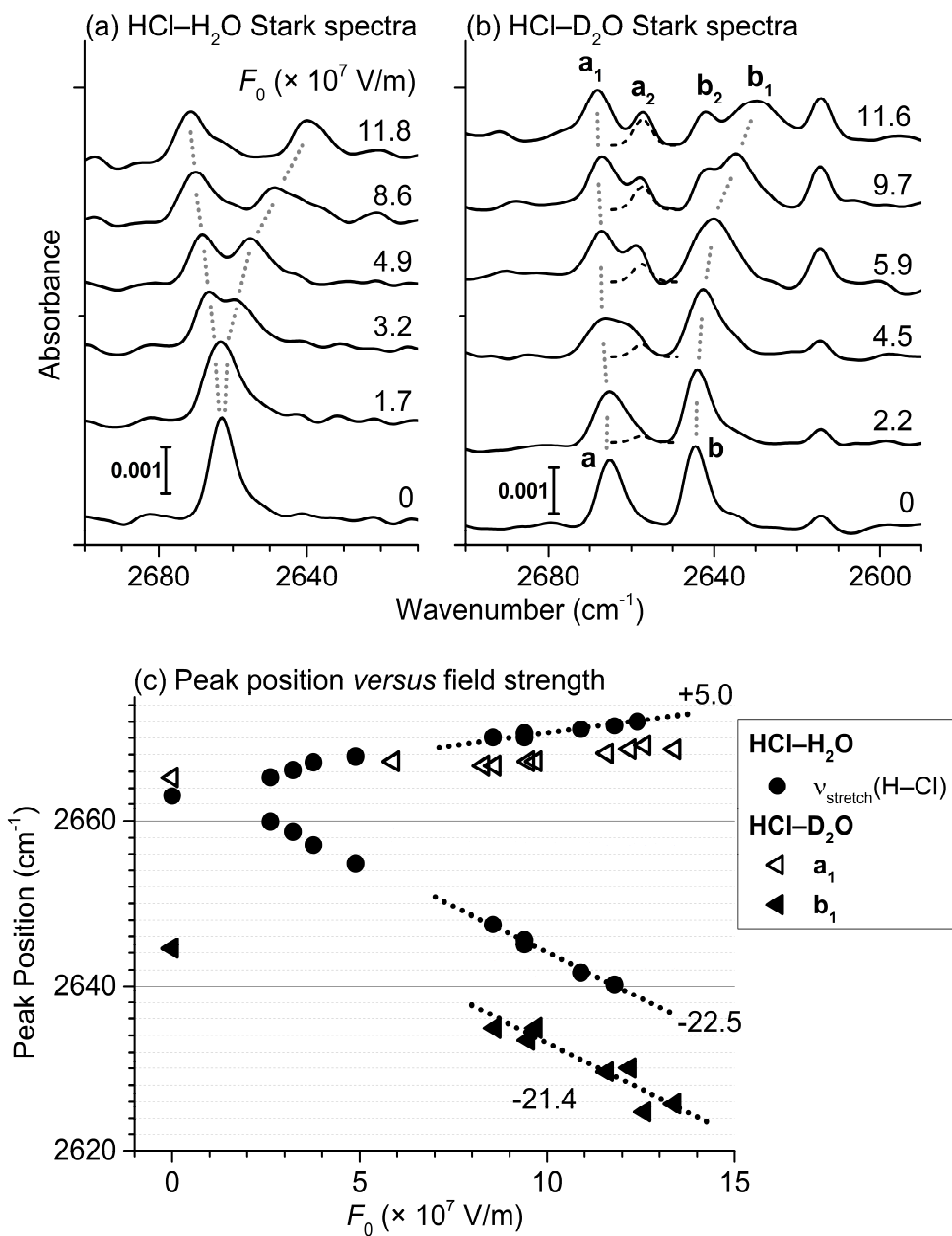


Figure 5-1. (a) RAIR spectra of the $\nu_{\text{stretch}}(\text{H-Cl})$ of the matrix-isolated HCl-H₂O 1:1 complex, acquired as a function of external electric field strength. (b) RAIR spectra of the HCl-D₂O 1:1 complex acquired in a similar manner. The features related to

the proton vibration are marked with ‘a’ and ‘b’ at the zero field spectrum. The dashed profiles at the ‘a₂’ peak position indicate the intensity of $\nu_{\text{sym.stretch}}(\text{D}_2\text{O})$ band of D₂O monomer in the matrices at each stage of field strength (see Figure 5-S3). The peak at 2615 cm⁻¹ is assigned to $\nu_{\text{stretch}}(\text{D}_2\text{O})$ of (D₂O)₂ in the Ar matrix, which is beyond the scope of this work. (c) Plot of the position of the peaks shown in (a) and (b) as a function of the field strength. The slopes of linear fit for the peak position shift are marked in the unit of cm⁻¹/(10⁸ V/m).

The splitting of $\nu_{\text{stretch}}(\text{H-Cl})$ band into two separate components at stronger field results from a large Stark shift of $\nu_{\text{stretch}}(\text{H-Cl})$, which manifests an extremely large field-susceptibility of this vibration. Note that a band splits, rather than broadens, when the frequency shift is very large and the spectrum is acquired with p-polarized light parallel to the applied electric field direction [21]. The field-induced changes of the peak position of $\nu_{\text{stretch}}(\text{H-Cl})$, one in red and the other in blue direction, are plotted as circle points in Figure 5-1(c). The slope of a linear fit for the peak position change gives the estimation of Stark sensitivity of the vibration, defined as $\Delta\mu = \Delta\tilde{\nu}/F_{\text{ext}}$ where $\Delta\tilde{\nu}$ is the change of vibrational frequency under field and F_{ext} is the strength of external field. The magnitude of $\Delta\mu$ estimated from the plot of red-shifting component is $c_{\text{dist}} \times 22.5 \text{ cm}^{-1}/(10^8 \text{ V/m})$, where the coefficient c_{dist} is introduced to account for the isotropic angular distribution of the complexes with respect to the field direction. c_{dist} is expected to be 1.2–1.4 according to simple molecular geometry analysis. This $\Delta\mu$ value of HCl–H₂O complex is one order of magnitude larger than that of HCl monomer in the Ar matrix, 2.7 cm⁻¹/(10⁸ V/m) [22], and that of OH stretch in hydrogen-bonded clusters, 2.3–2.6 cm⁻¹/(10⁸ V/m) [23–25]. In addition, it is about 4–5 times larger than the $\Delta\mu$ value estimated for the blue-shift in Figure 5-1(c), $c_{\text{dist}} \times 5.0 \text{ cm}^{-1}/(10^8 \text{ V/m})$.

Figure 5-1(b) shows the Stark spectra of the HCl–D₂O 1:1 complex in the Ar matrix. The vibrational spectrum of HCl–D₂O 1:1 complex has not been reported previously. We interpret that two peaks in the zero-field spectrum, labeled as ‘**a**’ (2665 cm⁻¹) and ‘**b**’ (2645 cm⁻¹), are produced by vibrational coupling of the H–Cl stretching mode and the symmetric stretching mode of D₂O in the complex (Supporting Information B). Additional peaks appear in the high-field spectra. The peak ‘**a**₂’ is assigned to the symmetric stretching of D₂O monomer present in the Ar matrix, rather than the proton vibration of HCl–D₂O 1:1 complex. The field-induced orientation of D₂O monomer in the Ar matrix makes this peak visible at high electric field [26]. The peak ‘**b**₂’ is assigned to D₂O vibrations in the 1:2 or 2:1 complexes. With the peaks ‘**a**₂’ and ‘**b**₂’ excluded from the features of HCl–D₂O 1:1 complex, the field-induced spectral changes in Figure 5-1(b) can be more clearly related to the proton vibration of the complex. The peak ‘**a**₁’ exhibits a slow blue-shift with an increase in field strength and the peak ‘**b**₁’, a red-shift with a much faster rate. Figure 5-1(c) compares the Stark shifts of these peaks with those of corresponding features of HCl–H₂O complex. The HCl–H₂O and HCl–D₂O complexes show resemblance in the Stark behavior, with $\Delta\mu/c_{\text{dist}}$ being about $-22 \text{ cm}^{-1}/(10^8 \text{ V/m})$ for the red-shifting peaks for both species.

Figure 5-2(a, b) shows two sets of Stark spectra for HCl–H₂O and HCl–D₂O, each set under the similar strength of external field. We simulated the field-driven spectral changes based on the model of large polarizability of acidic proton in the complexes. In this model, the external fields modify the potential energy surfaces along the proton-transfer coordinate and thereby lead to the displacement of proton within the complex to a certain extent. The spectral simulation was aided by quantum chemical calculation. The H–Cl distance ($r(\text{H–Cl})$) in the complex was artificially modified and frozen, followed by optimization of the other structural

parameters and subsequent vibrational analysis to obtain harmonic frequency and intensity at each distance-modified structure. Density functional theory (DFT) calculations with B3LYP functional [27, 28] and 6-311++G(3df,3pd) basis sets were performed using the Gaussian 09 suite of programs [29].

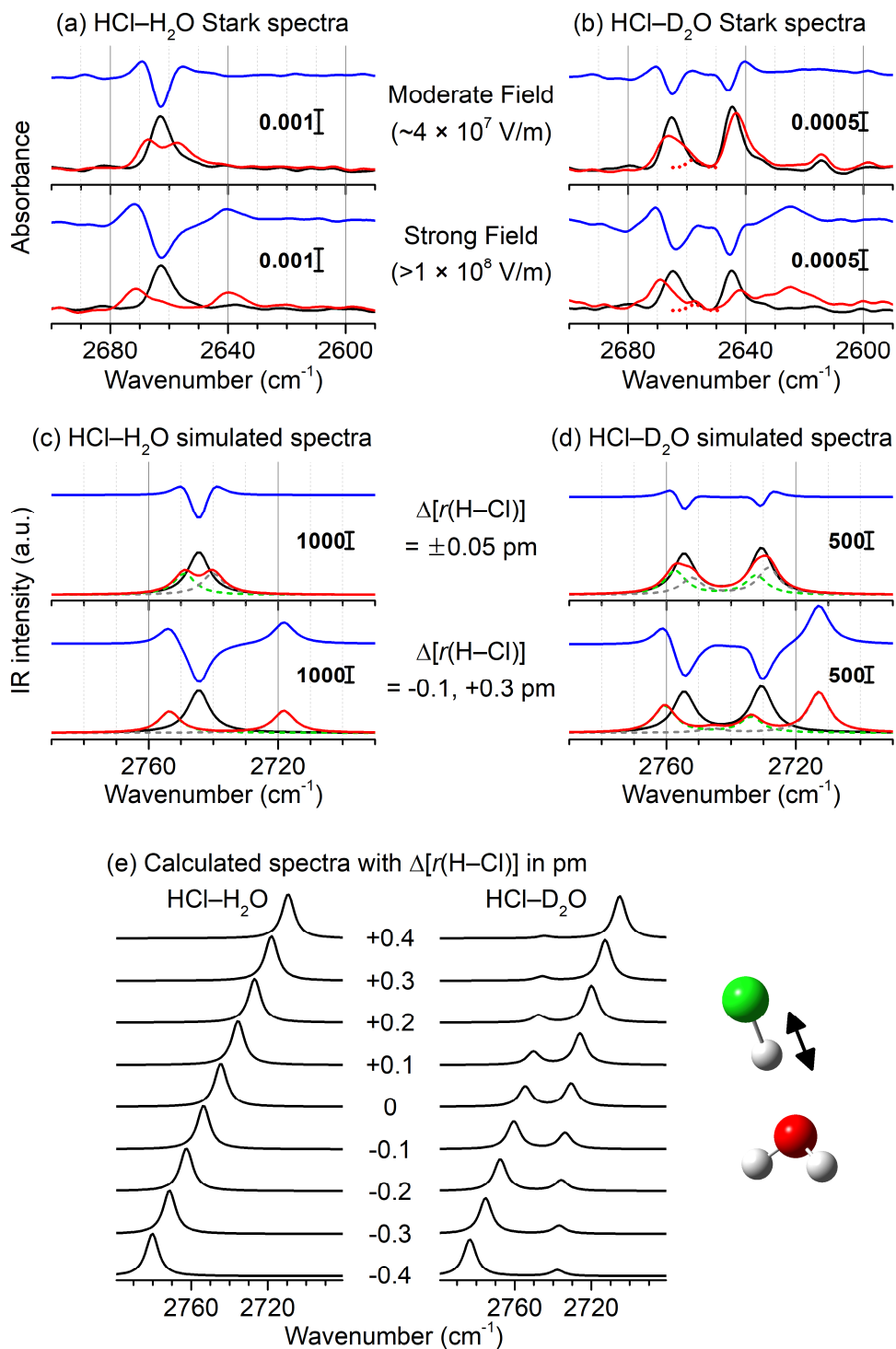


Figure 5-2. (a, b) Comparison of field-induced spectral changes of the proton vibrations between (a) HCl–H₂O and (b) HCl–D₂O complexes. The black, red, and blue lines indicate the spectra at zero field, spectra acquired under external fields, and the difference spectra, respectively. (Top) Under moderate fields (3.8×10^7 V/m for HCl–H₂O, 3.9×10^7 V/m for HCl–D₂O). (Bottom) Under strong fields (1.2×10^8 V/m for HCl–H₂O, 1.3×10^8 V/m for HCl–D₂O). The red dotted lines show the contribution of the $\nu_{\text{sym.stretch}}(\text{D}_2\text{O})$ of D₂O monomer for the spectra of HCl–D₂O. (c, d) Simulated spectra for (c) HCl–H₂O and (d) HCl–D₂O 1:1 complexes. The black lines correspond to the zero-field spectrum, which is simulated for the strongest-coupling geometry between the H–Cl stretching and D₂O symmetric stretching for the HCl–D₂O complex. The spectra are calculated upon the artificial change of $r(\text{H–Cl})$: one half of the ensemble with decreased $r(\text{H–Cl})$ (green dashed lines) from the zero-field geometry and the other half with increased $r(\text{H–Cl})$ (gray dashed lines). The red lines are the sum of the green and gray lines at each plot. The blue lines are the difference between the red and black lines. (Top panel) $\Delta[r(\text{H–Cl})] = \pm 0.05$ pm; (bottom panel) $\Delta[r(\text{H–Cl})] = -0.1, +0.3$ pm. (e) Spectral evolution calculated for HCl–H₂O and HCl–D₂O complexes upon artificial changes in $r(\text{H–Cl})$, both positively and negatively from the strongest-coupling geometry marked with $\Delta[r(\text{H–Cl})] = 0$.

The simulated spectra for HCl–H₂O and HCl–D₂O are depicted in Figure 5-2(c, d). Starting from the strongest-coupling point of the proton vibration and the symmetric stretching of D₂O in HCl–D₂O complex, where the resulting transitions showed 24 cm^{-1} separation which accords with the experimentally observed separation between peaks ‘a’ and ‘b’ (20 cm^{-1}), one half of intensity was subjected to an increase of $r(\text{H–Cl})$ as a hypothetical influence of parallel external field to the

dipole while the other half to a decrease of $r(\text{H-Cl})$ to simulate the effect of anti-parallel field. The artificial modifications of $r(\text{H-Cl})$ in Figure 5-2(c, d) were selected to simulate field-induced frequency changes in Figure 5-2(a, b) as similarly as possible. The intermolecular coupling between the H-Cl stretch and the D₂O symmetric stretch in the HCl-D₂O complex sensitively changes as $r(\text{H-Cl})$ varies, as shown in Figure 5-2(e) (more detailedly in Figure 5-S4 in Supporting Information). This manipulation of coupling efficiency is reflected in the simulated spectra in Figure 5-2(d).

The circumstance reflected in the simulation above is an extreme. In reality, the dipole of complexes would have an isotropic distribution of orientation with respect to the field direction, rather than only parallel and anti-parallel orientation. Nevertheless, the simple simulation with a change in $r(\text{H-Cl})$ reproduced the major features of the experimental results in Figure 5-2(a, b). Note that, in Figure 5-2(c, d), a single parametric change in $r(\text{H-Cl})$ was used to model both HCl-H₂O and HCl-D₂O spectra. The discrepancy in absolute frequency between calculations and experiments originates from the inaccuracy of DFT calculations (often corrected with 0.9–1 scaling factors for $>2000\text{ cm}^{-1}$ stretching modes) and the matrix effect [26, 30, 31].

Agreement between the calculated and experimental spectra provides a quantitative estimation of the protonic polarization: $\Delta[r(\text{H-Cl})]/c_{\text{dist}} = 0.3$ and 0.1 pm in the directions of H-Cl bond elongation and contraction, respectively, at the apparent field strength $1.2\text{--}1.3 \times 10^8\text{ V/m}$. Therefore, the protonic polarizability is highly asymmetric with respect to the direction of applied field. The polarization is driven by dipole–electric field interaction energy, where the proton dislocation changes the dipole moment of the complex toward electrostatic stabilization (Figure 5-S5 in Supporting Information).

This work demonstrates that external electrostatic fields with controlled strength can reversibly displace the acidic proton in the HCl–water complex along the proton-transfer coordinate. The protonic polarizability of the complex is extraordinarily large, corresponding to the Stark sensitivity of $\Delta\mu > 20 \text{ cm}^{-1}/(10^8 \text{ V/m})$, compared to that of HCl monomer. The present experiment observed the proton displacement of only 0.09–0.3% of the original H–Cl bond length ($\sim 130 \text{ pm}$) at the field strength of $\sim 1 \times 10^8 \text{ V/m}$. Yet, extension of the protonic polarizability to $\sim 1 \times 10^{10} \text{ V/m}$, a typical field strength inside the hydration sphere [5–7], predicts $\Delta[r(\text{H–Cl})] \sim 30 \text{ pm}$ and $\Delta\tilde{\nu} > 2000 \text{ cm}^{-1}$. This estimation is consistent with the ionization of HCl upon hydration in aqueous solution with the appearance of IR absorption continua at 500–3000 cm^{-1} [1]. The larger protonic polarizability in the direction of $r(\text{H–Cl})$ elongation than contraction suggests possibility that the thermal fluctuations of local electric field play an important role in the acid dissociation mechanism. It implies the cooperativity of hydration; the directly hydrogen-bonded water molecules make the H–Cl bond highly polarizable, while the electrostatic field arising from the surrounding molecules drives the bond dissociation.

References

1. Zundel, G. Hydrogen Bonds with Large Proton Polarizability and Proton Transfer Processes in Electrochemistry and Biology. *Adv. Chem. Phys.* **2000**, *111*, 1–217.
2. Leopold, K. R. Hydrated Acid Clusters. *Annu. Rev. Phys. Chem.* **2011**, *62*, 327–349.
3. Cabaleiro-Lago, E. M.; Hermida-Ramón, J. M.; Rodríguez-Otero, J. Computational Study of the Dissociation of H–X Acids (X= F, Cl, Br, I) in Water Clusters. *J. Chem. Phys.* **2002**, *117*, 3160–3168.
4. Alikhani, M.; Silvi, B. Ab initio Study of (H₂O)_{1,2}·HCl: Accurate Energetic and Frequency Shift of HCl. *Phys. Chem. Chem. Phys.* **2003**, *5*, 2494–2498.
5. Boda, M.; Patwari, G. N. Insights into Acid Dissociation of HCl and HBr with Internal Electric Fields. *Phys. Chem. Chem. Phys.* **2017**, *19*, 7461–7464.
6. Conley, C.; Tao, F.-M. Ionic Dissociation of Hydrogen Bromide in Water Clusters: A Computational Study. *Chem. Phys. Lett.* **1999**, *301*, 29–36.
7. Wolke, C. T.; Fournier, J. A.; Dzugan, L. C.; Fagiani, M. R.; Odbadrakh, T. T.; Knorke, H.; Jordan, K. D.; McCoy, A. B.; Asmis, K. R.; Johnson, M. A. Spectroscopic Snapshots of the Proton-Transfer Mechanism in Water. *Science* **2016**, *354*, 1131–1135.
8. Fried, S. D.; Bagchi, S.; Boxer, S. G. Extreme Electric Fields Power Catalysis in the Active Site of Ketosteroid Isomerase. *Science* **2014**, *346*, 1510–1514.
9. Zischang, J.; Skvortsov, D.; Choi, M. Y.; Mata, R. A.; Suhm, M. A.; Vilesov, S. M. Proton Transfer in Water Clusters. *J. Chem. Phys.* **2015**, *143*, 124701.

- A. F. Helium Nanodroplet Study of the Hydrogen-Bonded OH Vibrations in HCl–H₂O Clusters. *J. Phys. Chem. A* **2014**, *119*, 2636–2643.
10. Chaban, G. M.; Gerber, R. B.; Janda, K. C. Transition from Hydrogen Bonding to Ionization in (HCl)_n(NH₃)_n and (HCl)_n(H₂O)_n Clusters: Consequences for Anharmonic Vibrational Spectroscopy. *J. Phys. Chem. A* **2001**, *105*, 8323–8332.
 11. Gutberlet, A.; Schwaab, G.; Birer, Ö.; Masia, M.; Kaczmarek, A.; Forbert, H.; Havenith, M.; Marx, D. Aggregation-Induced Dissociation of HCl(H₂O)₄ below 1 K: The Smallest Droplet of Acid. *Science* **2009**, *324*, 1545–1548.
 12. Forbert, H.; Masia, M.; Kaczmarek-Kedziera, A.; Nair, N. N.; Marx, D. Aggregation-Induced Chemical Reactions: Acid Dissociation in Growing Water Clusters. *J. Am. Chem. Soc.* **2011**, *133*, 4062–4072.
 13. Schriver, A.; Silvi, B.; Maillard, D.; Perchard, J. Structure of Water-Hydrochloric Acid Complexes in Argon and Nitrogen Matrices from Infrared Spectra. *J. Phys. Chem.* **1977**, *81*, 2095–2102.
 14. Amirand, C.; Maillard, D. Spectrum and Structure of Water-Rich Water–Hydracid Complexes from Matrix Isolation Spectroscopy: Evidence for Proton Transfer. *J. Mol. Struct.* **1988**, *176*, 181–201.
 15. Weimann, M.; Fárník, M.; Suhm, M. A. A First Glimpse at the Acidic Proton Vibrations in HCl–Water Clusters via Supersonic Jet FTIR Spectroscopy. *Phys. Chem. Chem. Phys.* **2002**, *4*, 3933–3937.
 16. Flynn, S. D.; Skvortsov, D.; Morrison, A. M.; Liang, T.; Choi, M. Y.; Douberly, G. E.; Vilesov, A. F. Infrared Spectra of HCl–H₂O Clusters in Helium Nanodroplets. *J. Phys. Chem. Lett.* **2010**, *1*, 2233–2238.
 17. Morrison, A. M.; Flynn, S. D.; Liang, T.; Douberly, G. E. Infrared

- Spectroscopy of $(\text{HCl})_m(\text{H}_2\text{O})_n$ Clusters in Helium Nanodroplets: Definitive Assignments in the HCl Stretch Region. *J. Phys. Chem. A* **2010**, *114*, 8090–8098.
18. Shin, S.; Kim, Y.; Moon, E.-s.; Lee, D. H.; Kang, H.; Kang, H. Generation of Strong Electric Fields in an Ice Film Capacitor. *J. Chem. Phys.* **2013**, *139*, 074201.
 19. Park, Y.; Kang, H.; Kang, H. Brute Force Orientation of Matrix-Isolated Molecules: Reversible Reorientation of Formaldehyde in an Argon Matrix toward Perfect Alignment. *Angew. Chem. Int. Ed.* **2017**, *56*, 1046–1049.
 20. Bublitz, G. U.; Boxer, S. G. Stark Spectroscopy: Applications in Chemistry, Biology, and Materials Science. *Annu. Rev. Phys. Chem.* **1997**, *48*, 213–242.
 21. Shin, S.; Kang, H.; Cho, D.; Lee, J. Y.; Kang, H. Effect of Electric Field on Condensed-Phase Molecular Systems. II. Stark Effect on the Hydroxyl Stretch Vibration of Ice. *J. Phys. Chem. C* **2015**, *119*, 15596–15603.
 22. Kang, H.; Park, Y.; Kim, Z. H.; Kang, H. Electric Field Effect on Condensed-Phase Molecular Systems. VI. Field-Driven Orientation of Hydrogen Chloride in an Argon Matrix. *J. Phys. Chem. A* **2018**, *122*, 2871–2876.
 23. Saggi, M.; Levinson, N. M.; Boxer, S. G. Direct Measurements of Electric Fields in Weak $\text{OH}\cdots\pi$ Hydrogen Bonds. *J. Am. Chem. Soc.* **2011**, *133*, 17414–17419.
 24. Corcelli, S. A.; Lawrence, C. P.; Skinner, J. L. Combined Electronic Structure/Molecular Dynamics Approach for Ultrafast Infrared Spectroscopy of Dilute HOD in Liquid H_2O and D_2O . *J. Chem. Phys.* **2004**, *120*, 8107–8117.
 25. Sen, S.; Boda, M.; Lata, S. V.; Patwari, G. N. Internal Electric Fields in

- Small Water Clusters [(H₂O)_n; n=2–6]. *Phys. Chem. Chem. Phys.* **2016**, *18*, 16730–16737.
26. Park, Y.; Lim, J. H.; Lee, J. Y.; Kang, H. Electric Field Effect on Condensed-Phase Molecular Systems. VII. Vibrational Stark Sensitivity of Spatially Oriented Water Molecules in an Argon Matrix. *J. Phys. Chem. C* **2019**, *123*, 9868–9874.
27. Becke, A. D. Density-Functional Thermochemistry. III. The Role of Exact Exchange. *J. Chem. Phys.* **1993**, *98*, 5648–5652.
28. Lee, C.; Yang, W.; Parr, R. G. Development of the Colle-Salvetti Correlation-Energy Formula into a Functional of the Electron Density. *Phys. Rev. B* **1988**, *37*, 785–789.
29. Frisch, M. J.; Trucks, G.; Schlegel, H. B.; Scuseria, G.; Robb, M.; Cheeseman, J.; Scalmani, G.; Barone, V.; Mennucci, B.; Petersson, G. A. et al. *Gaussian 09*, Revision A. 1; Gaussian Inc.: Wallingford, CT, 2009.
30. Sinha, P.; Boesch, S. E.; Gu, C.; Wheeler, R. A.; Wilson, A. K. Harmonic Vibrational Frequencies: Scaling Factors for HF, B3LYP, and MP2 Methods in Combination with Correlation Consistent Basis Sets. *J. Phys. Chem. A* **2004**, *108*, 9213–9217.
31. Lambie, B.; Ramaekers, R.; Maes, G. Conformational Behavior of Serine: An Experimental Matrix-Isolation FT-IR and Theoretical DFT(B3LYP)/6-31++G** Study. *J. Phys. Chem. A* **2004**, *108*, 10426–10433.

Supporting Information

A. Experimental details

The experiments were performed in an ultrahigh vacuum (UHV) chamber which has been described in detail elsewhere [1–3]. The molecular films were prepared on a cold Pt(111) substrate (about 10 K) by sequential deposition of the gaseous species which were introduced into the UHV chamber through variable leak valves. H₂O (Milli-Q) and D₂O (Aldrich, 99 atom% D) were purified by several freeze–pump–thaw cycles. Ar (99.999%) and HCl (Sigma-Aldrich, >99%) gases were used from commercially available gas cylinders without additional purification processes. A tube doser was used to guide HCl gas close to the Pt(111) substrate. Other gases were back-filled.

The film of HCl–H₂O (HCl–D₂O) complexes isolated in the Ar matrix was prepared by co-adsorption of HCl, H₂O (D₂O) and Ar gases in predetermined pressure ratios. The sample had a stacked structure of an Ar film (288–960 ML thickness; ML = monolayer; 1 ML = 1.1×10^{15} molecules/cm²) containing HCl and H₂O (D₂O), sandwiched between two Ar spacer layers (96–120 ML each). The spacer layers prevent the isolated molecules and complexes from being affected by interfacial effects. The upper Ar film was capped by an amorphous H₂O film (25 ML). D₂O was not used to constitute the capping layer, since its intense broad OD stretching band, which overlaps with HCl stretching region in the IR spectra, restricts a reliable observation of HCl vibrations.

A dc electrostatic field was applied across the film using the previously demonstrated [1, 2, 4, 5] ice film nanocapacitor method. The strength of the

externally applied electric field across the Ar matrix was estimated from the film voltage developed by Cs⁺ ion deposition on the surface of the capping H₂O film, measured with a Kelvin probe. All field strength values given in this paper are those of macroscopic field (F_0), obtained simply by dividing the voltage across the film by the film thickness. The actual field strength (F) that a matrix-isolated molecule or a complex experiences is expressed by $F = c_{local}F_0$, with the local field correction factor, c_{local} , estimated to be in the range of 1–2 [2, 6].

Reflection–absorption infrared spectroscopic (RAIRS) measurements were conducted with a Fourier transform infrared (FTIR) spectrometer with a liquid nitrogen-cooled mercury cadmium telluride detector in grazing angle reflection geometry (85°). An incident IR beam was p-polarized by a wire grid polarizer. The spectra were averaged 1024 times at a spectral resolution of 4 cm⁻¹. The sloped baselines of spectra, caused by the increasing negative reflection–absorption with increasing wavenumber [7, 8], were corrected for better visualization.

B. Assignment of peaks in the zero-field spectrum of HCl–D₂O complex

The peaks ‘a’ (2665 cm⁻¹) and ‘b’ (2645 cm⁻¹) are attributed to coupling of the H–Cl stretching vibration and the symmetric stretching vibration of D₂O in the complex, for the reasons listed below. First, these two local vibrations are close in frequency and have the symmetries to be coupled with each other. Note the symmetric stretching frequency of D₂O monomer in the Ar matrix is 2658 cm⁻¹ [5, 9], which is in the vicinity of $\nu_{stretch}(H-Cl)$ frequency. Second, each peak of ‘a’ and ‘b’ in the zero-field spectrum of Figure 5-1(b) has about half of the intensity of the 2663 cm⁻¹ peak

of the HCl–H₂O complex in Figure 5-1(a), when identical experimental conditions are used to obtain the HCl–H₂O and HCl–D₂O spectra at zero field. Third, the peaks ‘**a**’ and ‘**b**’ appear at significantly different frequencies from the $\nu_{\text{stretch}}(\text{H–Cl})$ peak of HCl–H₂O complex. Fourth, evolution of the calculated spectrum of HCl–D₂O complex upon artificial changes in $r(\text{H–Cl})$ clearly predict coupling of the H–Cl stretching vibration and the D₂O symmetric stretching vibration (Figure 5-2(e) and Figure 5-S4). These features indicate that the H–Cl stretching motion in the HCl–D₂O complex is no longer localized but strongly coupled to the vibrations of hydrogen-bonded water. It might be considered that the peak ‘**b**’ is contributed by the O–D stretching vibrations of HCl–D₂O 1:2 or 2:1 complexes that are also present in the matrix samples [10]. However, the field-driven changes in the peak shape of ‘**b**’, especially the large red-shift of ‘**b**₁’ feature, is too drastic to be considered to originate from the vibrational Stark effect of D₂O vibrations in these complexes. In addition, the field-induced changes of the ‘**a**’ and ‘**b**’ peak shapes are independent of the population change of HCl–D₂O 1:2 and 2:1 complexes in the samples (Figure 5-S2 in Supporting Information). Therefore, the major intensity of the peak ‘**b**’ must originate from the 1:1 complex.

The peak ‘**a**₂’ is assigned as the symmetric stretching peak of D₂O monomer present in the matrix samples, rather than the proton vibration of HCl–D₂O 1:1 complex. The peak grows in intensity without a noticeable frequency shift as the field increases, as depicted by the dashed peak profiles in Figure 5-1(b). Figure 5-S3 depicts a detailed process of extracting this component. The assignment is based on the previous observations that the intensity of symmetric stretching peak of D₂O monomer grows as D₂O molecule is dipole-oriented along the field direction at high field [5].

The identity of the peak ‘b₂’ is uncertain. We note that the ‘b₂’ peak position is nearly identical to the ‘b’ peak position at zero field and remains unshifted when the field strength is changed. Therefore, it is unlikely to be due to an acidic proton but is possibly related to D₂O vibrations in the 1:2 or 2:1 complexes.

C. Supporting Figures

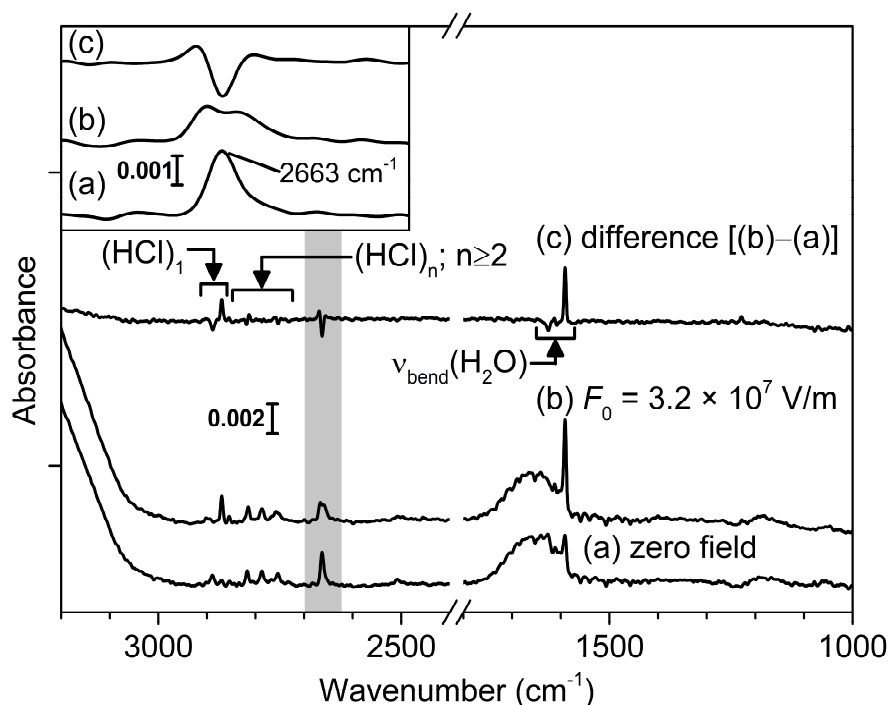


Figure 5-S1. RAIR spectra of the Ar film containing HCl and H₂O molecules inside, (a) at zero field and (b) under field whose strength is 3.2×10^7 V/m. (c) Difference spectrum of (b) and (a). The spectral region for the $\nu_{\text{stretch}}(\text{H}-\text{Cl})$ of HCl–H₂O 1:1 complex (2663 cm^{-1}) is marked by the shaded gray and shown magnified in the inset.

Various peaks appearing at $2730\text{--}2900 \text{ cm}^{-1}$ and 1600 cm^{-1} in Figure 5-

S1(a) originate from other matrix-isolated species than the HCl–H₂O 1:1 complex, which are explained in the text. The peak at 2888 cm⁻¹ corresponds to the R(0) transition of HCl monomer, 2818 and 2787 cm⁻¹ to the $\nu_{\text{stretch}}(\text{H-Cl})$ of HCl dimer and trimer, respectively, 2780–2730 cm⁻¹ to larger multimers [1, 11], features around 1600 cm⁻¹ to the $\nu_{\text{bend}}(\text{H}_2\text{O})$ of H₂O monomer and clusters [9]. The broad features appearing above 3000 cm⁻¹ and at around 1660 cm⁻¹ originate from stretching and bending vibrations of bulk H₂O film, respectively, which was used as a capping layer for the ice film nanocapacitor.

When the external field is applied across the film (Figure 5-S1(b)), the spectrum showed dramatic changes as depicted in Figure 5-S1(c), some of which have already reported by the previous studies in our group [1, 5]. The removal of the R(0) peak (2888 cm⁻¹) and emergence of the band center peak (2871 cm⁻¹) of HCl monomer is the indication of field-induced orientation of the matrix-isolated HCl monomer [1]. The dips at 1624 and 1608 cm⁻¹ and the significant increase at 1589 cm⁻¹ is the consequence of reorientation of H₂O monomer along the direction of external field [5]. Other spectral changes in the $\nu_{\text{stretch}}(\text{H-Cl})$ region of HCl clusters are not well-explained yet.

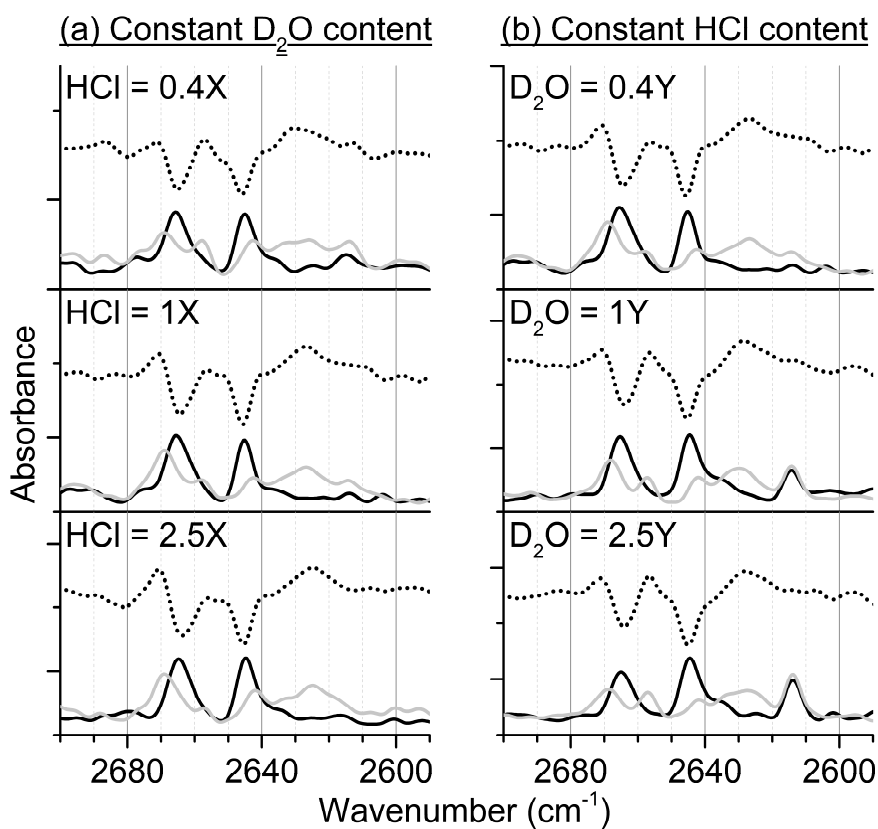


Figure 5-S2. Stark spectra of the film containing HCl and D₂O acquired at various pressure ratios of Ar, HCl, and D₂O, (a) series of constant D₂O pressure and (b) constant HCl. The black and gray solid lines indicate the spectra at zero field and under fields (about 1.2×10^8 V/m), respectively, and the difference spectra between them are displayed with dotted lines.

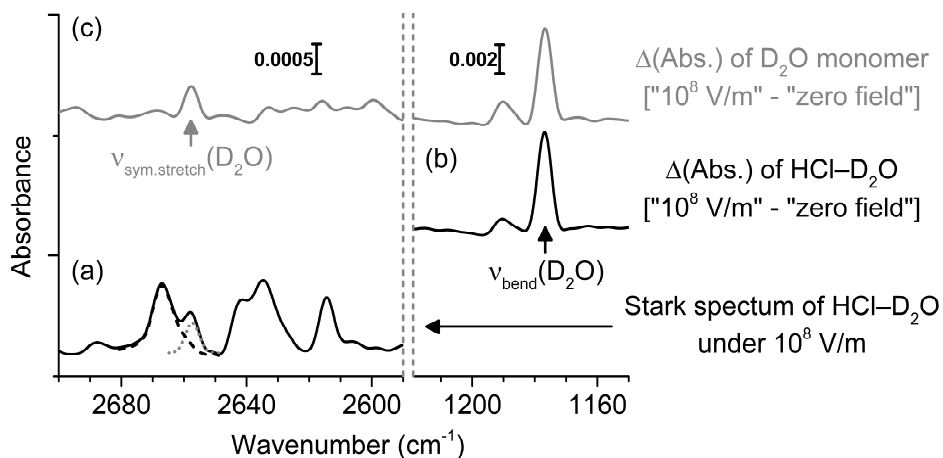


Figure 5-S3. This figure illustrates how the symmetric stretching band of D₂O monomer, marked with dashed lines in Figure 5-1(b) and red-dotted lines in Figure 5-2(b), which overlaps with the band of the HCl–D₂O complex in the Stark spectra, was estimated. Black solid line in (a) is the spectrum of the matrix-isolated HCl–D₂O complex under the external field whose strength is about 1×10^8 V/m. Line in (b) shows the difference spectrum of the black line with its zero field spectrum (not shown) in the bending vibration region of D₂O monomer isolated in the film. The intense rise in the difference spectrum (b) corresponds to the bending vibration origin peak of D₂O monomer oriented to the external field direction. The gray solid line in (c) displays the difference spectrum, between the spectra under 1×10^8 V/m field and at zero field, of the matrix which is comprised only of D₂O. The difference spectrum in (c) was scaled by a certain factor to make the intensity of the bending vibration peak of D₂O monomer identical with that of the difference spectrum in (b). Under this circumstance, the symmetric stretching band of D₂O monomer in the line at 2658 cm^{-1} in (c) is extracted (gray dotted line in (a)) and used as an estimation of that involved in the Stark spectrum of the HCl–D₂O complex. Black dashed line in (a) is the result of subtracting the gray dotted line from the black solid line in (a).

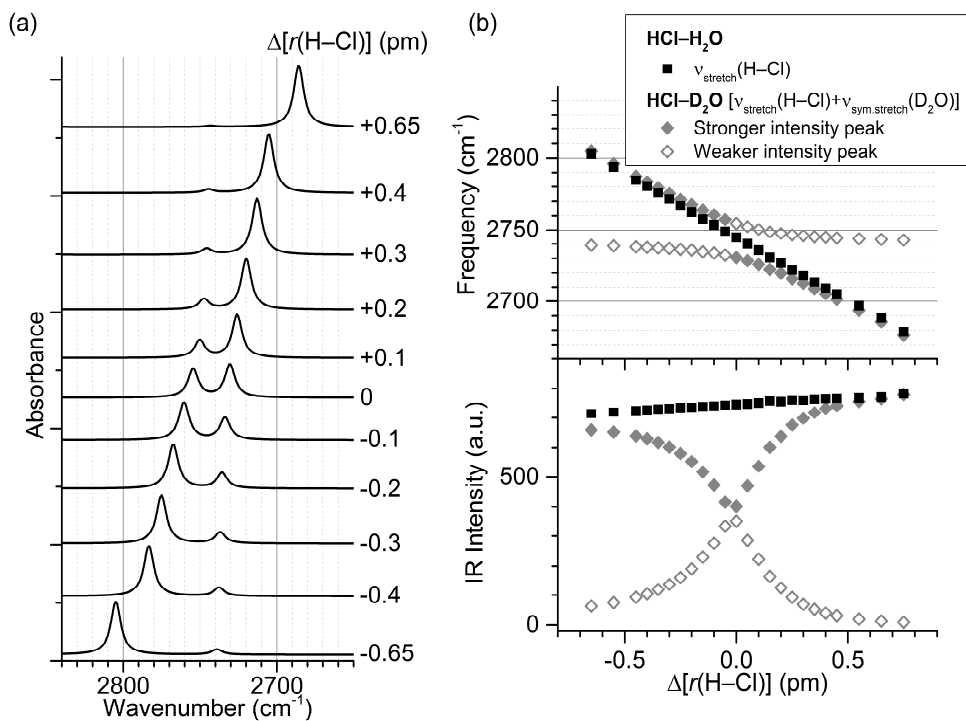


Figure 5-S4. (a) Simulated spectra of the HCl-D₂O complex in the H-Cl stretching and D₂O symmetric stretching region. H-Cl distance ($r(\text{H-Cl})$) was artificially changed both positively and negatively from the strongest-coupling structure as a reference point, which is marked as $\Delta[r(\text{H-Cl})] = 0$ in the Figure. The distance $r(\text{H-Cl})$ at the strongest-coupling structure was 129.15 pm. See the main text for details on the calculation. (b) The calculated frequency and IR intensity of the proton vibrations of HCl-H₂O and HCl-D₂O.

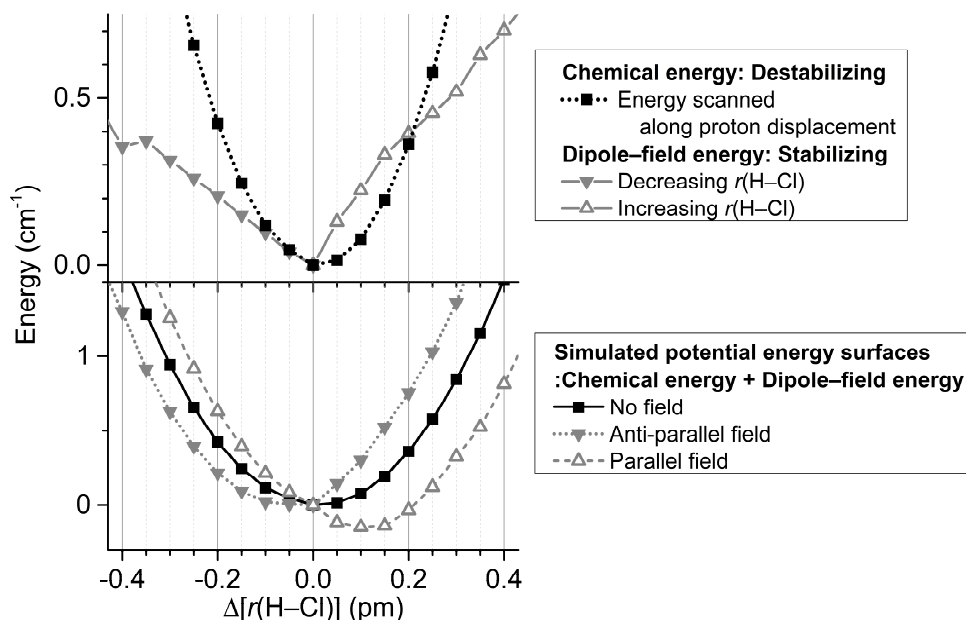


Figure 5-S5. (Top) Calculated energies of the HCl–water 1:1 complex upon the displacement of proton. The energy and dipole moment was calculated for the optimized structure with frozen $r(\text{H-Cl})$, as mentioned in the main text in detail. The dipole–field energy shown in the plot is the absolute magnitude of $u = -\boldsymbol{\mu} \cdot \boldsymbol{F}$ under the influence of the external field with $2 \times 10^8 \text{ V/m}$ strength which is parallel (or anti-parallel) to the dipole moment. The dipole–field energy in increasing $r(\text{H-Cl})$ direction exceeds the chemical destabilization energy up to $\Delta[r(\text{H-Cl})] = +0.2 \text{ pm}$ at $2 \times 10^8 \text{ V/m}$, whereas in decreasing $r(\text{H-Cl})$ direction, the field-driven energy gain hardly overcomes the destabilization. (Bottom) Simulated potential energy surfaces calculated from the sum of zero-field potential surface with the dipole–field interaction energy.

References for Supporting Information

1. Kang, H.; Park, Y.; Kim, Z. H.; Kang, H. Electric Field Effect on Condensed-Phase Molecular Systems. VI. Field-Driven Orientation of Hydrogen Chloride in an Argon Matrix. *J. Phys. Chem. A* **2018**, *122*, 2871–2876.
2. Park, Y.; Kang, H.; Kang, H. Brute Force Orientation of Matrix-Isolated Molecules: Reversible Reorientation of Formaldehyde in an Argon Matrix toward Perfect Alignment. *Angew. Chem. Int. Ed.* **2017**, *56*, 1046–1049.
3. Kang, H.; Shin, S.; Park, Y.; Kang, H. Electric Field Effect on Condensed-Phase Molecular Systems. III. The Origin of the Field-Induced Change in the Vibrational Frequency of Adsorbed CO on Pt (111). *J. Phys. Chem. C* **2016**, *120*, 17579–17587.
4. Shin, S.; Kim, Y.; Moon, E.-s.; Lee, D. H.; Kang, H.; Kang, H. Generation of Strong Electric Fields in an Ice Film Capacitor. *J. Chem. Phys.* **2013**, *139*, 074201.
5. Park, Y.; Lim, J. H.; Lee, J. Y.; Kang, H. Electric Field Effect on Condensed-Phase Molecular Systems. VII. Vibrational Stark Sensitivity of Spatially Oriented Water Molecules in an Argon Matrix. *J. Phys. Chem. C* **2019**, *123*, 9868–9874.
6. Fried, S. D.; Boxer, S. G. Measuring Electric Fields and Noncovalent Interactions Using the Vibrational Stark Effect. *Acc. Chem. Res.* **2015**, *48*, 998–1006.
7. Ayotte, P.; Plessis, S.; Marchand, P. Trapping Proton Transfer Intermediates in the Disordered Hydrogen-Bonded Network of Cryogenic Hydrofluoric Acid Solutions. *Phys. Chem. Chem. Phys.* **2008**, *10*, 4785–4792.

8. Cholette, F.; Zubkov, T.; Smith, R. S.; Dohnalek, Z.; Kay, B. D.; Ayotte, P. Infrared Spectroscopy and Optical Constants of Porous Amorphous Solid Water. *J. Phys. Chem. B* **2009**, *113*, 4131–4140.
9. Engdahl, A.; Nelander, B. Water in Krypton Matrices. *J. Mol. Struct.* **1989**, *193*, 101–109.
10. Amirand, C.; Maillard, D. Spectrum and Structure of Water-Rich Water–Hydracid Complexes from Matrix Isolation Spectroscopy: Evidence for Proton Transfer. *J. Mol. Struct.* **1988**, *176*, 181–201.
11. Hallam, H. E. *Vibrational Spectroscopy of Trapped Species*; Wiley: Hoboken, 1973, pp. 70–80.

Chapter 6

Vibrational Stark Spectroscopy on Proton Vibrations in Proton-Transfer Complexes of Hydrogen Chloride with Ammonia and Methylated Amines

Abstract

The response of proton vibrations of the complexes of hydrogen chloride with ammonia and methylated amines to electrostatic fields was investigated. Infrared spectroscopic measurements were conducted for the complexes isolated in the solid Ar matrix under the influence of strong external electric fields ($<1 \times 10^8$ V/m). The vibrational bands of the parallel/anti-parallel (“proton stretching”) and the perpendicular (“proton bending”) proton motions showed the exceptionally drastic field-driven changes. The Stark spectral changes were characteristic of each complex which represents a different degree of field-induced proton dislocation in the complexes. The spectroscopic observations were interpreted and discussed with the concept of protonic polarizability of the complexes in parallel/anti-parallel and perpendicular directions to the proton-transfer coordinate.

6.1. Introduction

Strongly hydrogen-bonded molecular complexes, typically composed of a strong Brønsted-Lowry acid and a strong base, have been a target of numerous studies to reveal the nature of hydrogen bond and proton transfer [1–18]. Pimentel and coworkers used the matrix isolation technique to pioneer the studies on the strongly hydrogen-bonded complexes, especially on the molecular complexes of hydrogen halides (HX) with base molecules (B). They grouped these complexes into three classes according to what they called “normalized proton affinity (PA) difference” Δ , defined as $[PA(B) - PA(X^-)]/[PA(B) + PA(X^-)]$ [1]. “Type I” complexes are those with largely negative Δ , in which the proton is much closer to the halide ion (X^-) than to the base molecule. When Δ increases above a certain value, proton is nearly equally shared by X^- and B, and they named this class of complexes as “completely shared” or “type II” hydrogen bond. “Type III” complexes have more positive Δ than “type II” and have an ion pair structure, in which proton transfer has occurred to have hydrogen bonding between X^- and BH^+ ions. Pimentel and coworkers also introduced a plot called “vibrational correlation diagram,” in which the frequency of proton vibration ($X \cdots H \cdots B$ asymmetric stretching) of the molecular complexes is correlated with the normalized proton affinity difference. They observed that the proton vibration frequency, originally the H–X stretching before complexation, significantly red-shifts with increasing Δ , reaches a minimum frequency point at “type II” region, and increases back to higher frequency as Δ increases from the turning point. Barnes and coworkers expanded the studies by investigating a large variety of molecular complexes isolated in various matrices [2–4]. They observed a similar correlation of proton vibration frequencies to the proton affinity difference, with an additional consideration on the effect of matrix.

A prototypical example of this system is the complexes of hydrogen chloride (HCl) with ammonia (NH₃) and methylated amines (methylamine; MeNH₂, dimethylamine; Me₂NH, trimethylamine; Me₃N) [5–10]. Ammonia and amines span a wide range of proton affinity through methylation, complexation of which with HCl forms a family of complexes including all three proton-transfer types. Figure 6-1 shows the vibrational correlation diagram of these complexes and HCl–H₂O. The proton frequency shown in the ordinate indicates the frequency of the Cl···H···N asymmetric stretching in general, which can be approximated to the H–Cl and N–H local stretching modes for “type I” and “type III” complexes, respectively. The H–Cl stretching retains its vibrational character when HCl is complexed with weak base molecules, forming “type I” complexes. It becomes, however, the Cl···H···N asymmetric stretching when proton is shared between Cl[−] and N (“type II”) and the N–H stretching of NH⁺ bond in “type III” complexes.

The matrix effect significantly alters the proton vibration frequency of the isolated complex compared to the gas-phase frequency [9, 10]. In the case of HCl–NH₃ 1:1 complex, the H–Cl stretching frequency differs significantly between gas-phase (~2200 cm^{−1}) and in the Ar matrix (1370 cm^{−1}) [4]. This contrasts with the similar frequency of uncomplexed HCl monomer in the Ar matrix (2871 cm^{−1}) to gas-phase frequency (2886 cm^{−1}) [19, 20]. The substantial difference in proton vibrational frequency between gas-phase and in matrix may be attributed to the large susceptibility of proton vibration to the internal electrostatic fields of the matrix as well as structural confinement effect of the matrix.

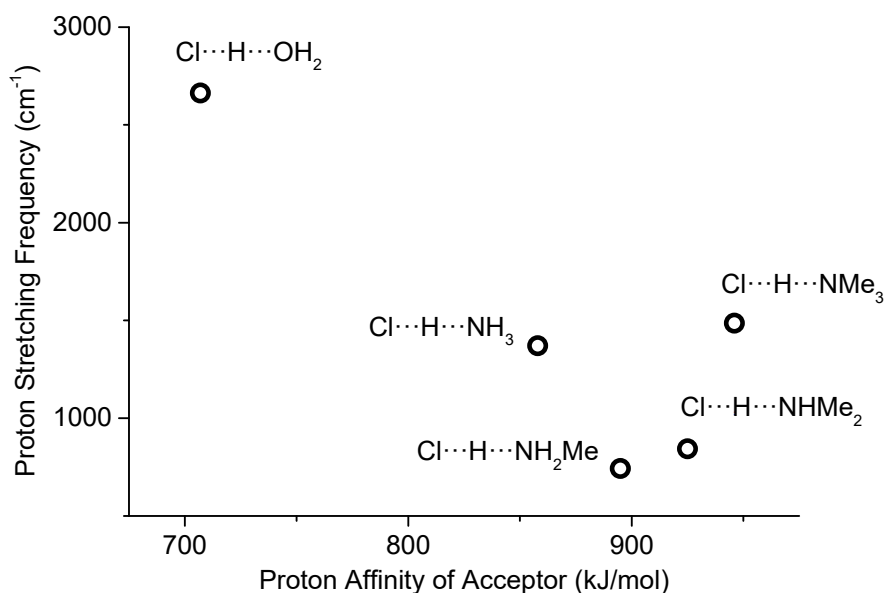


Figure 6-1. Vibrational correlation diagram of A···H···B complexes (A = Cl; B = H₂O, NH₃, MeNH₂, Me₂NH, Me₃N) isolated in the Ar matrix. The proton stretching frequency of each complex is plotted as a function of proton affinity of the acceptor (B).

Electrostatic fields are thought to be a critical factor on the process of proton transfer. In this work, the IR spectral changes of the matrix-isolated molecular complexes of HCl with NH₃ and methylated amines under the influence of strong experimental fields (<10⁸ V/m) were investigated. The external fields were systematically applied by using the ice film nanocapacitor method [21, 22]. Each proton-transfer complex showed a characteristic field-induced spectral change. The spectral changes were rationalized by the displacement of proton induced by electrostatic fields.

6.2. Experimental Details

The experiments were conducted in an ultrahigh vacuum (UHV) chamber, described in detail elsewhere [22, 23]. The molecular films were prepared on a Pt(111) substrate at about 10 K by sequential deposition of the corresponding gaseous species introduced into the UHV chamber through variable leak valves. Ar, NH₃, and HCl (Sigma-Aldrich, >99%) gases were used directly from commercially available gas cylinders. MeNH₂, Me₂NH, and Me₃N gases were prepared by thermal evaporation of corresponding molecules from MeNH₂ (Aldrich, 40 wt % in H₂O), Me₂NH (Aldrich, 40 wt % in H₂O), and Me₃N (Aldrich, 45 wt % in H₂O) aqueous solutions, respectively, utilizing the large vapor pressure of amines relative to that of water. All liquid materials used in the preparation of gaseous species, including D₂O (Aldrich, 99 atom % D), were purified by freeze–pump–thaw cycles. Tube dosers were used to guide gaseous HCl, NH₃, and amines close to the Pt(111) substrate. Other gases were back-filled.

The matrix-isolation of molecular complexes was achieved by co-adsorbing the corresponding molecules with excess amount of Ar gas. The sample had a stacked structure of an Ar film (288–960 ML thickness; ML = monolayer; 1 ML = 1.1×10^{15} molecules/cm²) containing molecular complexes of interest, which was sandwiched between two spacer layers (96–120 ML each) of pure Ar films. The Ar film was capped with an amorphous D₂O film (25 ML). The thickness of the complete sample was 290–710 nm.

Electrostatic fields were applied across the film by using the ice film nanocapacitor method, the detailed description of which can be found elsewhere [21].

The field strength was increased by the deposition of Cs⁺ ions on the capping ice film and decreased by spraying low energy (roughly 3 eV) electrons on the film [24, 25]. The strength of the applied field was estimated from the film voltage measured with a Kelvin probe. The macroscopic field strength (F_0), given in this paper, was obtained simply by dividing the film voltage with the thickness of the film. The actual field strength is expected to be $c_{\text{local}}F_0$, with the local field correction factor c_{local} roughly estimated to be in the range of 1–2 [22, 26].

Reflection–absorption infrared spectroscopic (RAIRS) measurements were conducted using a Fourier transform infrared spectrometer with a liquid nitrogen-cooled mercury–cadmium–telluride detector in the grazing angle reflection geometry (85°). An incident IR beam was p-polarized by a wire grid polarizer. The RAIR spectra were averaged 1024 times with 4 cm⁻¹ resolution. The sloped baselines of RAIR spectra, caused by the increasing negative reflectance–absorbance with increasing wavenumber [27, 28], were corrected for better visualization.

6.3. Results

In a simplified point of view, the proton in the Cl···H···NH_nMe_{3-n} (n=0–3) complexes has three degrees of motional freedom. One of them is the movement along the proton-transfer coordinate which results in the stretching vibration of proton. The proton vibrations that are essentially the proton motion parallel to the proton-transfer coordinate corresponds to the H–Cl stretching for “type I”, the Cl···H···N asymmetric stretching for “type II”, and the N–H stretching for “type III” complexes. In the rest of this article, we use a term “proton stretching” to indicate all these stretching vibrations. Other two degrees of freedom are perpendicular

motions with respect to the proton-transfer coordinate. The vibrations predominantly composed of proton motion perpendicular to the axis are termed “proton bending” in this work. For C_{3v} complexes, $\text{Cl}\cdots\text{H}\cdots\text{NH}_3$ and $\text{Cl}\cdots\text{H}\cdots\text{NMe}_3$, the perpendicular proton motions result in the doubly-degenerate $\text{Cl}\cdots\text{H}\cdots\text{N}$ bending vibrations.

The IR spectrum of each $\text{Cl}\cdots\text{H}\cdots\text{NH}_n\text{Me}_{3-n}$ ($n=0-3$) complex, in addition to vibrational bands of the $\text{NH}_n\text{Me}_{3-n}$ molecule, is expected to show an intense band originating from the proton stretching and bands from the proton bending, the field-induced spectral changes of which are the main focus of this research. In the case of $\text{Cl}\cdots\text{H}\cdots\text{NH}_3$ and $\text{Cl}\cdots\text{H}\cdots\text{NMe}_3$ complexes, the proton bending band were reported to be as intense as the proton stretching band [5, 6]. The low-frequency motions such as the intermolecular stretching (or $\text{Cl}\cdots\text{H}\cdots\text{N}$ symmetric stretching) and the libration of HCl or $\text{NH}_n\text{Me}_{3-n}$ molecules are also expected to be IR active, though those were not investigated in this work. The proton stretching and bending motions can vibrationally couple with the vibrations of the $\text{NH}_n\text{Me}_{3-n}$ molecule, which complicates the normal mode analysis of the complexes.

The proton stretching ($\text{H}-\text{Cl}$ stretching) vibration of $\text{HCl}-\text{NH}_3$ 1:1 complex isolated in the Ar matrix displays a broad band at 1370 cm^{-1} [5, 7]. The band is shaded gray in Figure 6-2. When external fields were applied, the band became split into two components, accompanied by the decrease of intensity (dotted difference spectrum in Figure 6-2). The band located at 1070 cm^{-1} corresponds to the umbrella vibration of NH_3 in $\text{HCl}-\text{NH}_3$ complex. The umbrella vibration of uncomplexed NH_3 monomer in the Ar matrix has 968 cm^{-1} frequency [29, 30]. It became Stark-broadened by the external field, with the magnitude of Stark sensitivity ($|\Delta\mu|$; $\Delta\mu = \Delta\tilde{\nu}/F_{\text{ext}}$; $\Delta\tilde{\nu}$ = frequency change; F_{ext} = external field strength) estimated to be around $16\text{ cm}^{-1}/(10^8\text{ V/m})$ (see Chapter 4), which is similar to that of the umbrella vibration of the matrix-isolated NH_3 monomer ($14\text{ cm}^{-1}/(10^8\text{ V/m})$) [29]. The band

at 1290 cm^{-1} was assigned, by Barnes et al., to the proton bending ($\text{Cl}\cdots\text{H}\cdots\text{N}$ bending) motion [5], while Andrews and coworkers reassigned it as the first overtone of H–Cl libration which locates at 734 cm^{-1} [7]. In both assignments, the band is correlated with predominantly the protonic motion where the proton is oscillating perpendicular to the main axis of the complex. The large field-induced spectral change of 1290 cm^{-1} band agrees with the assignment of the band to protonic motion. The bands in $1400\text{--}1470\text{ cm}^{-1}$ and $1080\text{--}1120\text{ cm}^{-1}$ were assigned to larger aggregates of HCl and NH_3 [5, 7].

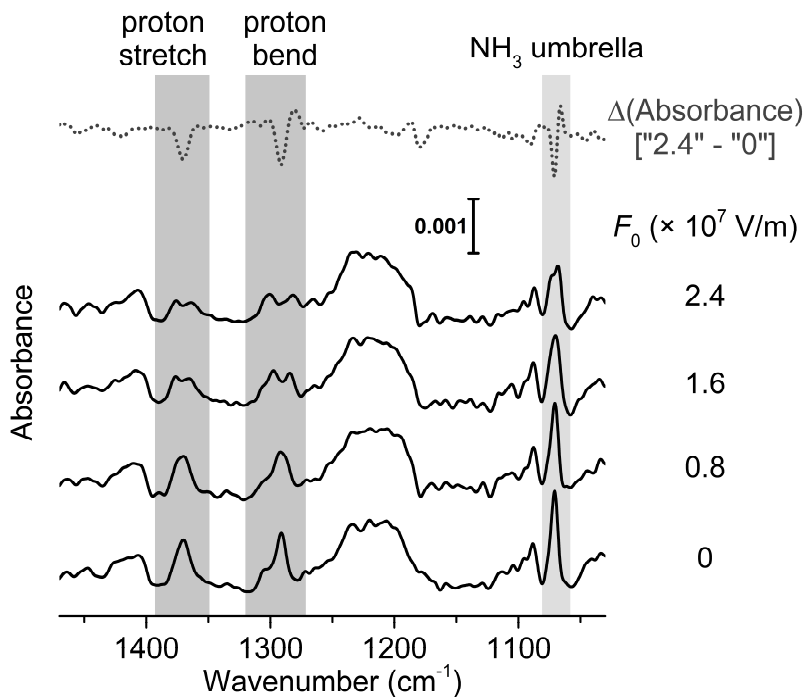


Figure 6-2. RAIR spectra of the Ar matrix containing HCl and NH_3 acquired as a function of field strength. The bands that correspond to HCl– NH_3 1:1 complex are highlighted with shades. Dotted line indicates the difference absorbance between the Stark spectrum at $2.4 \times 10^7\text{ V/m}$ and the zero-field spectrum. The broad band at 1220

cm^{-1} is of the bending vibration of D_2O layer capping the Ar matrix, used for the ice film nanocapacitor.

Ab initio calculations on the HCl-NH_3 complex expect the extraordinarily large IR intensity for proton stretching motion, but not for the perpendicular proton motions. The calculated IR intensity for perpendicular motions was about two orders of magnitude smaller than that for proton stretch. In experimental observations on the matrix-isolated HCl-NH_3 complex, however, the IR bands at 1290 cm^{-1} and 734 cm^{-1} , which were assigned to perpendicular proton motions, had comparable intensity with 1370 cm^{-1} band [5, 7]. The reason for this discrepancy between experiments and calculations is uncertain. It may originate from the poor estimation of quantum calculations on IR intensity and/or frequency of intermolecular vibrational motions.

Figure 6-3 shows the field-induced spectral changes of matrix-isolated HCl-MeNH_2 1:1 complex. The broad band at 743 cm^{-1} , gray-highlighted in Figure 6-3, corresponds to the proton stretching motion [6]. It has lower frequency than its correspondence of HCl-NH_3 complex. Upon the application of external fields, the position of the band became blue-shifted (743 cm^{-1} at zero-field $\rightarrow 750 \text{ cm}^{-1}$ at $3.5 \times 10^7 \text{ V/m}$) and the width of the band became larger (full width at half maximum 17 cm^{-1} at zero-field $\rightarrow 24 \text{ cm}^{-1}$ at $3.5 \times 10^7 \text{ V/m}$). The transition with small intensity at 915 cm^{-1} , shaded light gray in Figure 6-3, was assigned to the NH_2 wagging weakly mixed with proton motion [6]. The peak seemed to undergo field-induced broadening, though the small intensity restricts a clear observation. Note that the increase of frequency of NH_3 umbrella vibration (968 cm^{-1} for NH_3 monomer in Ar $\rightarrow 1070 \text{ cm}^{-1}$ for HCl-NH_3 in Ar) [29, 30] and NH_2 wagging (796 cm^{-1} for MeNH_2 monomer in Ar $\rightarrow 915 \text{ cm}^{-1}$ for HCl-MeNH_2 in Ar) [6] upon complexation of NH_3

and MeNH₂ with HCl, respectively, was both about 100 cm⁻¹. The slash pattern in Figure 6-3 around 800 cm⁻¹ indicates the spectral region where abnormally large instrumental errors in the equipment used in the present work forbade a proper analysis.

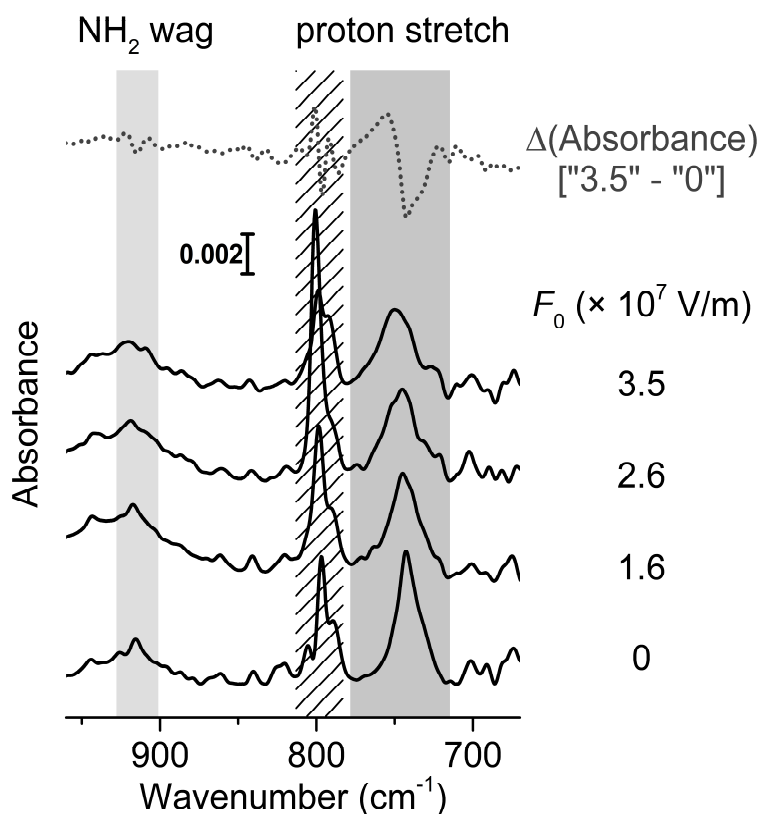


Figure 6-3. Stark spectra of HCl–MeNH₂ complex. The slash pattern around 800 cm⁻¹ shows the spectral region with large instrumental error.

The frequency of the proton stretching bounces back to higher frequency under additional methylation from HCl–MeNH₂. It appeared at 843 cm⁻¹ for HCl–Me₂NH complex isolated in the Ar matrix [6], as shown in Figure 6-4 with gray

shade. The external fields induced the band at 843 cm^{-1} to be split into two components and decreased the intensity of the band, similarly to 1370 cm^{-1} band of HCl-NH₃. Barnes et al. assigned the peak at 915 cm^{-1} to the NH in-plane bending of HCl-Me₂NH complex in Ar (note: the NH in-plane bending of Me₂NH monomer in Ar locates at 734 cm^{-1}) [6], an analogous motion to the NH₃ umbrella vibration in HCl-NH₃ and the NH₂ wagging in HCl-MeNH₂. Though too weak to be clearly identified, this peak at 915 cm^{-1} , shaded light gray in Figure 6-4, seemed to be broadened by external fields. Features at 850–900 cm^{-1} are thought to originate from aggregates of HCl and Me₂NH [6].

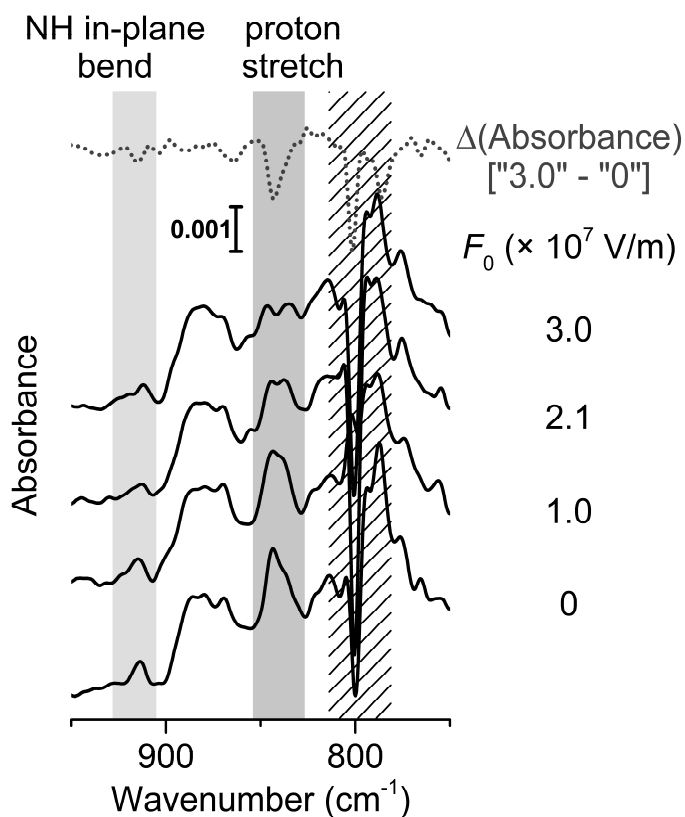


Figure 6-4. Stark spectra of HCl-Me₂NH complex.

In Figure 6-5, the IR spectrum of the Ar matrix containing Me₃N and HCl (black line, zero-field) was compared with that of Me₃N only (gray dashed line). 1472, 1455, 1439 cm⁻¹ transitions were assigned to the CH₃ deformation (*A*₁, *E*), 1271 cm⁻¹ to the CN stretch (*E*), 1185 cm⁻¹ to the CH₃ rock (*A*₁), and 1097, 1040 cm⁻¹ to the CH₃ rock (*E*) of Me₃N monomer isolated in solid Ar matrix [6, 31]. Three bands in HCl–Me₃N spectra were evidently distinguishable from Me₃N-only spectra: 1486, 1030, and 1019 cm⁻¹ transitions. Barnes et al. assigned 1486 cm⁻¹ band to the proton stretching of HCl–Me₃N complex and 1030 and 1019 cm⁻¹ bands to proton bending strongly coupled with the CH₃ rocking (*E*) mode [6].

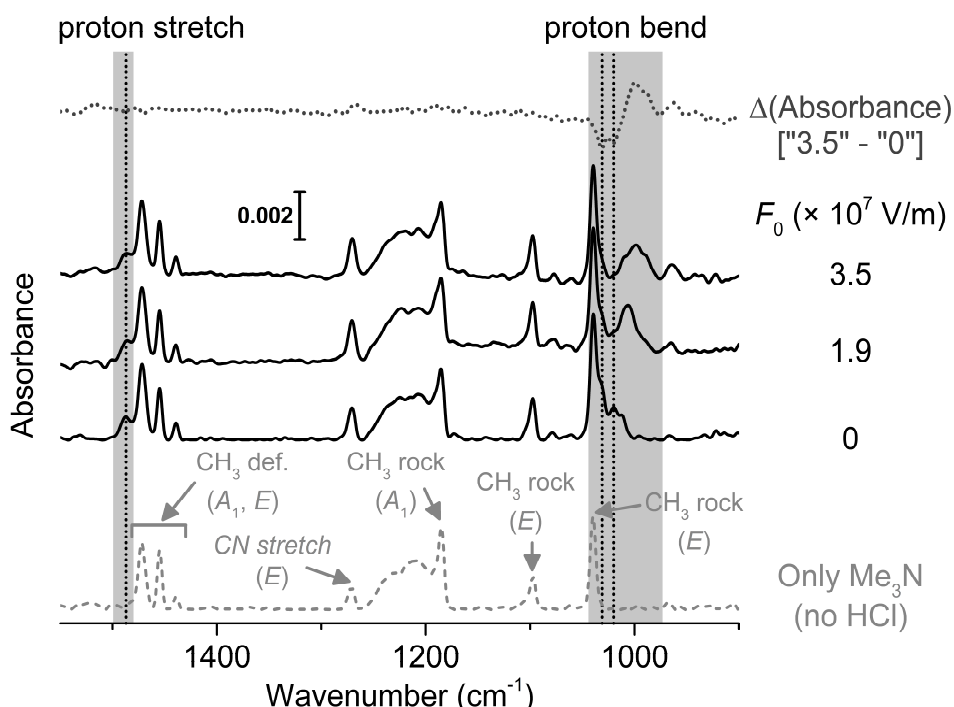


Figure 6-5. Stark spectra of HCl–Me₃N complex. The dashed gray spectrum was acquired from the Ar matrix containing only Me₃N, without HCl. The dotted vertical

lines indicate the peak positions of the matrix-isolated HCl–Me₃N 1:1 complex.

The external fields resulted little effect on 1486 cm⁻¹ peak, but significantly influenced 1030 and 1019 cm⁻¹ peaks. As inferred from the difference absorbance shown with dotted line in Figure 6-5, 1030 and 1019 cm⁻¹ transitions shifted toward lower frequency as external field became stronger. The transitions which correspond to Me₃N monomer were unchanged by external fields on the scale displayed in Figure 6-5.

6.4. Discussion

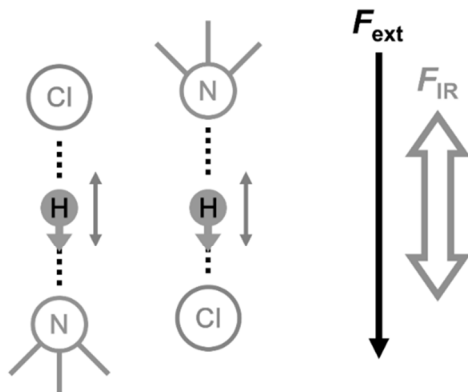
The HCl complexes with NH₃ and amines are a representative homologous series in that they share a common essential structure during proton transfer: for instance, when the equilibrium structure is calculated for HCl–NH₃ complex with a fixed H–Cl distance ($r(\text{H–Cl})$) which coincides with that of HCl–Me₃N, the resulting H–N distance ($r(\text{H–N})$) and N–Cl distance ($r(\text{N–Cl})$) would be almost identical for both complexes. This makes the family of the complexes serve as a prototypical system of proton-transfer complexes with HCl and N-base molecules.

In the rigid Ar matrix, the strongly hydrogen-bonded molecular complexes are expected to retain their initial isotropic distribution of orientation under the external fields of $<10^8$ V/m applied in this work. The field-driven splitting of the proton stretching band at 1370 cm⁻¹ of HCl–NH₃ complex results from the 10⁻¹ pm order displacement of proton along the proton-transfer axis induced by external fields ($<10^8$ V/m), as the previous work on HCl–H₂O complex under fields has demonstrated (see Chapter 5). The external fields parallel to the dipole would induce

the elongation of $r(\text{H}-\text{Cl})$, translocating proton closer to NH_3 by means of the dipole-field stabilization energy, resulting in the red-shift of the proton stretching. The anti-parallel fields affect in an opposite manner, blue-shifting the band.

The proton bending vibration of $\text{HCl}-\text{NH}_3$ complex has a transition dipole perpendicular to the proton-transfer coordinate (main axis of the complex). This implies that the complexes whose proton bending vibration contributes dominantly to the experimentally observed intensity have perpendicular orientation with respect to external electrostatic fields collinear with the IR radiative field. These complexes undergo little parallel or anti-parallel displacement of proton (see Figure 6-6). Instead, the proton may be displaced perpendicularly by the perpendicular external fields. The large intensity of the proton bending in the zero-field experimental spectra, comparable to that of the proton stretching, implies the significant perpendicular displacement of proton by radiative fields, which provides the feasibility of perpendicular proton dislocation by an external dc field. When the proton is perpendicularly displaced by a dc field, the proton bending vibration is expected to be manipulated in two manners: 1) the frequency would change unidirectionally (presumably to lower frequency due to the lowered force constant upon perpendicular proton displacement), since the complex has an approximately cylindrical symmetry (rigorously C_{3v}) and perpendicular fields are applied in radial direction, 2) the double-degeneracy (E symmetry in C_{3v}) would be broken.

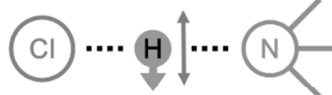
Parallel/Anti-Parallel Field



Intensity(proton stretch) $\gg 0$
Intensity(proton bend) ≈ 0

Parallel/anti-parallel proton displacement by external field

Perpendicular Field



Intensity(proton stretch) ≈ 0
Intensity(proton bend) $\gg 0$

Perpendicular proton displacement by external field

Figure 6-6. Schematic of proton displacement induced by parallel/anti-parallel and perpendicular external fields.

The ensemble of HCl-NH₃ complexes isolated in the Ar matrix has an isotropic distribution of orientation with respect to an external field. This means that the majority of IR intensities of the proton stretching and bending would experience the field neither parallel/anti-parallel nor perpendicular, which may result in the two-dimensional (parallel/anti-parallel + perpendicular) proton displacement. Therefore, in addition to the spectral changes of the proton stretching induced by parallel/anti-parallel fields and those of the proton bending by perpendicular fields discussed above, the cross terms, namely the response of the proton stretching vibration by perpendicular displacement and that of the proton bending by parallel/anti-parallel displacement, should be taken into consideration in order to account for the experimental Stark spectral changes. Quantum calculations on the complex will be

needed to elucidate these effects and ultimately to confidently interpret the observed Stark spectra. This approach may account for the intensity decrease of the proton stretching band (1370 cm^{-1}) under the influence of an external field as shown in Figure 6-2, the reason for which is unexplainable by the known vibrational Stark effect of a single oscillator with an isotropic orientation distribution [32, 33].

The unidirectional blue-shift of the proton stretching band (743 cm^{-1}) of HCl–MeNH₂ seems to originate from the field-induced parallel/anti-parallel displacement of proton in the complex. Since the HCl–MeNH₂ complex isolated in the Ar matrix, with the lowest proton stretching frequency among the family of molecular complexes of HCl with NH₃ and methylated amines, can be classified as a complex with “completely shared” or “type II” hydrogen bond, proton displacement in both parallel and anti-parallel directions would result in the increase of proton stretching frequency. In other words, the extremely broad minimum of the potential energy surface along the proton stretching coordinate becomes narrower by external fields regardless of their parallel/anti-parallel directions.

In the case of HCl–Me₂NH, the proton stretching band at 843 cm^{-1} showed a similar field-response with that of HCl–NH₃ complex. This implies that the behavior of proton in HCl–Me₂NH, which slightly deviates from “type II” to “type III” class, would be similar to that of HCl–NH₃, “type I” complex.

The 1486 cm^{-1} band of HCl–Me₃N, which was assigned to the proton stretching by Barnes and coworkers [6], changed little under the influence of external fields. This contrasts to the substantially large field-induced spectral change of proton stretching vibrations of other complexes. Two possibilities may account for the little field-driven spectral change of HCl–Me₃N: 1) the 1486 cm^{-1} band originates mostly from the CH₃ deformation (A_1), only weakly associated with the proton stretching, 2) The parallel/anti-parallel proton displacement is not significant in this

complex. The latter can be rationalized by the complex being an ion pair structure and the proton is bound to N as N–H⁺ bond. Spectral analysis based on quantum structure calculation will be needed to distinguish these possibilities.

The significantly field-modified 1030 and 1019 cm⁻¹ bands of HCl–Me₃N possibly correspond to the proton bending vibration coupled with the CH₃ rock (*E*) of Me₃N molecule, as suggested previously [6]. Those may alternatively correspond to the proton stretching coupled to the totally-symmetric (*A*₁) vibrations of Me₃N, but the nearest *A*₁ symmetry bands (CH₃ rock: 1185 cm⁻¹, CN stretch: 823 cm⁻¹) are not in enough vicinity from 1030, 1019 cm⁻¹ bands to be coupled. Besides, the experimentally observed unidirectional red-shift by external fields cannot be explained with frequency change of proton stretching vibration induced by parallel/anti-parallel proton displacement. We speculate that the Stark spectra revealed the frequency change of the proton bending vibration of HCl–Me₃N caused by substantial perpendicular displacement of proton in the complex. Again, the large intensity of the proton bending band implies that the proton is prone to be displaced perpendicularly by perpendicular fields. The frequency of the proton bending is expected to be red-shifted and the double-degeneracy would be destroyed upon the perpendicular proton displacement. In addition, as the frequency of proton bending evolves away from that of CH₃ rock (*E*) of Me₃N (~1040 cm⁻¹), the intermolecular coupling between those two motions would be weakened.

Figure 6-7 is a plot of peak frequency as a function of external field strength, compiled for the molecular complexes investigated in this work. From the linear frequency change, the magnitude of Stark sensitivity, $c_{\text{local}}|\Delta\mu|/c_{\text{dist}}$, can be estimated, where c_{local} (1–2) is the local field correction factor and c_{dist} (1.2–1.4) accounts for the isotropic angular distribution of dipoles with respect to the direction of external field. For the band split into two components by external fields, the average rate of

frequency shifts was used for the estimation. Since the spectral changes of the complexes do not have a definitive interpretation yet, we cannot guarantee that those values simply estimated from the linear frequency change would be physically meaningful. It can be argued, however, with certainty, that the proton-involved vibrations of HCl complexes with NH_3 and amines are extremely sensitive to external electrostatic fields, with Stark sensitivity values about an order of magnitude larger than that of uncomplexed HCl ($2.7 \text{ cm}^{-1}/(10^8 \text{ V/m})$) [20].

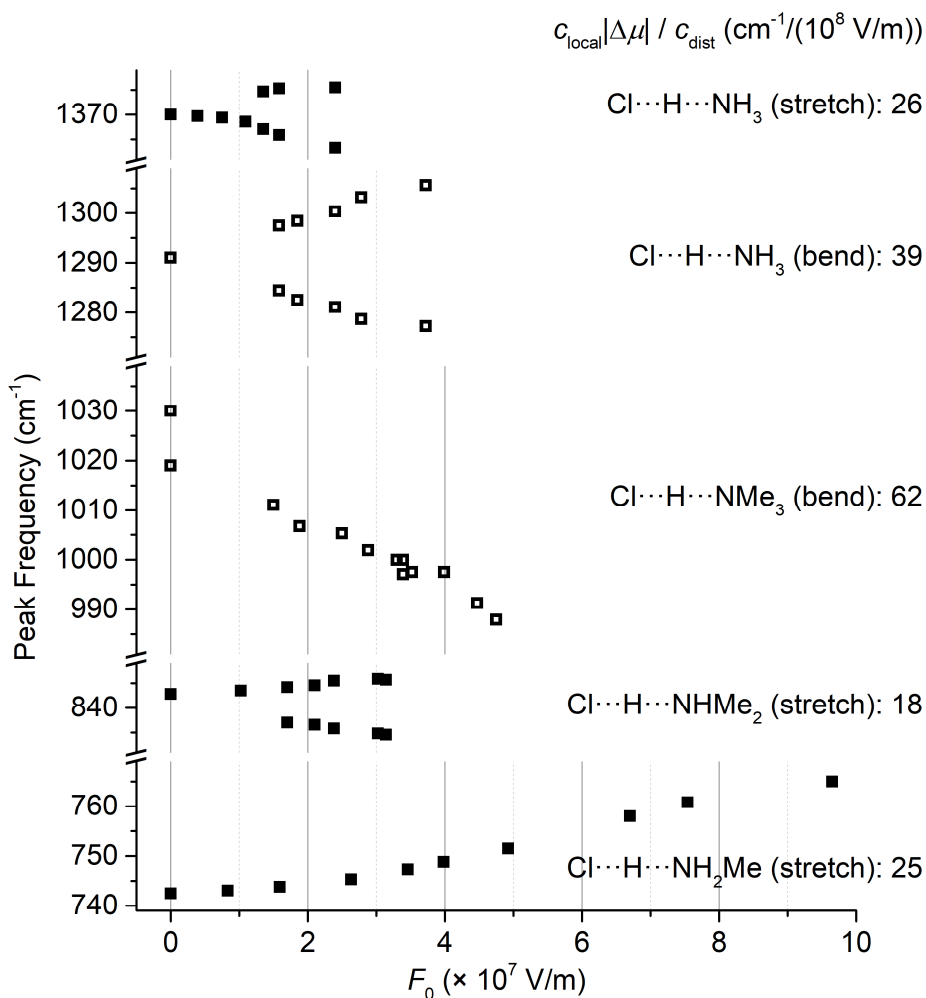


Figure 6-7. Peak frequency plot as a function of external field strength for different matrix-isolated complexes of HCl with NH₃, MeNH₂, Me₂NH, and Me₃N. The Stark sensitivity values, $c_{\text{local}}|\Delta\mu|/c_{\text{dist}}$, estimated from the frequency change under external fields, are shown in the right-side of the plot.

6.5. Conclusion

The IR spectra of the proton-transfer complexes of HCl with NH₃, MeNH₂, Me₂NH, and Me₃N were investigated under the influence of external electrostatic fields of $<1 \times 10^8$ V/m. The bands for the proton stretching and the proton bending showed drastic changes by fields. The spectral changes observed for different complexes were characteristic of different stages of proton transfer in acid–base complex. The large field-susceptibility of the proton stretching and the proton bending is proposed to originate from the protonic polarizability of complexes in parallel/anti-parallel and perpendicular directions, respectively. The parallel/anti-parallel polarization of proton by electrostatic fields implies the important role of electrostatics in various proton transfer processes including coupled electron and proton transfer reactions. As a novel concept which has hardly been proposed previously, the perpendicular proton polarization may open a new perspective on protonic behavior in molecular physics and chemistry. This study would provide an insight on the veiled electrostatic behavior of proton.

References

1. Ault, B. S.; Steinback, E.; Pimentel, G. C. Matrix Isolation Studies of Hydrogen Bonding. Vibrational Correlation Diagram. *J. Phys. Chem.* **1975**, *79*, 615–620.
2. Barnes, A. Molecular Complexes of the Hydrogen Halides Studied by Matrix Isolation Infrared Spectroscopy. *J. Mol. Struct.* **1983**, *100*, 259–280.
3. Barnes, A.; Legon, A. Proton Transfer in Amine-Hydrogen Halide Complexes: Comparison of Low Temperature Matrices with the Gas Phase. *J. Mol. Struct.* **1998**, *448*, 101–106.
4. Barnes, A. J.; Latajka, Z.; Biczysko, M. Proton Transfer in Strongly Hydrogen-Bonded Molecular Complexes: Matrix Effects. *J. Mol. Struct.* **2002**, *614*, 11–21.
5. Barnes, A. J.; Beech, T. R.; Mielke, Z. Strongly Hydrogen-Bonded Molecular Complexes Studied by Matrix-Isolation Vibrational Spectroscopy. Part 1.—The Ammonia–Hydrogen Chloride Complex. *J. Chem. Soc. Faraday Trans. 2* **1984**, *80*, 455–463.
6. Barnes, A. J.; Kuzniarski, J. N. S.; Mielke, Z. Strongly Hydrogen-Bonded Molecular Complexes Studied by Matrix-Isolation Vibrational Spectroscopy. Part 2.—Amine–Hydrogen Chloride Complexes. *J. Chem. Soc. Faraday Trans. 2* **1984**, *80*, 465–476.
7. Andrews, L.; Wang, X.; Mielke, Z. Infrared Spectrum of the H₃N–HCl Complex in Solid Ne, Ne/Ar, Ar, and Kr. Matrix Effects on a Strong Hydrogen-Bonded Complex. *J. Phys. Chem. A* **2001**, *105*, 6054–6064.
8. Andrews, L.; Wang, X.; Mielke, Z. Infrared Spectrum of the H₃N–HCl

- Complex in Solid Neon. *J. Am. Chem. Soc.* **2001**, *123*, 1499–1500.
9. Jordan, M. J.; Del Bene, J. E. Unraveling Environmental Effects on Hydrogen-Bonded Complexes: Matrix Effects on the Structures and Proton-Stretching Frequencies of Hydrogen– Halide Complexes with Ammonia and Trimethylamine. *J. Am. Chem. Soc.* **2000**, *122*, 2101–2115.
 10. Bevitt, J.; Chapman, K.; Crittenden, D.; Jordan, M. J.; Del Bene, J. E. An ab initio Study of Anharmonicity and Field Effects in Hydrogen-Bonded Complexes of the Deuterated Analogues of HCl and HBr with NH₃ and N(CH₃)₃. *J. Phys. Chem. A* **2001**, *105*, 3371–3378.
 11. Brciz, A.; Karpfen, A.; Lischka, H.; Schuster, P. A Candidate for an Ion Pair in the Vapor Phase: Proton Transfer in Complexes R₃N-HX. *Chem. Phys.* **1984**, *89*, 337–343.
 12. Legon, A. C. The Nature of Ammonium and Methylammonium Halides in the Vapour Phase: Hydrogen Bonding versus Proton Transfer. *Chem. Soc. Rev.* **1993**, *22*, 153–163.
 13. Snyder, J. A.; Cazar, R. A.; Jamka, A. J.; Tao, F.-M. Ab Initio Study of Gas-Phase Proton Transfer in Ammonia–Hydrogen Halides and the Influence of Water Molecules. *J. Phys. Chem. A* **1999**, *103*, 7719–7724.
 14. Alkorta, I.; Rozas, I.; Mó, O.; Yáñez, M.; Elguero, J. Hydrogen Bond vs Proton Transfer between Neutral Molecules in the Gas Phase. *J. Phys. Chem. A* **2001**, *105*, 7481–7485.
 15. Li, R.-J.; Li, Z.-R.; Wu, D.; Chen, W.; Li, Y.; Wang, B.-Q.; Sun, C.-C. Proton Transfer of NH₃–HCl Catalyzed by Only One Molecule. *J. Phys. Chem. A* **2005**, *109*, 629–634.
 16. Eustis, S. N.; Radisic, D.; Bowen, K. H.; Bachorz, R. A.; Haranczyk, M.; Schenter, G. K.; Gutowski, M. Electron-Driven Acid-Base Chemistry:

- Proton Transfer from Hydrogen Chloride to Ammonia. *Science* **2008**, *319*, 936–939.
17. Zhou, Z.-J.; Li, X.-P.; Liu, Z.-B.; Li, Z.-R.; Huang, X.-R.; Sun, C.-C. Electric Field-Driven Acid–Base Chemistry: Proton Transfer from Acid (HCl) to Base (NH₃/H₂O). *J. Phys. Chem. A* **2011**, *115*, 1418–1422.
 18. Weiss, N. M.; Waller, A. W.; Phillips, J. A. Infrared Spectrum of CH₃CN–HCl in Solid Neon, and Modeling Matrix Effects in CH₃CN–HCl and H₃N–HCl. *J. Mol. Struct.* **2016**, *1105*, 341–349.
 19. Hallam, H. E. *Vibrational Spectroscopy of Trapped Species*; Wiley: Hoboken, 1973, pp. 70–80.
 20. Kang, H.; Park, Y.; Kim, Z. H.; Kang, H. Electric Field Effect on Condensed-Phase Molecular Systems. VI. Field-Driven Orientation of Hydrogen Chloride in an Argon Matrix. *J. Phys. Chem. A* **2018**, *122*, 2871–2876.
 21. Shin, S.; Kim, Y.; Moon, E.-s.; Lee, D. H.; Kang, H.; Kang, H. Generation of Strong Electric Fields in an Ice Film Capacitor. *J. Chem. Phys.* **2013**, *139*, 074201.
 22. Park, Y.; Kang, H.; Kang, H. Brute Force Orientation of Matrix-Isolated Molecules: Reversible Reorientation of Formaldehyde in an Argon Matrix toward Perfect Alignment. *Angew. Chem. Int. Ed.* **2017**, *56*, 1046–1049.
 23. Kang, H.; Shin, S.; Park, Y.; Kang, H. Electric Field Effect on Condensed-Phase Molecular Systems. III. The Origin of the Field-Induced Change in the Vibrational Frequency of Adsorbed CO on Pt (111). *J. Phys. Chem. C* **2016**, *120*, 17579–17587.
 24. Horowitz, Y.; Asscher, M. Low Energy Charged Particles Interacting with Amorphous Solid Water Layers. *J. Chem. Phys.* **2012**, *136*, 134701.

25. Shin, S.; Kim, Y.; Kang, H.; Kang, H. Effect of Electric Field on Condensed-Phase Molecular Systems. I. Dipolar Polarization of Amorphous Solid Acetone. *J. Phys. Chem. C* **2015**, *119*, 15588–15595.
26. Fried, S. D.; Boxer, S. G. Measuring Electric Fields and Noncovalent Interactions Using the Vibrational Stark Effect. *Acc. Chem. Res.* **2015**, *48*, 998–1006.
27. Ayotte, P.; Plessis, S.; Marchand, P. Trapping Proton Transfer Intermediates in the Disordered Hydrogen-Bonded Network of Cryogenic Hydrofluoric Acid Solutions. *Phys. Chem. Chem. Phys.* **2008**, *10*, 4785–4792.
28. Cholette, F.; Zubkov, T.; Smith, R. S.; Dohnalek, Z.; Kay, B. D.; Ayotte, P. Infrared Spectroscopy and Optical Constants of Porous Amorphous Solid Water. *J. Phys. Chem. B* **2009**, *113*, 4131–4140.
29. Park, Y.; Kang, H.; Field, R. W.; Kang, H. The Frequency-Domain IR Spectrum of Ammonia Encodes Changes in Molecular Dynamics Caused by a DC Electric Field. *Proc. Natl. Acad. Sci. U.S.A.* **2019**, *116*, 23444–23447.
30. Abouaf-Marguin, L.; Jacox, M. E.; Milligan, D. E. The Rotation and Inversion of Normal and Deuterated Ammonia in Inert Matrices. *J. Mol. Spectrosc.* **1977**, *67*, 34–61.
31. Goldfarb, T. D.; Khare, B. N. Infrared Spectra of Solid and Matrix-Isolated $(\text{CH}_3)_3\text{N}$, $(\text{CD}_3)_3\text{N}$, and $(\text{SiH}_3)_3\text{N}$. *J. Chem. Phys.* **1967**, *46*, 3379–3384.
32. Bublitz, G. U.; Boxer, S. G. Stark Spectroscopy: Applications in Chemistry, Biology, and Materials Science. *Annu. Rev. Phys. Chem.* **1997**, *48*, 213–242.
33. Andrews, S. S.; Boxer, S. G. Vibrational Stark Effects of Nitriles I. Methods and Experimental Results. *J. Phys. Chem. A* **2000**, *104*, 11853–11863.

Chapter 7

Summary

This dissertation explores the experimental manipulation of molecules and molecular clusters with external electrostatic fields. The molecules and molecular clusters of interest have been isolated in the inert Ar matrices. Strong external electrostatic fields ($<2 \times 10^8$ V/m) have been applied across the matrices containing the target molecules and clusters by using the ice film nanocapacitor method. It has been shown in **Chapter 3** that electrostatic fields can manipulate the inversion dynamics of ammonia molecule. The field-induced frequency shifts have been investigated for small hydrogen-bonded clusters of water and ammonia, and the clustering effect on Stark response has been discussed in **Chapter 4**. It is demonstrated that electric fields on 10^8 V/m scale enable the dislocation of proton in the hydrated acid clusters and proton-transfer complexes in **Chapter 5** and **Chapter 6**, respectively.

As mentioned in **Chapter 1**, the manipulation of molecules, and therefore their dynamics and reactivity, with controllable external forces is a dream of chemists. Nature utilizes the electrostatics in an extremely sophisticated way to control dynamics and reactions in chemical and biological systems. Nature knows in what strength and in which direction electric fields are generated by charges, and how they affect the molecular properties in the complicated systems. Chemists try to mimic what nature does. Organic chemists change the solvent and therefore local electric field to control reactions. Biochemists design artificial protein structures to

manipulate the reactivity at enzymatic site. Electrochemists apply a bias voltage to induce reactions within the electric double layer. Inherent in all these methods can be regarded as fundamental electrostatics: control of electric fields in the solvent environment, inside the protein structure, and at the electrode/liquid interface. Yet, we are far from complete understanding of the molecular electrostatics in the real system.

Presented in this dissertation partly illustrate how the electric fields interact with molecules and molecular clusters and how the fields can be utilized for manipulating molecular structures and reactions. Eventually, this type of studies is expected to shed light on the detailed mechanism of intermolecular interactions and chemical processes. Besides, the well-understood and perfect control of molecules with external fields will potentially lead us to realize our imagination in nano- and quantum technologies. Of course, there are still numbers of questions to be answered on the way to these goals. How would strong external forces influence the motional (rotational, vibrational, translational) behaviors of molecules and intra-/inter-molecular chemical properties in the complicated molecular systems? How can we push the boundary beyond the current limitation on the applicable strength of controlled external forces to molecular systems?

In brief, the studies carried out in this dissertation show that the vibrational spectroscopy with the aid of unprecedentedly strong dc electric field can provide rich information on the electrostatic behaviors of molecules and molecular clusters, which underlie the understanding of intermolecular processes and molecular manipulation.

List of Publications

1. Hani Kang, Sunghwan Shin, Youngwook Park, and Heon Kang, Electric Field Effect on Condensed-Phase Molecular Systems. III. The Origin of the Field-Induced Change in the Vibrational Frequency of Adsorbed CO on Pt(111). *J. Phys. Chem. C* **2016**, *120*, 17579–17587.
2. Youngwook Park, Hani Kang, and Heon Kang, Brute Force Orientation of Matrix-Isolated Molecules: Reversible Reorientation of Formaldehyde in an Argon Matrix toward Perfect Alignment. *Angew. Chem. Int. Ed.* **2017**, *56*, 1046–1049.
3. Sunghwan Shin, Youngwook Park, Youngsoon Kim, and Heon Kang, Dissociation of Trifluoroacetic Acid in Amorphous Solid Water: Charge-Delocalized Hydroniums and Zundel Continuum Absorption. *J. Phys. Chem. C* **2017**, *121*, 12842–12848.
4. Sunghwan Shin, Youngwook Park, Hani Kang, and Heon Kang, Electric Field Effect on Condensed-Phase Molecular Systems. IV. Conformational Change of 1,2-Dichloroethane in a Frozen Molecular Solid. *J. Phys. Chem. C* **2017**, *121*, 25342–25346.
5. Sunghwan Shin, Youngwook Park, Hani Kang, and Heon Kang, Electric Field Effect on Condensed-Phase Molecular Systems. V. Acid–Base Proton Transfer at the Interface of Molecular Films. *J. Phys. Chem. C* **2018**, *122*, 4901–4907.
6. Hani Kang, Youngwook Park, Zee Hwan Kim, and Heon Kang, Electric Field Effect on Condensed-Phase Molecular Systems. VI. Field-Driven

- Orientation of Hydrogen Chloride in an Argon Matrix. *J. Phys. Chem. A* **2018**, *122*, 2871–2876.
7. Youngwook Park,[†] Sunghwan Shin,[†] and Heon Kang, Entropy-Driven Spontaneous Reaction in Cryogenic Ice: Dissociation of Fluoroacetic Acids. *J. Phys. Chem. Lett.* **2018**, *9*, 4282–4286. ([†]equal contribution)
 8. Youngwook Park, Jong Hyeon Lim, Jin Yong Lee, and Heon Kang, Electric Field Effect on Condensed-Phase Molecular Systems. VII. Vibrational Stark Sensitivity of Spatially Oriented Water Molecules in an Argon Matrix. *J. Phys. Chem. C* **2019**, *123*, 9868–9874.
 9. Youngwook Park, Hani Kang, Robert W. Field, and Heon Kang, The Frequency-Domain IR Spectrum of Ammonia Encodes Changes in Molecular Dynamics Caused by a DC Electric Field. *Proc. Natl. Acad. Sci. U.S.A.* **2019**, *116*, 23444–23447.
 10. Hani Kang, Josée Maurais, Youngwook Park, Patrick Ayotte, and Heon Kang, Electric Field Effect on Condensed-Phase Molecular Systems. VIII. Vibrational Stark Effect and Dipolar Inversion in a Carbon Monoxide Crystal. *J. Phys. Chem. C* **2019**, *123*, 31262–31271.
 11. Youngwook Park, Hani Kang, and Heon Kang, Electric Field Effect on Condensed-Phase Molecular Systems. IX. Control of Proton Displacement in Matrix-Isolated Hydrogen Chloride–Water Complexes. *accepted (J. Phys. Chem. C)*.
 12. Youngwook Park, Jong Hyeon Lim, Jin Yong Lee, and Heon Kang, Vibrational Stark Effect on Matrix-Isolated Formaldehyde: the Matrix Effect. *manuscript in preparation*.
 13. Youngwook Park, Hani Kang, and Heon Kang, Experimental Measurement of Vibrational Stark Sensitivity of Small Molecular Clusters: Clustering

Effect on Stark Response of Vibrations. *manuscript in preparation.*

14. Youngwook Park, Jong Hyeon Lim, Jin Yong Lee, and Heon Kang, Vibrational Stark Spectroscopy on Proton Vibrations in Proton-Transfer Complexes of Hydrogen Chloride with Ammonia and Methylated Amines. *manuscript in preparation.*

Abstract in Korean (국문 초록)

전기장을 이용한 분자 및 분자 클러스터 조작에 관한 연구

서울대학교 대학원

화학부 물리화학전공

박 영 욱

본 학위 논문은 10^8 V/m 수준의 강한 외부 정전기장이 저온의 비활성 매트릭스 내에 고립된 분자 및 분자 클러스터의 방향, 구조, 동력학 등의 성질을 어떻게 조작하는지에 대해 다룬다. ‘얼음 박막 축전법’과 ‘매트릭스 고립법’을 동시에 이용하여 이전 연구에서는 가할 수 없었던 강한 외부 직류 전기장을 고립된 분자와 분자 클러스터에 가할 수 있었다. 외부 전기장에 의한 분자 특성의 변화는 진동 분광학을 이용해 관측하였다.

1장에서는 외부 힘을 통해 분자를 조작하는 기존 연구들을 소개한다. 정전기장, 자기장, 광학 전기장 등의 외부 힘을 이용한 분자 조작에 관한 간단한 역사를 소개하고, 그 후에는 정전기장을 이용한 연구들에 대해 보다 자세히 다룬다. 본 학위 논문 연구에서 이용된 방법론에 대해서도 간단히 소개한다.

2장에서는 연구에 사용된 실험 방법을 설명한다. 강한 외부

전기장을 걸어주기 위해 ‘얼음 박막 축전법’을 사용하였고, 고립된 분자 및 분자 클러스터를 만들기 위해서는 ‘매트릭스 고립법’을 사용하였다. 전기장에 의한 분자 및 분자 클러스터의 변화는 ‘반사-흡수 적외선 분광법’이 사용되었다. 이 방법들에 대한 원리적, 실용적 측면들을 요약한다. 실험에 사용된 장치에 대해서도 묘사한다.

3장은 암모니아 분자의 반전 터널링 동력학의 전기장에 의한 변화에 대한 분광학적 연구이다. 아르곤 매트릭스 내의 암모니아 분자는 외부 방해가 없을 때 대칭적인 이중-최소점 퍼텐셜 에너지 표면 내에서 매우 빠른 우산-반전 터널링을 일으키는 것으로 알려져 있다. 강한 외부 전기장이 가해지면 반전 상태들의 Stark 섞임이 일어나고, 그로 인해 분자가 전기장 방향으로 정렬하게 된다. 정렬된 암모니아 분자는 비대칭적인 이중-최소점 퍼텐셜 에너지 표면을 가지게 되고, 따라서 반전 터널링이 일어나지 않게 된다. 외부 전기장에 의한 이러한 변화들은 전기장 세기를 변화시켜가며 얻은 적외선 스펙트럼에 암호화되어 있으며, 본 연구에서는 퍼텐셜 에너지 표면, 파동함수의 편재화, 전이 선택 규칙 등을 이용하여 이를 해석하였다.

4장에서는 물과 암모니아 분자를 포함하는 수소 결합 클러스터의 진동 Stark 민감도의 실험적 측정에 관해 다룬다. 외부 전기장은 분자 진동의 퍼텐셜 에너지 표면을 조작하여 진동수 이동을 일으키는데, 이를 진동 Stark 효과라고 한다. 분자 클러스터의 진동 Stark 민감도는 클러스터를 이루지 않은 단독 분자의 민감도와 크게 다른 것으로 관찰되었다. 이러한 클러스터 효과를 진동의 비조화성, 구조적 효과, 분자간 진동 짝지움 등의 측면에서 논의한다. 수소 결합을

통한 클러스터링의 극단적 예시로 결정형 얼음의 진동 스펙트럼이 전기장에 의해 어떻게 변하는지를 조사하였으며, 이를 단독 물분자와 비교하였다.

5장과 6장은 강한 외부 전기장이 산성 양성자를 이동시킬 수 있다는 것을 실험적으로 보여주었다. **5장**은 염화수소-물(H_2O , D_2O) 클러스터에 대한 진동 Stark 분광학적 연구이다. 이 클러스터의 양성자 신축 진동수가 외부 전기장에 의해 매우 크게 변화한 것을 관찰하였다. 염화수소- D_2O 클러스터의 경우에는 양성자 신축 진동과 D_2O 의 대칭 신축 진동의 짝지음이 외부 전기장에 의해 변하는 것을 관찰하였다. 양자 계산을 이용해 스펙트럼을 해석한 결과, 외부 전기장이 염화수소-물 클러스터의 양성자 전달 좌표 상에서 양성자가 가역적, 비대칭적으로 이동하도록 유도한다는 사실을 알 수 있었다. **6장**은 염화수소와 암모니아, 메틸화된 아민 분자의 클러스터에 대한 연구이다. 이 클러스터들은 양성자 전달 시스템의 대표적인 예이다. 평행한 방향의 양성자 신축 진동 뿐만 아니라 수직 방향의 양성자 굽힘 진동 역시 외부 전기장에 의해 큰 진동수 변화를 나타냈다. 각 양성자 전달 분자 클러스터는 전기장에 의해 고유한 스펙트럼 변화를 보였다. 수화된 산성 분자와 양성자 전달계에 대한 이러한 연구는 양성자의 거동에 있어서 핵심적인 개념인 큰 양성자 편극도에 대한 실험적 증거를 제공한다.

7장은 본 학위 논문의 요약이다. 본 연구의 중요성과 전망을 분자간 화학적 과정과 양자 기술에서의 분자 조작의 측면에서 서술한다.

주요어: 분자 조작, 전기장, 터널링 동역학, 분자 클러스터, 수화된 산성
분자, 양성자 전달계, 진동 분광학

학 번: 2014-21234

Acknowledgement (감사의 글)

이 학위논문은 저의 이름으로 나가지만, 박사학위 과정 동안 많은 분들의 지도와 도움이 없었다면 불가능했을 일입니다. 가장 먼저, 부족한 저에게 연구를 할 수 있는 기회를 주시고 학위 과정 동안 양질의 지도와 따뜻한 격려를 아끼지 않으시며 연구자/학자의 자세를 몸소 가르쳐주신 저의 지도교수님 강 현 교수님께 깊은 감사를 드립니다.

바쁘신 와중에도 저의 학위논문 심사를 기꺼이 맡아 주시고 논문에 대한 귀한 조언을 주신 심사위원장 이성훈 교수님을 비롯하여 심사위원 김지환 교수님, 이정호 교수님, 성균관대 이진용 교수님께 큰 감사를 드립니다. 특히 이진용 교수님과 그 연구실의 임종현 학생께서는 저의 학위 과정 동안 여러 연구를 공동으로 진행하며 제가 수행하기 힘든 이론적 접근을 가능하게 해주셨습니다. 감사드립니다. I would like to express my sincere gratitude to Prof. Robert Field at MIT for his invaluable advice and collaboration on molecular spectroscopic theory, and Prof. Patrick Ayotte at Université de Sherbrooke as well for all the instructive and precious discussions that we shared over a long period of time. 수료 심사 때 심사위원을 맡아 주시고, 박사과정 장학금 지원에 큰 도움을 주신 석차옥 교수님께도 감사드립니다. 호기심 가득한 과학자의 표본으로 저에게 늘 건강한 자극을 주시는 이동환 교수님께도 감사의 인사를 전하고 싶습니다.

저의 학위 과정은 약 6년 정도였습니다. 짧다면 짧고 길다면 긴 시간 동안 연구실에서 함께 연구하며 학문적으로, 그리고 연구 외적으로

많은 것들을 배울 수 있게 해주신 저희 연구실 선배님들 및 동료들, 영순, 성환, 두형, 재혁, 한이에게 진심 어린 감사를 전합니다. 연구에 필요한 분자 합성에 도움을 주었고, 500동에서 함께 지내며 많은 시간을 공유한 화학부 동료 현창에게도 감사를 포함합니다. 같은 분야에서 공부하며 기쁨과 고충을 나누었던 다른 연구실의 대학원생 동료들에게도 감사합니다. 2015년부터 5년 동안 연구에 집중할 수 있도록 장학금을 지원해준 한국연구재단의 글로벌박사펠로우십에 감사드립니다.

연구 외적으로 저의 일상을 지탱하는데 도움을 주신 분들이 있습니다. 아침마다 생각없이 테니스를 함께 쳤던 ATE 멤버들 (은혜, 남우, 호운, 한검, 인성, 중기, 은아, 민석), 생각없이 만나서 아무 얘기 안하고 함께 있기에 참 좋은 고등학교 친구들 (승원, 선일, 신명, 용우, 섭), 생각없이 이 산 저 산 함께 오르던 등산 멤버들 (성환, 선미, 재연, 석희) 에게 감사를 전합니다. 이 사람들과 함께하며 머릿속을 비우지 않았다면, 부족한 점이 참 많은 저로서는 아마 지난 6년 간 오롯이 연구에 집중하지 못했을 것입니다.

마지막으로 저의 가장 가까운 사람들에게 감사를 표하며 끝맺겠습니다. 특유의 사랑스러움과 귀여움으로 제 곁을 지켜준 매력적인 코를 가진 지원에게 마음 속 깊은 고마움을 전합니다. 한창 경제활동 할 나이에 자기 공부한다고 용돈 한 번 제대로 못 드린 못난 아들을 멀찍이서 지켜봐 주신 가족에게도 감사합니다.